
Interaction of intense laser pulses with overdense plasmas.

Theoretical and numerical study.

Sergey Rykovanov



München 2009

Interaction of intense laser pulses with overdense plasmas.

Theoretical and numerical study.

Sergey Rykovanov

Dissertation
an der Fakultät für Physik
der Ludwig-Maximilians-Universität
München
vorgelegt von
Sergey Rykovanov
aus Snezhinsk

München, den 14 August 2009

Erstgutachter: Prof. Dr. Hartmut Ruhl

Zweitgutachter: Prof. Dr. Dietrich Habs

Tag der mündlichen Prüfung: 2 November 2009

Contents

Abstract	ix
Zusammenfassung	xi
1 Introduction and motivation	1
1.1 Intense laser-matter interactions	1
1.2 High order harmonics generation and attosecond physics	2
1.2.1 Overview	2
1.2.2 Attosecond physics	4
1.3 Generation of mono-energetic ion beams	6
1.4 Structure of the thesis	7
2 Main equations and methods of numerical simulations	9
2.1 Main equations	9
2.1.1 Relativistic Unit System	12
2.2 Basics of the particle-in-cell method	12
2.2.1 Numerical scheme for Maxwell equations	13
2.2.2 Stability and numerical dispersion	15
2.2.3 Numerical scheme for equations of motion.	17
2.2.4 Current deposition.	20
2.2.5 Test case	24
2.3 Summary of the chapter	25

3 Generation of high-order harmonics on the plasma-vacuum boundary.	27
3.1 Oscillating Mirror (OM) harmonics	27
3.1.1 One-particle mirror model	27
3.1.2 Emission of harmonic spectrum.	35
3.2 Summary of the chapter.	38
4 Controlling the temporal structure of harmonic beam.	41
4.1 Intensity gating	42
4.2 Polarization gating	43
4.2.1 Dynamics of the reflecting surface	43
4.2.2 Dependance of harmonics generation efficiency on ellipticity	46
4.2.3 Results of the simulations of the polarization gating	50
4.2.4 Oblique incidence	50
4.3 Summary of the chapter.	54
5 Controlling the spatial structure of harmonic beam.	55
5.1 Surface denting	56
5.2 Focusing of harmonics	60
5.3 Controlling the divergence of the harmonic beam by shaped targets.	62
5.4 Influence of surface roughness on the divergence of harmonic beam.	63
5.5 Summary of the chapter.	66
6 Generation of monoenergetic ion beams from thin foils.	71
6.1 Ion acceleration in the radiation pressure regime	71
6.2 Model equations	74
6.3 Simulations	77
6.3.1 Optimal conditions for ion acceleration	77
6.3.2 Ellipticity effects	78
6.4 Summary of the chapter.	80

Inhaltsverzeichnis	vii
<hr/>	
7 Conclusions	83
7.1 Controlling the generation of attosecond pulses.	83
7.1.1 Controlling the temporal structure of attosecond pulses.	83
7.1.2 Controlling the spatial structure of attosecond pulses.	84
7.2 Controlling the generation of ion beams	85
Publications	103
Acknowledgements	107
Curriculum Vitae	111

Abstract

This thesis is devoted to theoretical studies of the interaction of intense laser pulses with solid-state targets. This area of laser physics is very active and fast growing as it might possess a number of useful applications in material science, physics, biology and medicine.

The main part of the thesis is devoted to the generation of high-order harmonics on the vacuum-plasma interface due to the longitudinal oscillatory motion of the reflecting surface. This has a prospect of generation of trains or even single attosecond pulses that have much more intensity than those generated in atomic media.

Before making this source an instrument for studying electron dynamics in condensed matter or for laser-vacuum interactions, one has to know how to control the important properties of the harmonic beam, namely its temporal and spatial structure. To pursue the answering of the question of control, analytical and numerical studies were performed. Most of the ideas are based on the shaping of the laser pulse (both in temporal and spatial domains) and of the target.

The second part of the thesis is devoted to the studies of the generation of energetic ion beams. These beams can be used, for example, in cancer therapy, plasma radiography and isotope production. The studies of the influence of laser pulse ellipticity and target thickness on ion beam monoenergetic features and energy allows one to use the results presented in this thesis for optimization of future experiments.

x

Zusammenfassung

Zusammenfassung

Diese Arbeit befasst sich mit theoretischen Untersuchungen der Wechselwirkung intensiver Laserpulse mit Festkörperoberflächen. Dieses Feld der Laserphysik ist momentan sehr aktuell und entwickelt sich schnell, da es eine Vielzahl von potentiellen Anwendungen auch jenseits der Physik in Materialwissenschaften, der Biologie und der Medizin verspricht.

Der Hauptteil dieser Arbeit befasst sich mit der Erzeugung von hohen Harmonischen der fundamentalen Laserfrequenz an der Grenzfläche zwischen Target und Vakuum als Folge der Oszillation der reflektierenden Grenzfläche im Feld des treibenden Lasers. Dieser Prozess verspricht die Erzeugung von Attosekunden-Pulszügen oder sogar einzelnen Attosekundenpulsen die wesentlich intensiver sind als entsprechende in Gastargets erzeugte Pulse. Bevor eine solche Quelle allerdings für zeitaufgelöste Untersuchungen der Elektronendynamik in Festkörpern oder Plasmen angewendet werden kann, ist es notwendig, die zeitlichen und räumlichen Eigenschaften der Pulse genau kontrollieren zu können. Zu diesem Zwecke wurden in dieser Arbeit detaillierte numerische und analytische Untersuchungen der Harmonischenerzeugung durchgeführt. Insbesondere wurde dabei untersucht, welchen Einfluss die räumlichen und zeitlichen Eigenschaften des Treiberlasers auf die erzeugten Harmonischen haben.

Der zweite Teil der Arbeit befasst sich mit der Erzeugung energetischer Ionenstrahlen. Solche Strahlen haben eine Vielzahl von potentiellen Anwendungen zum Beispiel in der Strahlentherapie, der Untersuchung von dichten Plasmen und der Erzeugung radioaktiver Isotope. In dieser Arbeit wird demonstriert, wie sich die Elliptizität des Laserpulses und die Targetdicke auf die Spektren und die Energie der erzeugten monoenergetischen Ionen

auswirkt. Mit Hilfe dieser Ergebnisse wird es in Zukunft möglich sein, Experimente zur Erzeugung von Ionenstrahlen wesentlich zu optimieren.

Chapter 1

Introduction and motivation

1.1 Intense laser-matter interactions

State-of-the-art laser systems are capable of generating electromagnetic pulses with unprecedented energy compression leading to intensities several orders of magnitude above the *relativistic* threshold ($I_{rel} \cdot \lambda_L^2 \geq 1.37 \cdot 10^{18} \text{W/cm}^2 \cdot \mu\text{m}^2$) [1, 2], i.e. the intensity of the wave in which oscillatory energy of a test electron $W_{osc} = eA_L/m_e c^2$ becomes more than its rest energy $m_e c^2$. Here λ_L is the laser wavelength, e, m_e are the electron charge and mass respectively, A_L is the wave vector potential and c is the speed of light in vacuum. The generation of relativistically strong laser pulses with duration less than 100 fs ($1 \text{ fs} = 10^{-15} \text{ s}$) became possible with the invention of the chirped-pulse-amplification (CPA) technique [3]. In this technique the broadband seed pulse is first stretched in time in order to avoid the material breakdown and nonlinear distortions of the pulse during amplification by strongly reducing its peak intensity. After the amplification the pulse is compressed in time back to the duration supported by its amplified bandwidth.

Relativistic intensities are much higher than intensities needed for target ionization. Thus it can be assumed that light interacts with a fully-ionized plasma at these intensities. The main feature of relativistic laser-plasma interactions is the character of the electron motion. Exposed to electromagnetic waves with such intensities the electron not only

wiggles transversely in electric field but also significantly drifts longitudinally due to the magnetic component of the Lorentz force [4, 5]. This behavior is the main reason for many interesting phenomena.

Relativistic laser-plasma studies are a fast growing and fascinating area of physics [6, 7, 8, 9] with a number of experimental breakthroughs. For example, during the interaction of laser radiation with under-dense plasma the longitudinal wakefields are formed that can trap the electrons and accelerate them up to GeV energy level in monochromatic fashion [10, 11, 12, 13, 14, 15]. This already found the application in generation of incoherent hard-x-ray betatron radiation [16] and VUV undulator radiation [17].

This thesis is devoted to the interaction of intense laser pulses with solid-state targets, namely to two interesting phenomena - transformation of initially narrow spectrum of the laser pulse into a broad harmonic spectrum and transformation of the energy of the laser pulse into the energy of the plasma ions. Both phenomena attract a lot of attention for a number of envisioned applications in physics, biology, medicine and materials science.

1.2 High order harmonics generation and attosecond physics

1.2.1 Overview

Historically, high-order harmonics from solid-state targets were probably first observed in 1977 by Burnett *et al* [18] who showed harmonics of CO_2 laser light with numbers extending up to 11-th. In 1981 Carman *et al* [19] observed up to 46 harmonics of the CO_2 laser light while using quite long pulses (1-2 ns, $\lambda_L = 10.6 \mu m$, $I = 10^{16} W/cm^2$) for which the hydrodynamical plasma expansion is not negligible and must be taken into account. An immediate proposal followed envisaging the application of harmonic emission as a measuring tool for plasma profile steepening [20]. First experimental studies of harmonic generation with short (100 fs to 2 ps) intense (up to $10^{17} W/cm^2$) solid-state lasers with $\lambda_L = 1 \mu m$ were conducted by Kohlweyer *et al* [21] and almost simultaneously by D. von der Linde

et al [22]. In these works with quite moderate intensities harmonics up to 15th were observed. Using pulses with intensity up to 10^{19} W/cm² and 2 ps duration P. Norreys *et al* [23] were able to generate up to 68 harmonics of the fundamental laser frequency. This was the first demonstration of harmonic generation with relativistic intensities later followed by a number of works [24, 25, 26, 27]. Due to the number of applications of the beams of harmonics, whose wavelength can reach nanometer range, the interest in this topic is constantly growing. It is important to highlight two papers demonstrating spatial [28] and temporal [29] coherence of such beams and opening the possibility to the creation of the *table-top* attosecond (1 as = 10^{-18} s) UV and X-ray sources.

From the theoretical side the process of high-order harmonics generation in over-dense plasmas was started to be investigated soon after the works of Carman *et al* [19]. Bezzerides *et al.* [30] applied hydrodynamic approach and showed that the presence of the plasma gradient for moderate intensities (i.e. when one can omit the relativistic corrections) leads to harmonic emission with well defined cut-off frequency corresponding to the plasma frequency $\omega_{co} = \omega_p$. This was however inconsistent with results of the studies based on PIC-simulations [31, 32] and experiments [23], which demonstrated the harmonics well beyond the plasma frequency of the target. In their work, Lichters and Meyer-ter-Vehn [33] distinguished two mechanisms - one responsible for the cut-off at ω_p and one exhibiting no plasma-frequency dependent cut-off. The first one is the mechanism of Bezzerides *et al.* [30] that is due to the inverse resonance absorption [34] of the wakefields created by the Brunel electron bunches [35] traveling through the plasma gradient. Experimental papers by Teubner *et al* [36], Tarasevitch *et al* [37] and Quere *et al* [38] studied this process (which can happen on both sides of the target) in more detail and demonstrated the plasma frequency dependent cut-off. Moreover, they showed the intensity dependent transition to the second (with no cut-off at ω_p) harmonic generation mechanism with the help of PIC simulations. This second mechanism is due to the forced longitudinal oscillation of the whole plasma surface leading to a Doppler shift of the incoming laser light. It is now generally accepted to call the first mechanism *Coherent Wake Emission* [38] and the second one *Oscillating Mirror* model [31]. The latter is the primary subject of this thesis.

1.2.2 Attosecond physics

Following from the Fourier Theorem, the generation of the broad spectrum is a prerequisite for generating ultra-short pulses. From it it follows that the width of the spectrum Ω and the width of the time structure τ (the duration) are connected via the expression $\Omega\tau = 2\pi$ if the phase is constant over the spectrum. For example if a filter is applied taking only harmonics with numbers from 10 to 20 of the laser with wavelength $\lambda_L = 1 \mu m$, then the width of this range is $\Omega = 2 \cdot 10^{16} 1/s$ and the Fourier-limited pulse duration is equal to $\tau = 314 \text{ as}$. This simple estimate shows that with moderate harmonic orders generated from infrared laser light it is possible to enter the attosecond domain. Please note that for the generation of attosecond pulses two conditions must be fulfilled. Firstly, the spectrum should be broad enough and secondly, the harmonics must be phase synchronized. As will be shown later, that the high-order harmonics from overdense plasmas fulfill these requirements.

It is important to stress that attosecond physics is already an active field in experimental physics with many high-profile applications (see [39] and references therein). Its main aim is to study the processes in atoms, molecules and condensed matter with sub-femtosecond time resolution. For example, it takes only 150 as for an electron to make one round-trip on the first Bohr orbit in the hydrogen atom. Historically, attosecond pulses were first generated in the experiments with gas jets where the incoming light was transformed into a broad spectrum with odd harmonics. The generation of gas harmonics can be understood in terms of the three-step-model proposed by Corkum [40]. Here an atom is first ionized and releases one electron, which is accelerated in the electromagnetic wave. During the next half period of the light field, the electron returns and recollides with the ionized atom, releasing a single broadband X-ray pulse. The periodic nature of this process subsequently leads to a spectral modulation, forming a harmonic comb in the spectral domain. Soon after this proposal, the conjecture of Farkas and Tóth [41] and of Harris *et al* [42] was experimentally confirmed. It states that if these monochromatic light waves of equally spaced frequencies are in phase, the interplay between constructive

and destructive interference in their superposition would give rise to temporal beating and therefore to generation of a train of attosecond pulses. Further innovations in short pulse laser technology gave rise to the generation of even single attosecond XUV bursts [43, 44, 45], which was promptly followed by an upsurge of extraordinary applications [46, 47, 48]. Unfortunately, the number of photons per unit time obtained by the atomic medium up-converter is low with the consequence of severely limiting the scope of applications of this attosecond pulse generation technique. This pertains in particular to the envisaged pump-probe measurements [49]: the attosecond pulse is split into two, the first one triggering the system into motion or starting a reaction, and the second one probing it after a controlled delay. But this approach is not feasible with attosecond pulses from atomic harmonics because they are too weak. Apparently, it needs another nonlinear medium operating at higher laser intensities and exhibiting higher efficiency. The relativistic interaction of an intense laser pulse with overdense plasma constitutes a very promising approach towards this objective. The main advantage over the process of harmonics generation in rarefied gases is that the plasma medium does not exhibit an inherent limit on the highest laser intensity that can be used. The projected specifications of the laser system envisioned for the near future allow for focused intensities of $10^{21} \text{ W/cm}^{-2}$ or even higher at a few hundred hertz repetition rates. The plasma medium can exploit these relativistic intensities and thus provide a novel source of intense attosecond pulses that will open the road to investigations with unparalleled temporal resolution for a host of new phenomena.

A very far-reaching application of attosecond pulses is the hope to experimentally approach the so called Schwinger limit (10^{29} W/cm^2), when quantum electrodynamics effects such as, for example, vacuum polarization become important [50]. Reaching this threshold intensity with optical radiation is beyond the limits of even the most ambitious laser projects such as ELI [51] or HIPER [52]. Focusing attosecond x-ray pulses that have a central wavelength of λ_{atto} to a minimal spot area $S_{atto} \approx \lambda_{atto}^2$ theoretically allows to concentrate the harmonics energy in a small enough volume to reach the intensities close to the Schwinger limit as discussed in [53, 54].

After all these considerations it becomes clear what problems experimentalist have to

overcome in order to generate trains or single intense attosecond pulses. It is important to obtain a coherent harmonic beam with a phase-synchronized broad spectrum. Before conducting an experiment it is also important to know how different parameters of target or laser will affect the production and quality of the beam. In other words, before advancing from an interesting topic of basic plasma physics to an everyday experimental tool it is important to know how to control the process. This is the main goal of this thesis - to study the effects of different parameters on harmonics generation and the ways of controlling their spatial and temporal structure.

1.3 Generation of mono-energetic ion beams

Another interesting phenomena occurring when a relativistically strong laser pulse impinges a solid-state target is the generation of energetic ions. The intensity of the plane wave in which the ion becomes relativistic is equal to $I_{ion}\lambda_L^2 = 1.37 \cdot 10^{18} \cdot M_i^2 \text{ W/cm}^2 \mu\text{m}^2$, where M_i - is the mass of the ion in the units of electron mass m_e . This means that for laser intensities less than 10^{24} W/cm^2 for $\lambda_L = 1\mu\text{m}$ one can assume that the light interacts with the electrons and not with the ions. However, if this interaction with electrons separates them from the ions, the created space charge fields can also affect the latter. There are several ways for the electrons to extract the energy from light in a collisionless plasma. If the plasma-vacuum interface is steep, then the electrons can absorb energy in the process of vacuum-heating [35] or the $\mathbf{j} \times \mathbf{B}$ heating [55]. In both cases it is important that the electron excursions are larger than the skin-depth, thus plasma electron can *lose the connection* and gain the energy from electromagnetic wave unlike the free electron.

If the plasma gradient is long, the resonance absorption becomes dominant [34]. In this case obliquely incident p-polarized laser pulse gets transformed into a longitudinal plasma wave near the resonance point where $n = n_{cr}$.

One of the ion acceleration mechanisms is based on the free plasma expansion into vacuum and was studied, for example, by Gurevich *et al* [56]. In the case of the thin foil this leads to thermal ion spectrum on both sides of the target. The second mechanism

usually referred to as target-normal-sheath-acceleration (TNSA, [57]) and is due to electron bunches created on the front surface of the target [58] that travel through the target, escape on the rear side and build the longitudinal field there. This mechanism normally also leads to the thermal spectrum, however, in some special cases [59] the mono-energetic ion beams can be generated. Third mechanism is the front side or shock acceleration of the ions [60]. Electrons being pushed inside by the laser pressure build the charge-separation fields and drag the ions. In this case the ions travel through the target and escape from the rear side possessing the thermal spectrum.

The acceleration of ions with ultra-high intensity laser pulses has attracted broad interest over the last decade [61, 62, 63, 64, 65, 66, 67, 68]. The high quality of the produced multi-MeV ion bunches in terms of very small values for the transversal and longitudinal emittances has stimulated discussions about a number of applications, such as cancer therapy [69, 70, 71, 72], isotope production [73, 74], plasma radiography [75], inertial confinement fusion (ICF) [76, 77] etc. However, only within the last years it became possible to produce mono-energetic ion beams directly from the irradiated targets [78, 79, 80] which is essential for some of the aforementioned applications. Since the mono-energetic ion beams are still generated via target normal sheath acceleration (TNSA, [57]), they suffer from a low laser-ion energy conversion efficiency of usually less than a few percent. Just recently, a new technique for a very efficient generation of quasi-mono-energetic ion beams was proposed by several authors [81, 82, 83, 84] and also studied experimentally [85]. The key-point is the use of ultra-thin foils and high-contrast, circularly polarized laser pulses. In this thesis the effect of the target thickness and laser ellipticity on the parameters of the generated ion beams is studied.

1.4 Structure of the thesis

The thesis is structured in the following way.

- Chapter 1 is the general introduction. The motivation for the studies is justified here.

- Chapter 2 describes the theoretical methods and methods of numerical simulations used in the thesis, describes and justifies the most important assumptions and shows the connection between Vlasov equation and particle-in-cell (PIC) method.
- Chapter 3 is devoted to the studies of the general dynamics of the reflecting surface during the interaction with a strong laser pulse. A simple one-dimensional one-particle model is described that allows to understand the main features of the surface motion. The emission of the harmonics is discussed based on both macro- and microscopic point of view.
- Chapter 4 discusses methods for controlling the temporal structure of the harmonics. A way of controlling the temporal structure is introduced based on the dynamically changing polarization inside the laser pulse - the polarization gating technique.
- In Chapter 5 the spatial coherence of the harmonic beam is discussed. The ways of controlling the divergence of the beam are presented based on target and laser shaping. It is demonstrated that the surface roughness under appropriate conditions can disappear and does not affect the coherence of the harmonics.
- Chapter 6 is devoted to the ion acceleration from thin foils using elliptically polarized laser pulses. The effect of the target thickness as well as laser ellipticity is discussed.

Chapter 2

Main equations and methods of numerical simulations

2.1 Main equations

Before writing down the main equations one should introduce the main assumptions that are almost always used in describing the interaction of intense laser pulses with matter.

First of all, relativistic intensities are several orders of magnitude higher than those needed for ionization of matter. For example, for the barrier suppression ionization (BSI) of the hydrogen atom an intensity of 10^{16} W/cm² is needed [86, 87, 88]. Relativistically intense laser pulse ionizes the matter already with its foot and the main part of it interacts with a fully ionized plasma.

Second, the electron-ion collision frequency is negligibly small for relativistic intensities and short pulses. One can estimate the ratio between mean free time between collisions τ_e [89] and the interaction time $\tau_{int} \approx 100$ fs:

$$\frac{\tau_e}{\tau_{int}} = \frac{T_e^{3/2} m^{1/2}}{4\pi e^4 n_e \ln \Lambda \cdot \tau_{int}}, \quad (2.1)$$

where T_e is the temperature of the electron component, which in the relativistic case can be estimated as the electron rest energy $T_e = 0.511$ MeV, m, e - are the electron mass

and charge respectively, $n_e \approx 4 \cdot 10^{23} \text{ 1/cm}^3$ is the solid state plasma density, $\ln \Lambda$ - is the so-called Coulomb logarithm [89] which is on the order of 20 for these intensities and plasma densities. Putting all the numbers together one gets

$$\frac{\tau_e}{\tau_{int}} \approx \frac{4 \cdot 10^{-12}}{100 \cdot 10^{-15}} \approx 40, \quad (2.2)$$

which means that the mean time between collisions is much larger than the interaction time. This fact allows one to neglect the collisions while describing the laser-plasma interactions.

For treating the laser-plasma interaction self-consistently one can write down Vlasov equation [90] for the distribution function $f(t, \mathbf{r}, \mathbf{p})$

$$\frac{\partial f}{\partial t} + \frac{\mathbf{p}}{m\gamma} \cdot \frac{\partial f}{\partial \mathbf{r}} + \mathbf{F} \frac{\partial f}{\partial \mathbf{p}} = 0 \quad (2.3)$$

and Maxwell equations [91] for the evolution of the electromagnetic fields

$$\frac{\partial \mathbf{E}}{\partial t} = c \cdot \text{rot} \mathbf{B} - 4\pi \mathbf{j} \quad (2.4)$$

$$\frac{\partial \mathbf{B}}{\partial t} = -c \cdot \text{rot} \mathbf{E}. \quad (2.5)$$

In this equations $\gamma = \sqrt{1 + (\mathbf{p}/mc)^2}$, the force \mathbf{F} equals to $\mathbf{F} = q\mathbf{E} + \frac{q}{c}\mathbf{v} \times \mathbf{B}$, and the current density \mathbf{j} can be found using the distribution function $\mathbf{j} = q \int \mathbf{v}(\mathbf{p}) f(t, \mathbf{r}, \mathbf{p}) d\mathbf{p}$, where $\mathbf{v}(\mathbf{p}) = \frac{\mathbf{p}}{m\gamma}$.

In the relativistic laser-plasma interactions there are almost no problems that allow exact analytical treatment due to the nonlinear gamma-factor and most of the time the numerical simulations are required. Seemingly the easiest and straightforward way would be to write the numerical scheme for eq. 2.3. However, even one-dimensional problems require at least a three-dimensional numerical grid for one coordinate and two momenta components. More than that, in many problems during the simulation time the distribution function is very compact in the momenta space. This leads to the non-effective calculation as the computer code has to simulate also the empty spaces - see for example

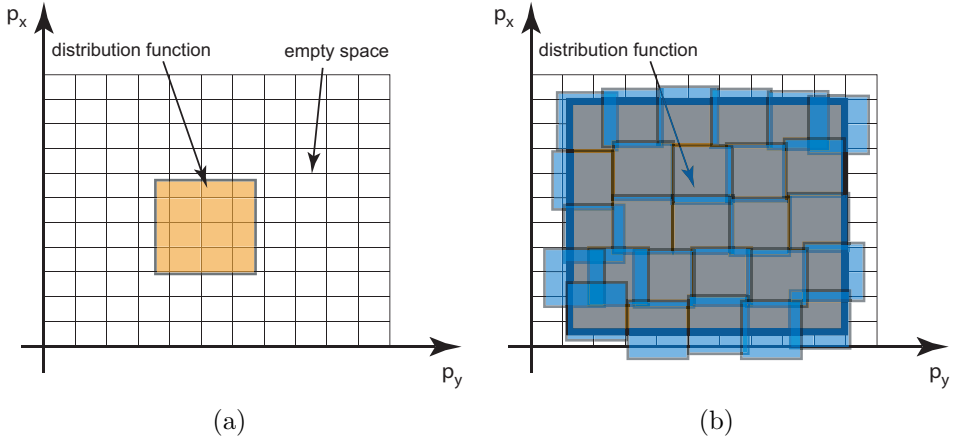


Figure 2.1: (a) Schematic drawing of the distribution function on the numerical grid. Empty areas lead to unefficient computation. (b) Sampling of the distribution function with the finite elements.

the schematic drawing on fig. 2.1a, where the projection of the distribution function in the one-dimensional case $f(t, x, p_x, p_y)$ on the p_x, p_y axes is shown (see also [6]).

There is another way of numerically solving eq. 2.3 - sampling the distribution function $f(t, \mathbf{r}, \mathbf{p})$ with the finite elements

$$f(t, \mathbf{r}, \mathbf{p}) = \sum_i S_i(\mathbf{r} - \mathbf{r}_i(t), \mathbf{p} - \mathbf{p}_i(t)), \quad (2.6)$$

where S_i is the shape-function of the particle, and $\mathbf{r}_i(t)$ and $\mathbf{p}_i(t)$ are its coordinates and momenta respectively (see illustration on fig. 2.1b). By doing that we put the time dependance of the distribution function in the time-dependent coordinates and momenta of the finite element, which will be called a quasi-particle or a macro-particle later. As the sampled function 2.6 satisfies eq. 2.3, the quasi-particles move along the characteristics of the Vlasov equation, thus their coordinates and momenta can be found from equations

$$\begin{aligned} \frac{d\mathbf{r}_i(t)}{dt} &= \frac{\mathbf{p}_i(t)}{m\gamma_i(t)} \\ \frac{d\mathbf{p}_i(t)}{dt} &= q\mathbf{E}(t, \mathbf{r}_i) + q\mathbf{v}_i(t) \times \mathbf{B}(t, \mathbf{r}_i). \end{aligned} \quad (2.7)$$

Note that the quasi-particles move in the same way as the specie (electrons or ions)

they represent. By initially sampling the distribution function with quasi-particles we get rid of the numerical grid in momenta space, that makes the PIC code more time efficient compared to the direct numerical solution of eq. 2.3. The main disadvantage of the PIC method is the fact that the sampling of the distribution function produces numerical fluctuations, which must be taken into account during the simulations by choosing the appropriate number of quasi-particles.

2.1.1 Relativistic Unit System

In equations 2.4, 2.5, 2.7 it is convenient to use the *relativistic unit system*, in which the normalized quantities for electric or magnetic field a , time t , length l , momentum p , and density n are obtained from their counterparts in CGS-units E , t' , l' , p' , and n' via

$$a = \frac{eE}{m_e c \omega_L}, \quad t = \omega_L t', \quad l = \frac{\omega_L}{c} l', \quad p = \frac{p'}{m_e c}, \quad n = \frac{n'}{n_{cr}}. \quad (2.8)$$

Here ω_L is the laser angular frequency, and $n_{cr} = m\omega_L^2/(4\pi e^2)$ - is the critical plasma density. The energy in this units is measured in units of the electron rest energy, the dimensionless field amplitude $a = 1$ denotes the transition to the relativistic regime when the oscillatory energy of the electron in the electromagnetic wave $W_{osc} = eE'/m_e c^2$ becomes equal to its rest energy. The corresponding intensity is called the *relativistic intensity* and is equal to $I_{rel} \lambda_L^2 = 1.37 \cdot 10^{18} \text{W/cm}^2 \cdot \mu\text{m}^2$. The laser wavelength used in this thesis is always set to $\lambda_L = 1\mu\text{m}$ if not noted otherwise. The target for this wavelength is always overdense, for example the glass target plasma has a density of about $n = 400$ (in critical densities n_{cr}).

2.2 Basics of the particle-in-cell method

To briefly summarize the previous section, in the PIC method the distribution function is approximated by a number of quasi-particles, whose evolution is described by the equations of motion for the relativistic particle (eq. 2.7). The evolution of the electromagnetic fields is

governed by Maxwell equations (eq. 2.4, 2.5). The connection between the quasi-particles and the fields is done via the current density \mathbf{j} . It is important to notice that the fields are determined on the Eulerian grid, whereas the particles move on the Lagrangian grid so that their coordinates and momenta are continuous. Therefore, every time step one needs to accommodate the particles on the Eulerian grid for finding the new field values and vice versa, distribute the fields to the particles to move them. Particle-in-cell method is good documented - for example in books [92, 93, 94] and papers [95, 96, 97, 98, 99].

2.2.1 Numerical scheme for Maxwell equations

Let us consider a two-dimensional problem, where every quantity depends on the laser propagation coordinate x and the transverse coordinate y . In the relativistic units the Maxwell equations read

$$\left\{ \begin{array}{l} \frac{\partial E_x}{\partial t} = \frac{\partial B_z}{\partial y} - j_x \\ \frac{\partial E_y}{\partial t} = -\frac{\partial B_z}{\partial x} - j_y \end{array} \right. \quad (2.9)$$

$$\left\{ \begin{array}{l} \frac{\partial E_z}{\partial t} = \left(\frac{\partial B_y}{\partial x} - \frac{\partial B_x}{\partial y} \right) - j_z \end{array} \right. \quad (2.11)$$

$$\left\{ \begin{array}{l} \frac{\partial B_x}{\partial t} = -\frac{\partial E_z}{\partial y} \end{array} \right. \quad (2.12)$$

$$\left\{ \begin{array}{l} \frac{\partial B_y}{\partial t} = \frac{\partial E_z}{\partial x} \end{array} \right. \quad (2.13)$$

$$\left\{ \begin{array}{l} \frac{\partial B_z}{\partial t} = -\left(\frac{\partial E_y}{\partial x} - \frac{\partial E_x}{\partial y} \right) \end{array} \right. \quad (2.14)$$

Without losing generality we can consider only the P-polarization (E_y, B_z, E_x mode). Following the one-dimensional scheme of Lichters [100] we introduce new functions $F^+ = E_y + B_z$ and $F^- = E_y - B_z$ and rewrite Maxwell equation in the following form

$$\left\{ \begin{array}{l} \frac{\partial E_x}{\partial t} = \frac{\partial(F^+ - F^-)}{2\partial y} - j_x \\ \left(\frac{\partial}{\partial t} + \frac{\partial}{\partial x} \right) F^+ = -j_y - \frac{\partial E_x}{\partial y} \\ \left(\frac{\partial}{\partial t} - \frac{\partial}{\partial x} \right) F^- = -j_y + \frac{\partial E_x}{\partial y} \end{array} \right. \quad (2.15)$$

$$\left\{ \begin{array}{l} \frac{\partial}{\partial t} + \frac{\partial}{\partial x} \end{array} \right) F^+ = -j_y - \frac{\partial E_x}{\partial y} \quad (2.16)$$

$$\left\{ \begin{array}{l} \frac{\partial}{\partial t} - \frac{\partial}{\partial x} \end{array} \right) F^- = -j_y + \frac{\partial E_x}{\partial y} \quad (2.17)$$

The numerical scheme for solving these equations was proposed by Y. Sentoku [101] and reads

$$\begin{aligned} E_x^{[n+1,i,j]} &= E_x^{[n,i,j]} + \\ &+ \frac{\Delta t}{2\Delta y} (B_z^{[n+1/2,i-1/2,j+1/2]} - B_z^{[n+1/2,i-1/2,j-1/2]} + B_z^{[n+1/2,i+1/2,j+1/2]} - B_z^{[n+1/2,i+1/2,j-1/2]}) - \\ &- \Delta t \cdot \frac{j_x^{[n+1/2,i-1/2,j]} + j_x^{[n+1/2,i+1/2,j]}}{2} \end{aligned} \quad (2.18)$$

$$\begin{aligned} F^{\pm[n+1/2,i\pm1/2,j+1/2]} &= F^{\pm[n-1/2,i\mp1/2,j+1/2]} \pm \frac{\Delta t}{\Delta y} (E_x^{[n,i,j+1]} - E_x^{[n,i,j]}) - \\ &- \Delta t \cdot \frac{j_y^{[n-1/2,i,j+1/2]} + j_y^{[n+1/2,i,j+1/2]}}{2} \end{aligned} \quad (2.19)$$

$$\begin{aligned} E_x^{[n+1/2,i,j]} &= E_x^{[n-1/2,i,j]} + \\ &+ \frac{\Delta t}{2\Delta y} (B_z^{[n,i-1/2,j+1/2]} - B_z^{[n,i-1/2,j-1/2]} + B_z^{[n,i+1/2,j+1/2]} - B_z^{[n,i+1/2,j-1/2]}) - \\ &- \Delta t \cdot \frac{j_x^{[n+1/2,i-1/2,j]} + j_x^{[n+1/2,i+1/2,j]} + j_x^{[n-1/2,i-1/2,j]} + j_x^{[n-1/2,i+1/2,j]}}{4} \end{aligned} \quad (2.20)$$

$$\begin{aligned} F^{\pm[n+1,i\pm1/2,j+1/2]} &= F^{\pm[n,i\mp1/2,j+1/2]} \pm \frac{\Delta t}{\Delta y} (E_x^{[n+1/2,i,j+1]} - E_x^{[n+1/2,i,j]}) - \\ &- \Delta t \cdot j_y^{[n+1/2,i,j+1/2]} \end{aligned} \quad (2.21)$$

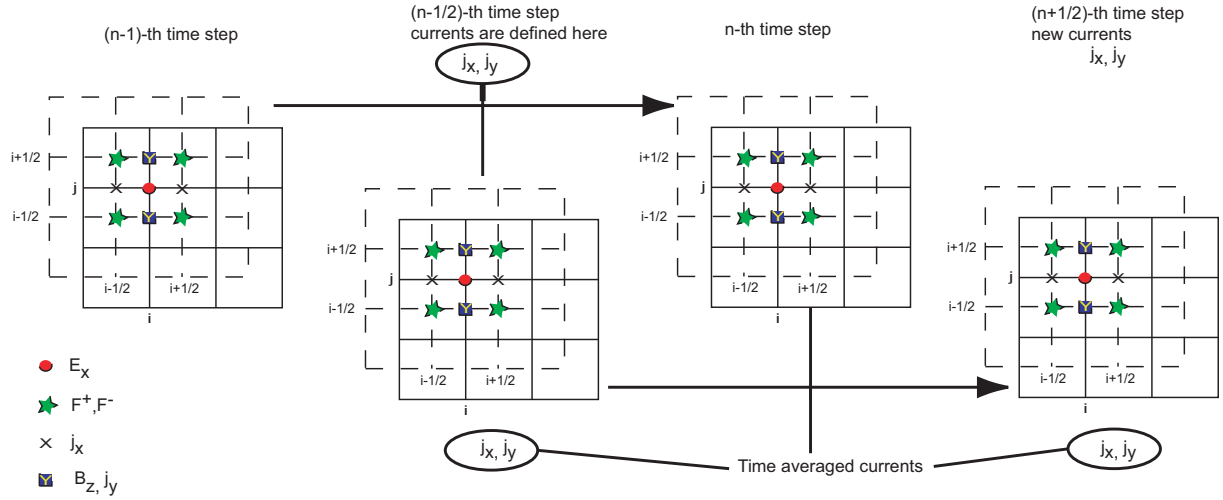


Figure 2.2: A sketch of the numerical scheme for the Maxwell equations solver.

Here, the superscripts n, i, j denote the time, longitudinal and transverse steps respectively, $B_z = 1/2(F^+ - F^-)$. The numerical method is schematically shown on fig. 2.2. In the one-dimensional case this scheme coincides with the scheme by Lichters. The new functions F^+ and F^- represent the right and left going waves respectively. By constructing the functions in such a way we get rid of numerical dispersion on the laser propagation axis and significantly simplify the longitudinal boundary conditions. For transversal boundaries the periodic conditions can be used.

2.2.2 Stability and numerical dispersion of the Maxwell equations solver.

In order to prove the stability of the numerical scheme we do the spectral analysis. One can put the following solution into eqs. (2.18, 2.19) and omit the currents:

$$E_x^{[n,i,j]} = e_x \cdot \lambda^n \cdot e^{I(k_x \cdot i \cdot \Delta x + k_y \cdot j \cdot \Delta y)} \quad (2.22)$$

$$F^{\pm[n+1/2,i+1/2,j+1/2]} = f^{\pm} \cdot \lambda^{n+1/2} \cdot e^{I(k_x \cdot (i+1/2) \cdot \Delta x + k_y \cdot (j+1/2) \cdot \Delta y)},$$

where I is the unit imaginary number. After some algebra we get the homogenous system of linear equations for amplitudes e_x, f^+, f^- (now i is the unit imaginary number)

with the following determinant

$$\begin{pmatrix} 1 - \lambda & ir_y \lambda^{1/2} \cos \frac{k_x \Delta x}{2} \sin \frac{k_y \Delta y}{2} & -ir_y \lambda^{1/2} \cos \frac{k_x \Delta x}{2} \sin \frac{k_y \Delta y}{2} \\ -r_y \lambda^{1/2} (e^{ik_y \Delta y} - 1) & \lambda e^{\frac{i(k_x \Delta x + k_y \Delta y)}{2}} - e^{\frac{i(-k_x \Delta x + k_y \Delta y)}{2}} & 0 \\ r_y \lambda^{1/2} (e^{ik_y \Delta y} - 1) & 0 & -e^{\frac{i(k_x \Delta x + k_y \Delta y)}{2}} + \lambda e^{\frac{i(-k_x \Delta x + k_y \Delta y)}{2}} \end{pmatrix}$$

where $r_y = \frac{\Delta t}{\Delta y}$. In order the homogenous system of equations has a non-trivial solution its determinant must be zero, thus we get an equation for λ :

$$\left(\lambda^2 - 2\lambda \left(2 \cos^2 \frac{k_x \Delta x}{2} \left[1 - r_y^2 \sin^2 \frac{k_y \Delta y}{2} \right] - 1 \right) + 1 \right) (\lambda - 1) = 0. \quad (2.23)$$

Solving this equation we obtain

$$\begin{aligned} \lambda &= 1 \\ \lambda &= X \pm \sqrt{X^2 - 1}, \end{aligned} \quad (2.24)$$

where $X = 2 \cos^2 \frac{k_x \Delta x}{2} (1 - r_y^2 \sin^2 \frac{k_y \Delta y}{2}) - 1$. For $r_y < 1$, $|X| < 1$, thus the root $\sqrt{X^2 - 1}$ is always imaginary and $|\lambda| = 1$ for any k_x, k_y . Therefore we proved that the scheme is stable when $r_y < 1$.

To study numerical dispersion we put $\lambda = e^{i\omega \Delta t}$ into eq. 2.24

$$\begin{aligned} e^{i\omega \Delta t} &= X + i\sqrt{1 - X^2} & e^{-i\omega \Delta t} &= X - i\sqrt{1 - X^2} \\ \frac{e^{i\omega \Delta t} + e^{-i\omega \Delta t}}{2} &= \cos(\omega \Delta t) = X \end{aligned} \quad (2.25)$$

Thus,

$$\cos^2 \frac{\omega \Delta t}{2} = \cos^2 \frac{k_x \Delta x}{2} \left(1 - r_y^2 \sin^2 \frac{k_y \Delta y}{2} \right) \quad (2.26)$$

Figure 2.3 shows the dependence of numerical speed of light in vacuum (color axis) on $k_x \Delta x$ and $k_y \Delta y$ for two different values of r_y . One can see that the waves propagating along the x -axis have no numerical dispersion that makes this scheme favorable in the

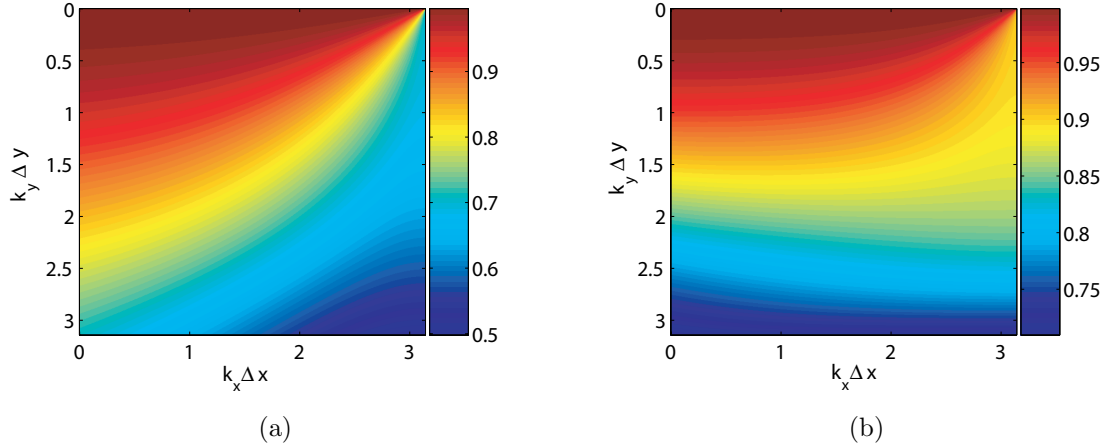


Figure 2.3: Dependance of the speed of light in vacuum on $k_x \Delta x$ and $k_y \Delta y$ for the numerical Maxwell solver according to eq. 2.26 for (a) $r_y = 0.7$ and (b) $r_y = 0.9$.

normal incidence geometry.

Test of the numerical Maxwell solver can be done using the known behavior of the gaussian beam in vacuum [102]. The beam waist of the gaussian beam is governed by the formula

$$\rho(x) = \rho_0 \cdot \sqrt{1 + \left(\frac{x - x_0}{x_d}\right)^2}, \quad (2.27)$$

where ρ_0 is the beam waist in the focus, x_0 is the position of the focus and $x_d = \pi \rho_0^2$ is the diffraction length of the beam. Figure 2.4 shows the results of the propagation of gaussian beams with $\rho_0 = 2$ (a) and $\rho_0 = 3$ (b) obtained from the numerical simulations (grayscale image) and from the formula 2.27. The results show good agreement between simulations and theory.

2.2.3 Numerical scheme for equations of motion.

For the numerical integration of equations of motion the Boris scheme [103] is used (which is also described by Lichters [100]). First the half-acceleration in electric field only is applied giving

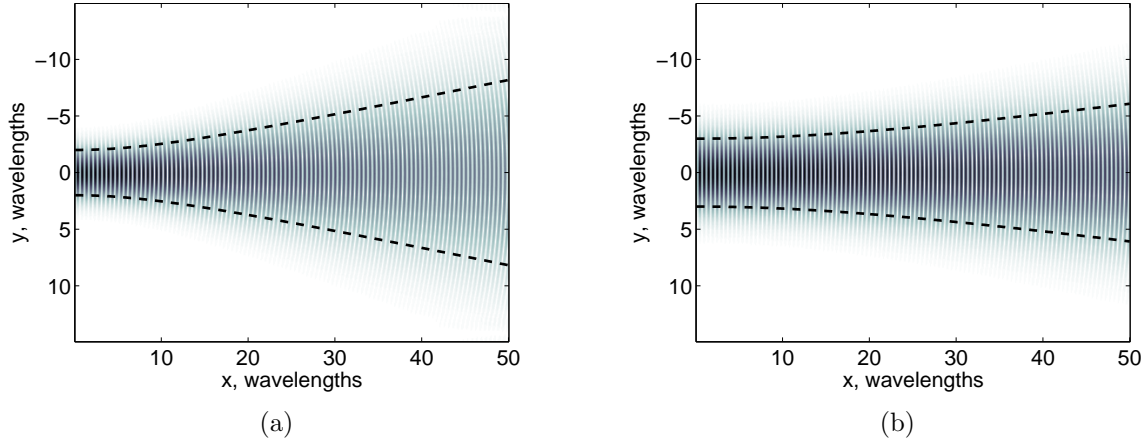


Figure 2.4: Propagation of gaussian beams with $\rho_0 = 2$ (a) and $\rho_0 = 3$ (b) in vacuum according to simulations (grayscale) and the formulas of gaussian optics (dashed lines).

$$\mathbf{p}^- = \mathbf{p}^{n-1/2} + \frac{q}{2} \mathbf{E}^n \Delta t.$$

Then the two-step rotation in magnetic field is done

$$\begin{aligned} \mathbf{p}' &= \mathbf{p}^- + \mathbf{p}^- \times \mathbf{t} \\ \mathbf{p}^+ &= \mathbf{p}^- + \mathbf{p}' \times \mathbf{s}, \end{aligned}$$

where $\mathbf{t} = \mathbf{B}q\Delta t/2\gamma^n$ and $\mathbf{s} = 2\mathbf{t}/(1 + \mathbf{t}^2)$. Finally, the new momenta is found from

$$\mathbf{p}^{n+1/2} = \mathbf{p}^+ + \frac{q}{2} \mathbf{E}^n \Delta t.$$

The new particle positions are found by integrating the momenta

$$\mathbf{r}^{n+1} = \mathbf{r}^n + \frac{\mathbf{p}^{n+1/2}}{m\gamma^{n+1/2}},$$

where $\gamma^{n+1/2} = \sqrt{1 + (\mathbf{p}^{n+1/2})^2}$.

The motion of a free electron in the plane electromagnetic wave is a well known problem and has analytical solutions [4, 5]. Thus it can be used for testing of the numerical solver for equations of motion.

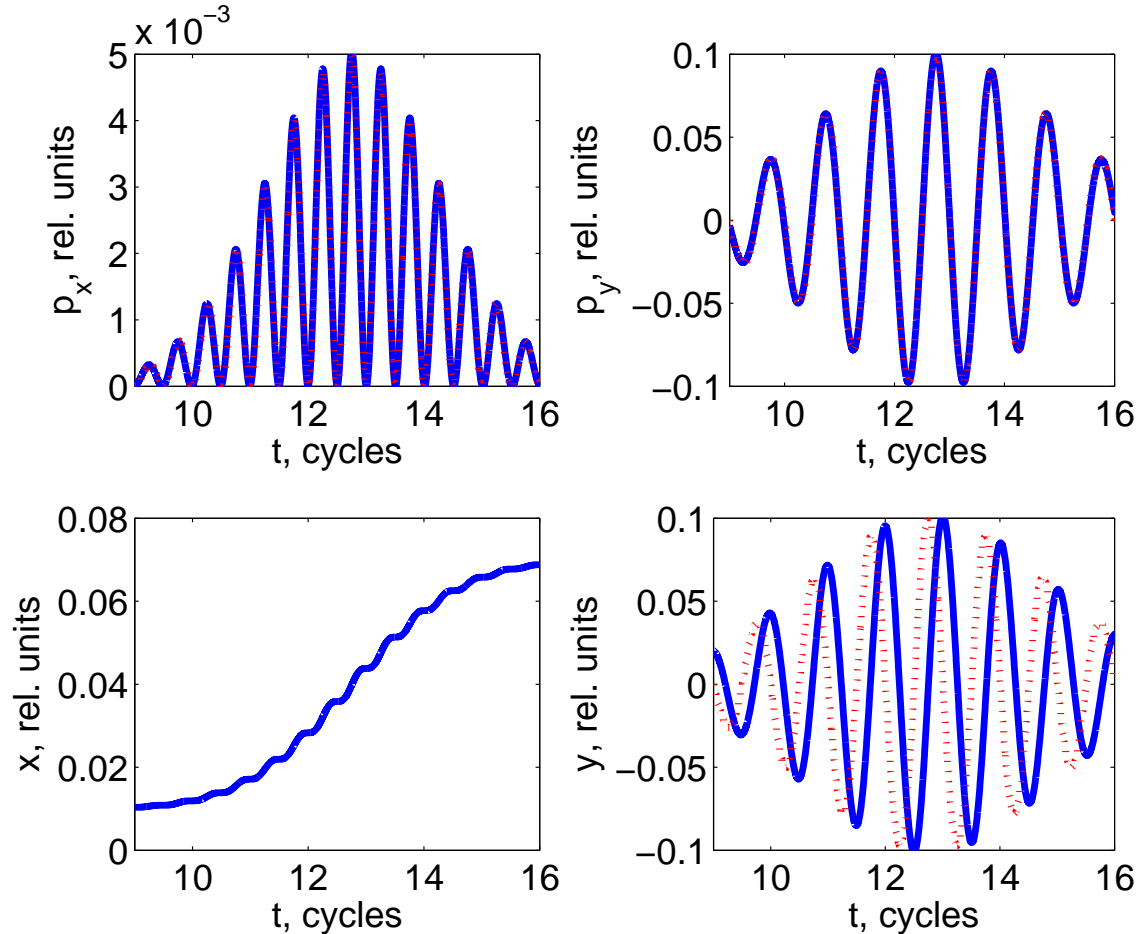


Figure 2.5: Results of the numerical simulations of the free electron motion in the electromagnetic pulse with $a_0 = 0.1$ and FWHM-duration of the electric field $T_{FWHM} = 5$ cycles.

For the electron initially at rest at x_0 irradiated by the linear polarized laser pulse propagating along the x axis the solutions read

$$\begin{aligned} x(\xi) &= x_0 + \frac{1}{2} \int \frac{a_y^2(\xi)}{\gamma(\xi)} d\xi \\ t(\xi) &= \xi + \frac{1}{2} \int \frac{a_y^2(\xi)}{\gamma(\xi)} d\xi \\ p_y(\xi) &= a_y(\xi) \\ p_x(\xi) &= \frac{1}{2\gamma(\xi)} a_y^2(\xi), \end{aligned} \tag{2.28}$$

where $a_y(\xi)$ - is the vector potential of the electromagnetic waves, p_x, p_y - the kinematical momenta components of the electron. The results of the numerical simulations for the laser pulse with $a_0 = 0.1$ and full-width-half-maximum (FWHM) duration of 5 cycles are presented on fig. 2.5. In this case the γ - factor in eqns. 2.28 is equal to 1 with high accuracy. Lower-left figure demonstrates the electron drift in the longitudinal direction with double the laser frequency. Lower-right figure shows the dependance of the y coordinate (which is simply the integration of p_y in this case) on time (solid line) as well as the laser vector potential (dotted line). One can see the phase difference of $\pi/2$ as predicted by the theory.

Upper figures show the evolution of the momenta components p_x (left) and p_y (right) with time obtained from the numerical simulations (solid line) and from eqns. 2.28 (dotted line). Results of the simulations exhibit good agreement with the analytical solutions.

2.2.4 Current deposition.

By moving, the particles produce currents. As the particle coordinates change continuously it is important to connect them to the Eulerian grid where the fields are defined. There are several *local* numerical current deposition schemes (*charge conservation schemes*) that allow to avoid solving the Poisson equation every time step [98, 97]. One of them is called the *zigzag* scheme and was proposed by Umeda *et al* [96].

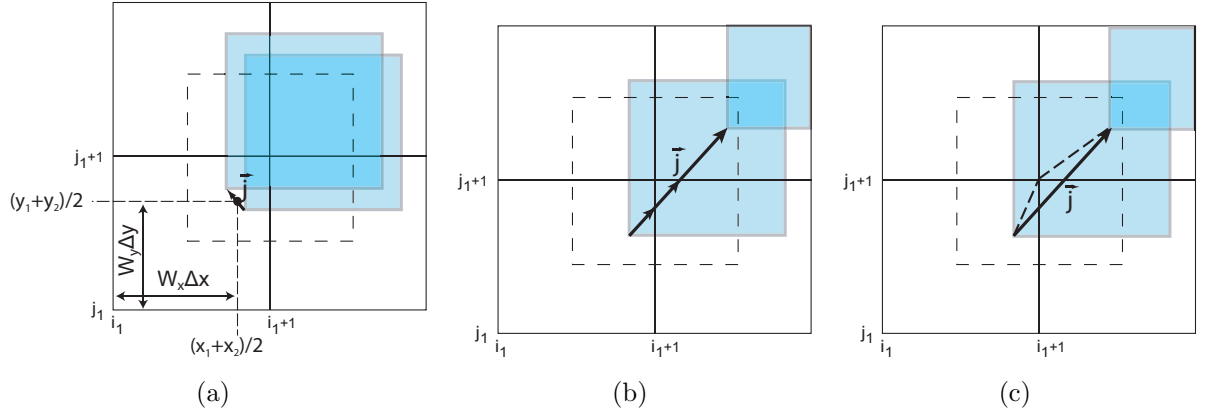


Figure 2.6: Current deposition schematics. (a) Particle remains in the same cell; (b),(c) particle changes the cell in both x and y directions. On sub-figure (b) the particle motion is assumed to be a straight line and described as the motion of 3 sub-particles, on sub-figure (c) the particle trajectory is assumed to be a zigzag line and is described by the motion of 2 sub-particles.

The continuity equation in discrete form reads

$$\frac{\rho^{[n+1,i,j]} - \rho^{[n,i,j]}}{\Delta t} + \frac{j_x^{[n+1/2,i+1/2,j]} - j_x^{[n+1/2,i-1/2,j]}}{\Delta x} + \frac{j_y^{[n+1/2,i,j+1/2]} - j_y^{[n+1/2,i,j-1/2]}}{\Delta y} = 0. \quad (2.29)$$

Let's assume the particle has a rectangular shape and moves from position (x_1, y_1) to (x_2, y_2) . Let's also assume that the point (x_1, y_1) belongs to the cell with coordinates (i_1, j_1) and (x_2, y_2) belongs to the cell with coordinates (i_2, j_2) . Depending on the end position of the particle i_2 and j_2 can be equal to i_1 and j_1 respectively or be different. Maximum displacement δ of the particle can not be more than the cell spacings Δx and Δy as the particle can not move faster than with the speed of light in vacuum.

Let's first discuss the density deposition. As one can see from the schematic drawing on fig. 2.6a the particle with coordinates (x_1, y_1) occupies four cells. One can define the weighting coefficients

$$W_x^n = \frac{x_1 - i_1 \Delta x}{\Delta x} \quad W_y^n = \frac{y_1 - j_1 \Delta y}{\Delta y}. \quad (2.30)$$

This coefficients (both less than one) define what part of the particle lies in the certain cell

in the following way

$$\begin{aligned}\rho^{[n, i_1, j_1]} &= q \cdot (1 - W_x^n)(1 - W_y^n) & \rho^{[n, i_1+1, j_1]} &= q \cdot W_x^n(1 - W_y^n) \\ \rho^{[n, i_1, j_1+1]} &= q \cdot (1 - W_x^n)W_y^n & \rho^{[n, i_1+1, j_1+1]} &= q \cdot W_x^nW_y^n.\end{aligned}\quad (2.31)$$

Let's now discuss the current deposition. The simplest case - when the particle remains in the same cell while moving, is schematically shown on fig. 2.6a. The current is assigned to four points: j_x is assigned to points $(i_1 + 1/2, j_1)$ and $(i_1 + 1/2, j_1 + 1/2)$ and j_y is assigned to $(i_1, j_1 + 1/2)$ and $(i_1 + 1, j_1 + 1/2)$. The total current density in both directions is given by

$$F_x = qv_x = q \frac{x_2 - x_1}{\Delta t} \quad F_y = qv_y = q \frac{y_2 - y_1}{\Delta t} \quad (2.32)$$

and the weighting is done at the time step $n + 1/2$ - the moment when the particle was in the middle of its trajectory, thus

$$W_x = \frac{x_1 + x_2}{2\Delta x} - i_1 \quad W_y = \frac{y_1 + y_2}{2\Delta y} - j_1. \quad (2.33)$$

The current density is then deposited on the grid in the following way

$$\begin{aligned}j_x^{[n+1/2, i_1+1/2, j_1]} &= qF_x(1 - W_y) & j_x^{[n+1/2, i_1+1/2, j_1+1]} &= qF_xW_y \\ j_y^{[n+1/2, i_1, j_1+1/2]} &= qF_y(1 - W_x) & j_x^{[n+1/2, i_1+1, j_1+1/2]} &= qF_yW_x.\end{aligned}\quad (2.34)$$

When the particle moves across the cell walls, the situation becomes a bit more complicated, but its trajectory can be viewed as a motion of several particles. In the method proposed by Villasenor and Buneman [98] the particle trajectory is always assumed to be a straight line. For example on fig. 2.6b the particle motion is described as motion of three *sub-particles*, each moving along the straight line with start and end coordinates located within the same cell. This algorithm has a major drawback as it uses the conditional operators in its implementation, which generally take a lot of computational time.

Umeda *et al.* suggested that the particle trajectory "needs not to be a straight" line and developed a new charge-conservation scheme called the *zigzag method* [96]. The idea

behind this method is to separate the motion into the motion of two *sub-particles*, one moving from the start to the intermediate point (the relay point) and the other moving from the relay point to the end position (see fig. 2.6c).

Let's consider the case when the particle changes the cell in both x and y directions. Other variants are done in analogy. As shown on fig. 2.6c we split the trajectory of one particle into the motion of two sub-particles, one moving from (x_1, y_1) to a relay point $((i_1 + 1)\Delta x, (j_1 + 1)\Delta y)$, and another one from the relay point to (x_2, y_2) . The particle trajectory becomes a zigzag-line. For each of the sub-particles we can now repeat the simple procedure of eq. 2.34. This current deposition scheme is much easier in implementation than the Villasenor and Buneman scheme and allows to avoid the conditional operators.

All four cases can be united by defining the relay point for each case. For example, in one-dimensional case, the relay point x_r is given by

$$x_r = \begin{cases} \frac{x_1 + x_2}{2} & \text{if the particle remains in the same cell} \\ \max(i_1 \Delta x, i_2 \Delta x) & \text{otherwise,} \end{cases}$$

so the relay point is located either in the middle of the straight-line trajectory if the particle remains in the same cell, or in one of the grid points $i_1 \Delta x$ or $i_2 \Delta x$ depending on the direction of particle motion.

In two-dimensional case Umeda *et al* show that the relay point can be defined analogously to the one-dimensional case without the conditional operators:

$$x_r = \min \left[\min(i_1 \Delta x, i_2 \Delta x) + \Delta x, \max \left(\max(i_1 \Delta x, i_2 \Delta x), \frac{x_1 + x_2}{2} \right) \right]$$

$$y_r = \min \left[\min(i_1 \Delta y, i_2 \Delta y) + \Delta y, \max \left(\max(i_1 \Delta y, i_2 \Delta y), \frac{y_1 + y_2}{2} \right) \right].$$

The current density is then decomposed into

$$F_{x_1} = q \frac{x_r - x_1}{\Delta t}, \quad F_{y_1} = q \frac{y_r - y_1}{\Delta t}$$

$$F_{x_2} = q \frac{x_2 - x_r}{\Delta t}, \quad F_{y_2} = q \frac{y_2 - y_r}{\Delta t}.$$

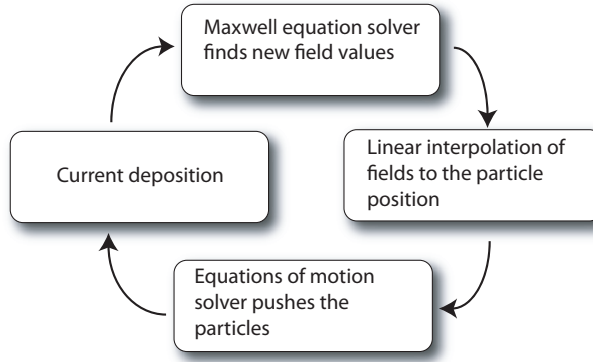


Figure 2.7: The routine of one time step in the particle-in-cell code.

Combined with the linear weighting coefficients

$$\begin{aligned} W_{x_1} &= \frac{x_1 + x_r}{2\Delta x} - i_1, & W_{y_1} &= \frac{y_1 + y_r}{2\Delta y} - j_1 \\ W_{x_2} &= \frac{x_r + x_2}{2\Delta x} - i_2, & W_{y_2} &= \frac{y_r + y_2}{2\Delta y} - j_2. \end{aligned}$$

the currents at 8 grid points can be obtained from

$$\begin{aligned} j_x^{[i_1+1/2, j_1]} &= F_{x_1}(1 - W_{y_1}), & j_x^{[i_1+1/2, j_1+1]} &= F_{x_1}W_{y_1} \\ j_x^{[i_2+1/2, j_2]} &= F_{x_2}(1 - W_{y_2}), & j_x^{[i_2+1/2, j_2+1]} &= F_{x_2}W_{y_2} \\ j_y^{[i_1, j_1+1/2]} &= F_{y_1}(1 - W_{x_1}), & j_y^{[i_1+1, j_1+1/2]} &= F_{y_1}W_{x_1} \\ j_y^{[i_2, j_2+1/2]} &= F_{y_2}(1 - W_{x_2}), & j_y^{[i_2+1, j_2+1/2]} &= F_{y_2}W_{x_2}. \end{aligned}$$

By obtaining the currents one time step ends and the next one starts again with solving the Maxwell equations using new currents values. Thus one time-cycle of the particle-in-cell method can be schematically drawn as on fig. 2.7.

2.2.5 Decay of the electromagnetic wave in the skin layer of the overdense plasma.

For testing the operation of all four routines of the PIC code one can use the known law of decay of electromagnetic waves in the overdense plasmas. In the case of non-collisional

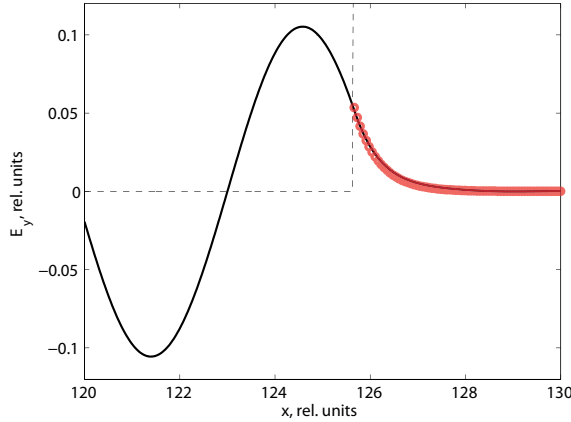


Figure 2.8: Results of the numerical simulations showing the decay of the electromagnetic field with $a_0 = 0.1$ inside the overdense plasma with density $n = 4$. Dashed line outlines the vacuum-plasma interface, solid line shows the electric field of the incoming (from left to right) laser pulse and red circles are obtained from eq. 2.35.

plasma its dielectric permeability is in simple case given by

$$\varepsilon(\omega) = 1 - \frac{n}{n_{cr}} = 1 - \frac{\omega_p^2}{\omega^2},$$

where n is the plasma density and n_{cr} is the critical density (the density for which the plasma frequency $\omega_p = \sqrt{n}$ is equal to the electromagnetic wave frequency). This dependence of permeability on frequency ω leads to the well-known exponential decay for $\omega < \omega_p$

$$E_y(t, x) = A \cdot e^{i\omega t} \cdot e^{-\frac{x}{l_s}}, \quad (2.35)$$

where $l_s = 1/\omega_p = 1/\sqrt{n}$ is the skin depth.

The comparison of the PIC simulation results (solid line) with the formula 2.35 (red circles) is shown on fig. 2.8. It exhibits good agreement.

2.3 Summary of the chapter

In this chapter the main equations and methods of numerical simulations are described. According to the numerical schemes described above the numerical code PICWIG was

written that allows to simulate the interaction of intense laser pulses with collisionless fully-ionized plasma in 1D and 2D geometries. All the simulation results presented in this thesis were obtained using this code.

Chapter 3

Generation of high-order harmonics on the plasma-vacuum boundary.

3.1 Oscillating Mirror (OM) harmonics

3.1.1 One-particle mirror model

Albert Einstein [104] showed that the reflection of electromagnetic wave from a moving mirror results in a frequency shift of $(1 + \beta)/(1 - \beta)$ with β the speed of the mirror. If the mirror moves periodically, for example with the period of the incoming wave, than constructive and destructive interference would lead to the appearance of the spectrum exhibiting harmonics of the fundamental wave frequency. This scenario is happening when a relativistically strong laser pulse is incident onto the overdense plasma surface, where surface oscillations arise as a result of the interplay between laser pressure and the restoring force from the ions. This simple concept of oscillating surface was proposed by Bulanov *et al* [31] and became a working horse in explanation of the phenomena. It was later followed by the detailed discussions by Lichters *et al* [105], Tsakiris *et al* [106], Gordienko *et al* [107] and Baeva *et al* [108].

In order to understand the basic properties of the surface motion one can use the simple one dimensional one particle model, which describes the longitudinal motion of the

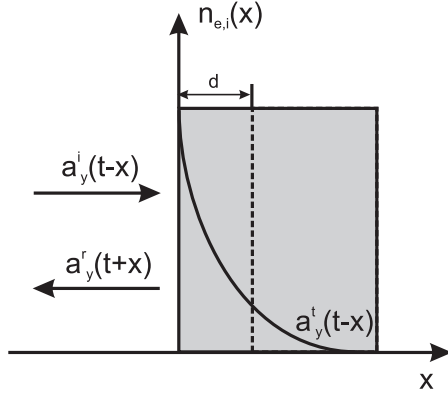


Figure 3.1: One-particle plasma surface model schematics showing the plasma-vacuum interface. The laser pulse is normally incident from the left side, part of it is reflected and part of it decays in the skin-layer of the target. Separation of the electrons from the ions results in longitudinal electrostatic field proportional to the separation length d .

incompressible electron layer relative to the immobile ion layer under the influence of the linearly polarized laser pulse incident normally. From the Poisson equation it is easy to find that the charge-separation potential is proportional to x^2 , where x - is the electron layer displacement. The Lagrangian of such a system in relativistic units reads

$$\mathcal{L}(t, x, \beta_x, \beta_y) = -\sqrt{1 - \beta^2} - a_y(t, x) \cdot \beta_y - 0.5 \cdot n \cdot x^2, \quad (3.1)$$

where $a_y(t, x)$ is the driving vector potential and n is the plasma density which defines the restoring force. Similar models were used by Zaretsky *et al* [109] for studies of Landau damping in thin foils and by Mulser *et al* [110] for studies of the laser absorption mechanisms.

First we note that Lagrangian (3.1) does not depend on the transverse coordinate y thus leading to the momentum conservation

$$p_y = a_y(t, x). \quad (3.2)$$

Using the Euler-Lagrange equation one can obtain the equation of motion

$$\frac{dp_x}{dt} = -\beta_y \frac{\partial a_y}{\partial x} - nx. \quad (3.3)$$

Using the equation for energy variation

$$\frac{d\gamma}{dt} = \beta_y \frac{\partial a_y}{\partial t} - \beta_x n x,$$

and the connection $\beta_{x,y} = p_{x,y}/\gamma$, left part of eq. (3.3) can be rewritten in the following form

$$\begin{aligned} \frac{dp_x}{dt} &= \frac{d(\gamma\beta_x)}{dt} = \gamma \frac{d\beta_x}{dt} + \beta_x \frac{d\gamma}{dt} = \\ &= \gamma \frac{d\beta_x}{dt} + \beta_x \left(\beta_y \frac{\partial a_y}{\partial t} - \beta_x n x \right) = \gamma \frac{d\beta_x}{dt} + \frac{\beta_x}{2\gamma} \frac{\partial a_y^2}{\partial t} - \beta_x^2 n x. \end{aligned}$$

Thus, eq. (3.3) after transformations reads

$$\frac{d\beta_x}{dt} = -\frac{1}{2\gamma^2} \left(\frac{\partial a_y^2}{\partial x} + \beta_x \frac{\partial a_y^2}{\partial t} \right) - \frac{nx}{\gamma} (1 - \beta_x^2) \quad (3.4)$$

Representing the gamma-factor in the form $\gamma = (1 + a_y^2) / (1 - \beta_x^2)$, we get an equation for coordinate x

$$\ddot{x} = -\frac{1 - \dot{x}^2}{2(1 + a_y^2)} \left(\frac{\partial a_y^2}{\partial x} + \dot{x} \frac{\partial a_y^2}{\partial t} \right) - \frac{nx(1 - \dot{x}^2)^{3/2}}{\sqrt{1 + a_y^2}} \quad (3.5)$$

with initial conditions

$$\begin{aligned} x(0) &= 0 \\ \beta_x(0) &= 0. \end{aligned} \quad (3.6)$$

In equation 3.5 a_y is the driving vector potential which is the result of the interference between the incoming and reflected light. In the following we assume that plasma surface possesses 100 percent reflectivity.

If one takes the incoming vector potential $a_y^i(t, x)$ in the form $a_y^i(t, x) = -E_i \cdot \sin(t - x)$, then electric and magnetic fields are given by expressions

$$E_{y,inc} = E_i \cdot \cos(t - x)$$

$$B_{z,inc} = E_i \cdot \cos(t - x).$$

For the reflected light one can write

$$\begin{aligned} E_{y,refl} &= E_r \cdot \cos(t + x + \phi_r) \\ B_{z,refl} &= -E_r \cdot \cos(t + x + \phi_r), \end{aligned} \quad (3.7)$$

and for transmitted light

$$\begin{aligned} E_{y,trans} &= E_t \cdot \cos(t + \phi_t) \cdot e^{-\frac{x-x_p}{l_s}} \\ B_{z,trans} &= \frac{E_t}{l_s} \cdot \sin(t + \phi_t) \cdot e^{-\frac{x-x_p}{l_s}}, \end{aligned}$$

where $l_s = 1/\omega_p = 1/\sqrt{n}$ - is the depth of the skin-layer, $\omega_p > 1$ is the plasma frequency. As the boundary condition one can use the continuity of the electromagnetic fields on the plasma-vacuum boundary ($x = x_p$):

$$\begin{aligned} E_i \cdot \cos(t - x_p) + E_r \cdot \cos(t + x_p + \phi_r) &= E_t \cdot \cos(t + \phi_t) \\ E_i \cdot \cos(t - x_p) - E_r \cdot \cos(t + x_p + \phi_r) &= \frac{E_t}{l_s} \cdot \sin(t + \phi_t) \end{aligned}$$

Using the formulae of trigonometry one gets the following values for amplitudes and phases

$$\begin{aligned} E_i &= E_r \\ E_t &= \frac{2E_i}{\sqrt{1 + \omega_p^2}} \\ \phi_t &= \alpha - x_p \\ \phi_r &= 2(\alpha - x_p), \end{aligned}$$

where $\alpha = \arctan(\omega_p)$.

Formally, in the relativistic case we are not allowed to use the simple expression for the skin-depth $l_s = 1/\omega_p$ and have to take into account the relativistic corrections. However, from the expression for E_t we see that the plasma screens the incoming field and the amplitude of the field on the surface is ω_p times lower than the amplitude of the incoming

light. Thus the linear expression for the skin-depth can be used when $a_0 < \omega_p$. When the amplitude a_0 exceeds ω_p , the relativistic correction to the skin-depth can be made taking into account the change of the electron energy

$$\begin{aligned}\omega_p &= \frac{\sqrt{n}}{\sqrt{m\gamma}} = \frac{\sqrt{n}}{\sqrt{\gamma}} \\ l_s &= \sqrt{\frac{\gamma}{n}} \\ \gamma &\approx \sqrt{1 + E_t^2}\end{aligned}\tag{3.8}$$

The field on the plasma surface is the result of the interference of the incoming and reflected light

$$\begin{aligned}E_{dr} &= E_{refl} + E_{inc} = E_i \cdot \cos(t - x_p) + E_i \cdot \cos(t - x_p + 2\alpha) = \\ &= 2E_i \cdot \cos(t - x_p + \alpha) \cos \alpha \\ B_{dr} &= B_{refl} + B_{inc} = E_i \cdot \cos(t - x_p) - E_i \cdot \cos(t - x_p + 2\alpha) = \\ &= 2E_i \cdot \sin(t - x_p + \alpha) \sin \alpha,\end{aligned}\tag{3.9}$$

thus

$$\begin{aligned}E_{dr} &= \frac{2E_i}{\sqrt{1 + \omega_p^2}} \cos(t - x_p + \alpha) \\ B_{dr} &= \frac{2\omega_p E_i}{\sqrt{1 + \omega_p^2}} \sin(t - x_p + \alpha)\end{aligned}\tag{3.10}$$

Vector potential inside plasma (for $x > x_p$) can be written in the following form

$$a_{trans} = -\frac{2E_i}{\sqrt{1 + \omega_p^2}} \sin(t - x_p + \alpha) \cdot e^{-\omega_p(x - x_p)}\tag{3.11}$$

Vector potential driving the surface can be obtained from eq. 3.11 by putting $x = x_p$. Using the trigonometry formulae eq. (3.5) can be rewritten in the form

$$\ddot{x} = (1 - \dot{x}^2) \cdot F_{dr} - nx(1 - \dot{x}^2)^{3/2} \cdot F_r\tag{3.12}$$

where $F_{dr} = (2E_i^2 \omega_p [1 - \cos(2(t - x_p + \alpha) - \theta)]) / [(1 + a_{dr}^2)(1 + \omega_p^2)]$, and $F_r = 1 / \sqrt{1 + a_{dr}^2}$.

When $\dot{x} \ll 1$ this equation allows the analytical solution. In this case eq. (3.12) reads

$$\ddot{x} + nx = \frac{2E_i^2\omega_p}{1 + \omega_p^2}(1 - \cos 2\tau), \quad (3.13)$$

where $\tau = t - x_p + \alpha$. From this equation the amplitude of the longitudinal oscillations X for small a_0 can be easily obtained

$$X = \frac{2E_i^2\sqrt{n}}{(1+n)(n-4)} + \frac{2E_i^2\sqrt{n}}{n(n+1)} \approx 2E_i^2 n^{-3/2}. \quad (3.14)$$

In the case when $n = 4$ formally we can not write the solution in this form, but after taking into account dissipation in some form we can see the well-known two photon plasma resonance [55]. Amplitude of the transverse oscillations Y in the case of small a_0 is easy to find from the equation $\dot{y} = a_y$:

$$Y = \frac{2E_i}{\sqrt{1 + \omega_p^2}} \approx 2E_i n^{-1/2} \quad (3.15)$$

In the general case eq. 3.12 requires a numerical solution. Results of the model calculations are presented on fig. 3.2. Trajectory of the electron during the interaction with the laser pulse with amplitude $a_0 = 10$ (corresponding to the intensity of $1.37 \cdot 10^{20} \text{ W/cm}^2$ for the laser with the wavelength $\lambda_L = 1 \mu\text{m}$), with a gaussian envelope and a 4-cycles FWHM duration is shown on fig. 3.2a. Plasma density is $n_e = 400$. Fig. 3.2b shows the transverse coordinate y_e as a function of time t . On fig. 3.2c the solid line shows the longitudinal coordinate x_e (horizontal axis) as a function of time t (vertical axis).

Dependence of the amplitude of the longitudinal X and transverse Y electron motion on the laser pulse amplitude a_0 for plasma density $n_e = 400$ are shown on fig. 3.3. On both figures the diamonds represent the result of numerical solutions of the model equations and dashed lines represent low a_0 asymptotic solutions (eqns. 3.14 and 3.15). On fig. 3.3a the circles show the results of the model with the relativistic skin-layer corrections taken into account. The simple estimates of eqns. 3.14 and 3.15 work well until the value of approximately $a_0 = \omega_p/2$. After that the relativistic corrections to the skin depth and

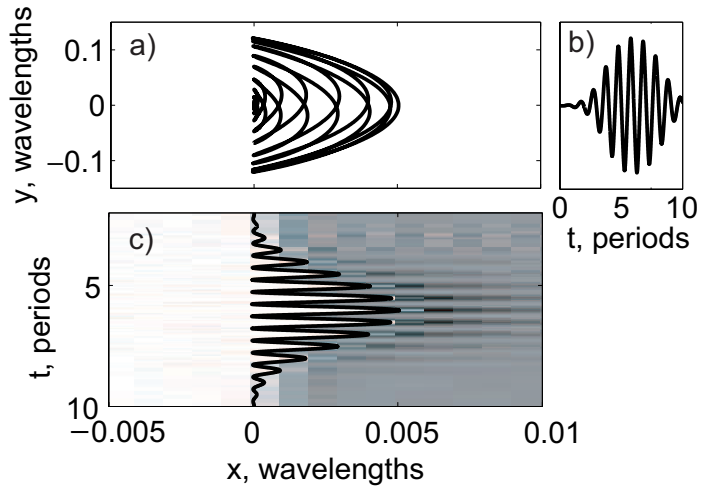


Figure 3.2: Electron motion obtained using the single particle model for laser pulse with $a_0 = 10$ with 4 cycles FWHM-duration and $n_e = 400$. Electron is initially located at $x_e = y_e = 0$. Subfigure (a) shows the electron trajectory, subfigure (b) demonstrates the behaviour of the transverse coordinate y_e in time, on subfigure (c) the dashed line represents the longitudinal coordinate x_e of the electron (vertical axis) versus time (horizontal axis) obtained from the model, the color coded image displays the spatio-temporal picture of the electron density obtained from 1D-PIC simulations with same laser and plasma parameters.

electron longitudinal motion become important.

In order to check the validity of the afore-described model we have conducted a series of 1D PIC simulations. The code described in Chapter 2 allows the simulation of the interaction of the intense laser pulses with pre-ionized non-collisional plasma. The density in the simulations is $n = 400$, step-like vacuum-plasma interface is assumed, the ions are immobile. Throughout the thesis we use FWHM of the electric field as the definition of the laser pulse duration and use pulses with an electric field that has a Gaussian envelope function. The results are presented on fig. 3.2 and fig. 3.3. The color-coded image on fig. 3.2c presents the spatio-temporal picture of the electron density obtained from simulations with the same laser and plasma parameters as in the model (solid-line). One can see that the model is in perfect agreement with the PIC simulations. Fig. 3.3a,b show the amplitude of electron longitudinal X and transverse Y oscillations respectively as a function of a_0

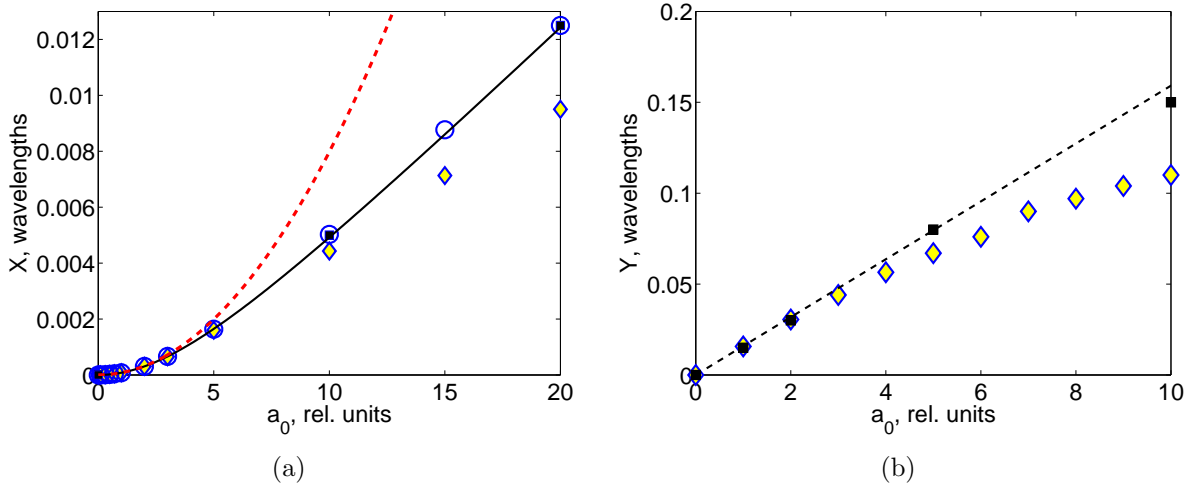


Figure 3.3: Amplitudes of longitudinal (a) and transverse (b) oscillations as functions of laser amplitude a_0 . On both subfigures diamonds represent the numerical solutions of the model equations, squares represent the results of the PIC simulations, dashed lines - the results of the analytical solutions of the model equations for low a_0 . On subfigure (a) the circles are obtained from numerical solutions of the model equations including the relativistic corrections to the skin-depth, solid line represents the capacitor model. Plasma density is $n = 400$.

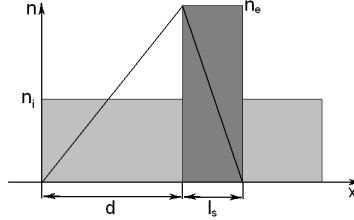


Figure 3.4: Schematics of the capacitor model.

obtained from PIC simulations (squares). The fact that the simulation results lie on the curve obtained from the model and as longitudinal motion is directly correlated to the transverse motion allows us to claim that the model works well and gives correct results for both longitudinal and transverse coordinates. Latter are hard to obtain from 1D PIC simulations as the particles leave the interaction region and are very intricate to trace.

It is interesting that the amplitude of the longitudinal oscillations X can be found from a different point of view - using the balance of the longitudinal charge-separation field and laser pressure. Laser pressure leads to the displacement and compression of the electron

layer inside the target to the depth d (see fig. 3.4). The density of the compressed electron layer is denoted as $n_{compressed}$, the characteristic size of the compressed layer is equal to the skin depth l_s . Writing down the condition of plasma neutrality we get

$$n_{compressed} \cdot l_s = n_0 \cdot (d + l_s). \quad (3.16)$$

Electrostatic field that arises when the electron layer is displaced by the length d is given by $E_{es} = n_0 \cdot d$, where n_0 is initial plasma density. Writing down the balance between laser pressure and electrostatic pressure we obtain

$$\frac{n_{compressed} \cdot l_s \cdot n_0 \cdot d}{2} = (1 + R)E_0^2 \approx 2E_0^2, \quad (3.17)$$

where R is the reflection coefficient which is assumed to be unity. Using eq. 3.16 we get the following equation for displacement d :

$$d^2 + l_s \cdot d - \frac{4E_0^2}{n_0^2} = 0, \quad (3.18)$$

with the solution in the following form

$$d = -\frac{1}{2\sqrt{n_0}} + \frac{1}{2}\sqrt{\frac{1}{n_0} + \frac{16E_0^2}{n_0^2}}. \quad (3.19)$$

Amplitude of longitudinal surface oscillation obtained from this (capacitor) model is shown on fig. 3.3a with a solid line. The results of PIC simulations, the simple mirror model and the capacitor model are in perfect agreement. Capacitor model is later used in this thesis for studies of the ion acceleration process.

3.1.2 Emission of harmonic spectrum.

The simple one particle model described above allows to understand the generation of high-order harmonics from both macroscopic and microscopic points of view.

Taking into consideration only the longitudinal motion of the surface and applying the boundary conditions for reflected light from eq. 3.7 one gets for reflected electric field

$$E_{refl} = E_i \cdot \cos(t - x(t') + 2\alpha), \quad (3.20)$$

where $t' = t + x(t')$ is the "meeting" time of the wave and the electron. Presence of the nonlinear term $x(t')$ inside the cosine function makes the right part of this equation nonlinear and exhibits harmonic spectra if $x(t')$ is periodic. For the spectrum of the reflected light one can write

$$E(q) = \frac{E_i}{2\sqrt{2\pi}} \int_{-\infty}^{\infty} e^{i(t-x(t')+2\alpha-qt)} dt + c.c. \quad (3.21)$$

The behavior of this integral for high frequencies $q \gg 1$ and high mirror velocities (approaching the speed of light) does not depend on the exact mirror motion function $x(t')$ and can be found using the standard asymptotic methods [111]. Gordienko *et al* [107] and later Baeva *et al* [108] showed that the spectrum is universal and exhibits a certain frequency dependance - it decays proportionally to $q^{-5/2}$ or $q^{-8/3}$. Moreover, the spectrum extends up to a certain cut-off frequency ω_{co} that is proportional to the γ^3 , where γ is the relativistic gamma-factor of the mirror, followed by the exponential roll-off. The integral in eq. 3.21 can also be taken numerically assuming the mirror motion function $x(t')$ in some form as shown in the paper by Tsakiris *et al* [106]. It shows the same frequency dependance and the cut-off frequency. As the moments when the surface moves towards the laser and has the highest longitudinal velocity are strongly localized in time, the Doppler shift produces a flash of harmonics with the attosecond duration [106].

Another way of looking at the emission of harmonics is from a more microscopic point of view. Although the model described above deals with the incompressible electron layer and not with the individual microscopical electron, we can assume that all the electrons within the skin layer are doing the same arc-like trajectories. Given the trajectory of the electron one can find the radiation it produces with the help of Lienard-Wiechert potentials [4]. Electric field is given by the following expression

$$E(\mathbf{x}_d, t) = - \left[\frac{(\mathbf{n} - \boldsymbol{\beta})(1 - \beta^2)}{\kappa^3 R^2} \right]_{ret} - \left[\frac{\mathbf{n}}{\kappa^3 R} \times ((\mathbf{n} - \boldsymbol{\beta}) \times \mathbf{w}) \right]_{ret}, \quad (3.22)$$

where \mathbf{x}_d - is the position of the detector, $\mathbf{n} = \mathbf{R}/R$, where \mathbf{R} is the radius vector pointing from the detector to the particle, $\boldsymbol{\beta}$ and \mathbf{w} are the electron velocity and acceleration respectively and $\kappa = 1 - \mathbf{n}\boldsymbol{\beta}$. The quantities in square brackets are taken in the retarded time. For large distances we can neglect the first term in the right part of eq. 3.22 as it scales with R^2 and is not responsible for the generation of electromagnetic waves [4]. As for the second part, we have to remember that the surface in 1D case is infinite in the transverse direction, so we only look at the transverse electric field component E_y and put a detector at position with $y_d = 0$ (the electron is supposed to be initially at rest at $x = 0, y = 0$). For $R \gg 1$ one can set $n_x = 1$ and $n_y = 0$ and write for $E_y(x_d, t)$

$$E_y(x_d, t) = E_0 \cdot [w_y \cdot (1 - \beta_x) + w_x \cdot \beta_y]_{ret}, \quad (3.23)$$

where $E_0 \approx 1/\kappa^3 R$. All functions on the right side of the equation are nonlinear as they depend on $t' = t + x(t')$. This leads to emission of harmonic spectrum. For example, for non-relativistic mirror motion case w_y is the analogue to the electric field on the surface ($w_y = \dot{p}_y = \dot{a}_y$) and has the same form as in eq. 3.20.

Equation 3.23 can be solved numerically for arbitrary electron trajectories. As a test one can numerically solve eq. 3.23 for an electron oscillating with a certain frequency only in transverse direction y and assure the well-known $\cos^2(\theta)$ law for angular distribution [4]. Figure 3.5a shows the results of the numerical solution of eq. 3.23 (circles) compared with the $\cos^2(\theta)$ formula (solid line) and exhibits perfect agreement. The dipole oscillating in transverse direction with fundamental frequency radiates at the same frequency. As the electron starts slightly wiggling in the longitudinal direction the radiation exhibits a broad spectrum. From fig. 3.2c one can see that the electron amplitude in longitudinal direction is not high and so is the amplitude of the longitudinal velocity. Nevertheless, the nonlinearity due to the longitudinal motion is enough to produce the harmonic spectrum, although not at the highest efficiency compared to the case of relativistically moving mirror [108].

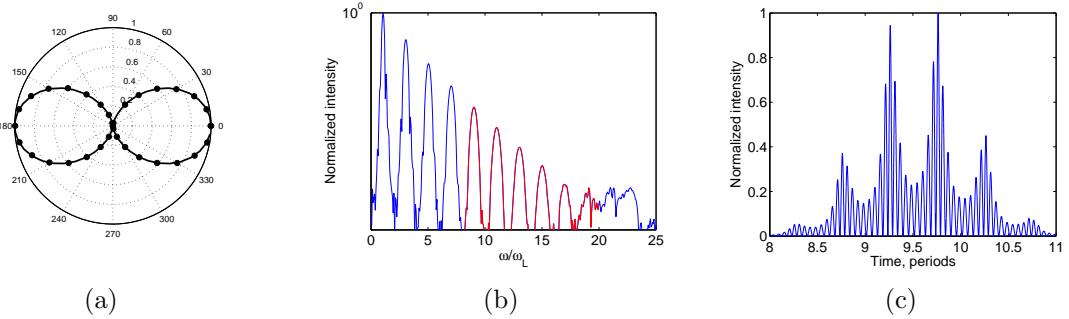


Figure 3.5: a) Angular distribution of the intensity of emitted light for the case of dipole oscillating in y direction. Dots represent the results of calculations using Lienard-Wiechert formula and the straight line is the predictions of the theory. b) Spectrum emitted by the particle moving with the trajectory same as on fig. 3.2a. c) Results of filtering (from 9th to 19th harmonics) of the light emitted by the particle.

Fig. 3.5b demonstrates the spectrum radiated by the electron moving with the same trajectory as on fig. 3.2a and exhibits only odd harmonics of fundamental frequency as the periodicity of the longitudinal oscillations is double the fundamental frequency. Detector is placed far on the left from the initial electron position. Fig. 3.5c demonstrates the results of the filtering of harmonics from 9th to 19th. A train of attosecond pulses is clearly visible.

One can put a detector also to the far right from the electron and observe approximately the same picture. This explains the harmonic emission from the rear side of the foils. In the simple model the plasma is not present and the rear side spectrum exhibits all odd harmonics from fundamental up to the highest. In reality plasma would filter out all harmonics below the plasma frequency - this is in perfect agreement with the PIC simulations.

3.2 Summary of the chapter.

In this chapter the simple one-particle model is presented. This model is very intuitive and allows to understand the basic properties of the dynamics of the reflecting surface during the interaction with intense laser pulse. A series of PIC simulations exhibit good agreement with the model calculations. It is shown that for the case of normal incidence of the laser

pulse the term *relativistic interaction* is very relative and depends on the intensity of the pulse as well as density of the target. A plasma with higher density effectively screens the incoming laser pulse. The emission of harmonic spectrum happens due to the nonlinear and periodic term and can be understood from both macroscopic and microscopic points of view.

Chapter 4

Controlling the temporal structure of harmonic beam.

The most straightforward way of generating the attosecond pulses is by slicing a part of the reflected spectrum by a bandpass filter that suppresses the fundamental and low lying harmonics. If the driving pulse is a many-cycle laser pulse (consisting of several periods of the 2.63 fs period for a commonly used Ti:sapphire laser systems), the plasma mirror executes accordingly also oscillations and the process is repetitive. This gives rise to a discrete spectrum within the filtered part, which in the time domain corresponds to a train of attosecond pulses. For many applications a single attosecond pulse is desirable [49]. The simple mirror model concept gives two possibilities for pursuing this goal. Both methods rely on reducing the number of surface oscillations during interaction. The most straightforward idea is to use laser pulses that have the duration of only few cycles (ideally only one cycle) - thus during the interaction the surface oscillates only few times and single attosecond pulse can be extracted. This method is called intensity gating and was theoretically studied, for example, in the paper by Tsakiris *et al* [106]. Let us briefly discuss this method.

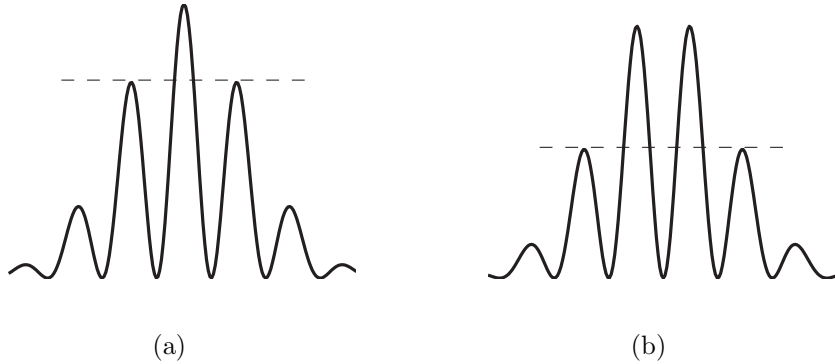


Figure 4.1: Instantaneous intensity of 2-cycle cosine (a) and sine (b) pulses.

4.1 Intensity gating

In the intensity gating technique in order to properly extract a single attosecond pulse from the harmonics generated on the surface it is important to control the carrier-envelope phase (CEP) of the incoming pulse. This becomes obvious from a schematic drawing on fig. 4.1 where the instantaneous intensity of cosine (a) and sine (b) pulses is presented. For cosine pulse it is possible to gate only one peak, whereas the sine pulse always has two peaks in intensity.

From eq. 3.9 electric field driving the surface is given by

$$E_{dr}(t) = E_{0,dr} \cdot \cos(t + \alpha + \phi_0), \quad (4.1)$$

where $E_{0,dr}$ - is the amplitude, $\alpha = \arctan(\omega_p)$ and ϕ_0 is the CE-phase. Let's fix the plasma density n to 81 times overcritical. Plasma frequency ω_p is then equal to 9 and $\alpha = 1.46 \approx \pi/2$, which means that it is not optimal to shoot cosine pulse initially, but rather a pulse with phase $\phi_0 = -\alpha$. Spectrum of the 2-cycle pulse with amplitude $a_0 = 20$, reflected from the plasma with density $n = 81$ is shown on fig. 4.2a. When initial CE-phase ϕ_0 was set to 0 corresponding to the cosine-pulse, filtering of the reflected light from 30th to 100th harmonic resulted in a train of 2 attosecond pulses (fig. 4.2b). In the optimal case when the CE-phase was set to compensate α the filtering resulted in the single attosecond

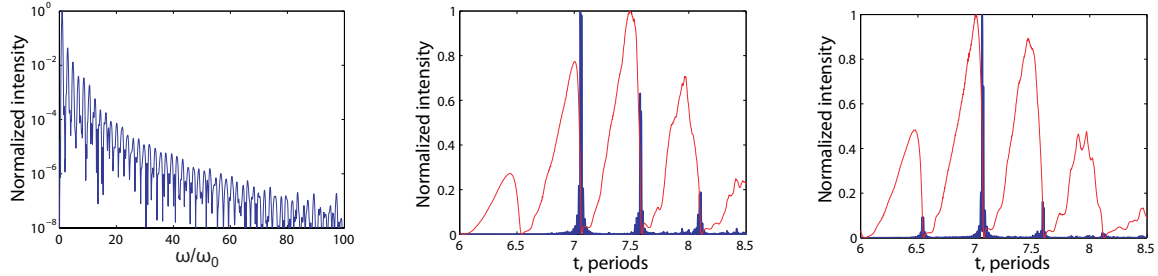


Figure 4.2: a) Spectrum of the reflected light for laser pulse with $a_0 = 20$, 2-cycle duration, density of the target is $n = 81$. b) Filtered light (from 30th to 100th harmonic) for the case when initial phase of the laser pulse was $\phi_0 = 0$. c) Same as on b) but $\phi_0 = -\alpha$.

pulse with strongly suppressed satellites as shown on fig. 4.2c. It is important to notice that α depends on the density of the target and changes from $\alpha = \pi/4$ for the target with $n = 1$ to $\alpha \rightarrow \pi/2$ for $n \rightarrow \infty$. Thus, the known dependance of the coefficient α can be used for optimization of experiments.

4.2 Polarization gating

4.2.1 Dynamics of the reflecting surface under the influence of light with different polarization.

Another approach for generation of single attosecond pulses is to use many-cycle pulses and incorporate a time varying switch or gate that allows harmonics emission only during a very short time interval. A possible switch is based on the dependence of the harmonics efficiency on the polarization state of the driving pulse. In both cases, since the driving pulse or the gate can be reduced to a 2-3 periods only, the positioning of the carrier frequency field under the envelope of the pulse and therefore the carrier-envelope phase (CEP) stabilization plays an important role.

As shown in previous section, it is possible to generate single attosecond pulses with the help of intense few-cycle laser pulses. However, the laser systems with the required specifications are still under development, and more time is needed to make them fully

operational [112]. Most of the high power (10-100 TW) laser systems currently in operation in several laboratories deliver pulses with a duration of $\tau_L \simeq 50$ fs. For these systems, the technique known for almost 10 years in connection with harmonics generation from atomic media - polarization gating [113, 114, 115] appears to be apropos. In this technique, the laser pulse is appropriately manipulated so that rapid switching between circular and linear polarizations within the same pulse occurs for a very short time interval thus creating a gate that temporally confines the harmonics generation process. The same technique is in principle applicable to harmonics from solid targets [116]. The aim of the present work is to study in detail the conditions under which the specific polarization gating technique used in gas harmonics can effectively be applied to surface harmonics. The study of the dependence of harmonics generation efficiency on the ellipticity of the laser pulse for both normal and oblique incidence allows us to estimate the parameters under which the gate would effectively confine the emission in only one attosecond pulse.

The basic idea behind the oscillating mirror model is that the electrons at the plasma vacuum interface execute forced oscillations near the edge of an immobile step-like ion background. For near-normal incidence, the oscillations are driven by the light pressure force F_p of the incident laser pulse arising from $\mathbf{v} \times \mathbf{B}$ term of the Lorenz force. In the case of linear polarization of the incident pulse, this force varies as $F_p \sim a_L^2(t) \cdot [1 + \sin(2\omega_L \cdot t)]$, where $a_L^2(t) = I_L(t) \cdot \lambda_L^2 / (1.37 \times 10^{18} \text{W} \mu\text{m}^2/\text{cm}^2)$ is the normalized vector potential envelope. Charge separation and induced electrostatic fields give rise to a restoring force and thus to surface oscillations. Due to the relativistic Doppler shift, light reflected from such an oscillating mirror consists of a broad harmonics spectrum. Moreover, the harmonics are generated only during the short time when the mirror moves towards the laser pulse, which results in their phase-locking and attosecond duration. In the case of the circularly polarized pulse the force due to light pressure is of the form $F_p \sim a_L^2(t)$ and thus it exhibits no fast oscillations. The slowly-varying laser pressure following the envelope of the laser pulse pushes the electrons against the restoring force due to charge separation creating only a dent in the electron cloud. The absence of surface oscillations means also absence of harmonics emission. These basic assumptions of the oscillating mirror model are clearly

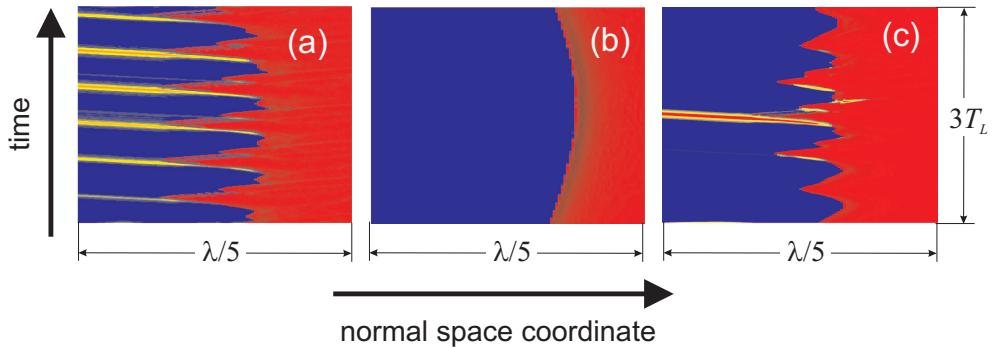


Figure 4.3: Plasma surface motion (vertical axis represents the time and horizontal axis the space coordinate both in arbitrary units) under the influence of linearly (a), circularly (b), and (c) gated pulses. In the case of linear polarization (a) surface oscillations (red color) are clearly seen. The generated train of attosecond pulses propagating with the speed of light are shown in yellow color. Circular polarization (b) exhibits no oscillations and as a consequence no harmonics are generated. In the case of a polarization gated pulse (c) the surface oscillations are highly suppressed during the time of circular polarization and only few of them survive. One clearly sees that only one attosecond pulse is generated. The simulation parameters are: $a_L = 10$ ($I_L = 100I_{rel} \approx 2.0 \cdot 10^{20} \text{ W/cm}^2$, $\lambda_L = 0.8 \mu\text{m}$), $\tau_L = 5$ cycles (15 fs), $n_e = 40n_{cr}$, normal incidence.

supported by the 1D-PIC simulations shown in fig. 4.3, where the motion of the surface under the influence of linearly and circularly polarized light has been calculated.

Now as the basic features of the plasma-vacuum interface motion and the accompanying harmonics generation have been described, the idea of polarization gating becomes straightforward. When the polarization over the pulse duration rapidly evolves from circular to linear and back to circular then the harmonics will be generated only during the linear period, and the shorter it is - the less attosecond pulses will be generated. It is even possible to gate only one attosecond pulse.

The polarization gating technique was first proposed by Corkum *et al.* [113] along with a technique of using two pulses with slightly different frequencies to generate the polarization gate. Platonenko and Strelkov [114] proposed to use only linear optics to construct a gate, and this idea was experimentally realized by Tscherbakoff *et al.* [115]. The shortest attosecond pulses from atomic medium (130 attoseconds) were produced using this technique by Sansone *et al.* [117]. The polarization gating technique was also discussed

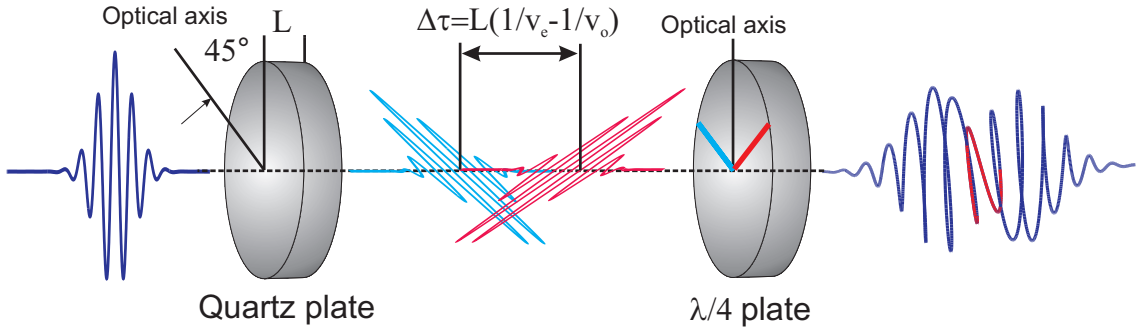


Figure 4.4: A technique for generating a pulse with time-varying ellipticity. The first crystal plate (the optical axis is set to 45 degrees with respect to the initial polarization) splits linearly polarized pulse into two delayed pulses linearly polarized in two mutually perpendicular planes. The thickness of the plate is chosen in a such a way as to dephase the two pulses proportionally to $(2n + 1) \cdot \pi/2$ (n is a natural number) so that the plate serves as the multiple order quarter wavelength plate ($\Delta t = L(1/v_e - 1/v_o)$, where L is the thickness of the plate, v_e and v_o are the velocities of extraordinary and ordinary components, respectively). The field after the first plate is linearly polarized in the beginning and in the end and has circular polarization in the middle. The second plate (the optical axis is set 45 degrees with both components) serves as a 0-order quarter wavelength plate and transforms linear polarization into circular and vice versa.

for the surface harmonics [116]. In view of forthcoming experiments, we restrict ourselves to studying the experimentally most common technique based on two crystal plates (see Figure 4.4) and we investigate the details associated with the application of this technique to the surface harmonics.

4.2.2 Dependence of harmonics generation efficiency on ellipticity

The study of the behavior of harmonics generation efficiency as a function of ellipticity ϵ of the incident pulse allows us to define the gating time. We call gating time - the time interval when the efficiency of a certain range of harmonics lies above the value of 0.1 of its maximum. The ellipticity corresponding to this harmonic efficiency is the threshold ellipticity ϵ_0 .

As it was already mentioned, the harmonics generation becomes less efficient as the

amplitude of the linearly polarized part decreases with the growth of ellipticity. In order to determine the threshold ellipticity ϵ_0 one has to calculate the harmonic efficiency (for a single harmonic or a range of harmonics) as a function of ellipticity. The efficiency within the spectral range between the n_1^{th} and n_2^{th} harmonics is given by:

$$\eta_{n1,n2} = \frac{\int_{n1}^{n2} |E_{refl}(n)|^2 dn}{\int_0^\infty |E_{refl}(n)|^2 dn} \quad (4.2)$$

where $|E_{refl}(n)|^2$ is the reflected spectrum and $\int_0^\infty |E_{refl}(n)|^2 dn$ is approximately the incident pulse energy. Figure 4.5 shows the results of the PIC simulations for the efficiency as given by Equation 4.2 as a function of ellipticity of the incident pulse in the range from 10th to 20th harmonics for $a_L = 10$ and in the range from 20th to 100th harmonics for $a_L = 20$. From Figure 4.5 one can see that the harmonics lose 90% of efficiency near the value of threshold ellipticity $\epsilon_0 = 0.4$ for $a_L = 10$ and $\epsilon_0 = 0.2$ for $a_L = 20$, respectively. We performed several PIC simulations showing that the value of ellipticity at which the harmonic efficiency is reduced by 90% slightly changes with the parameters of the laser pulse, plasma density, and the harmonics range, but we find the value of threshold ellipticity $\epsilon_0 = 0.4$ to be an adequate estimate for effective gating.

For the polarization gating scheme shown on Figure 4.4, the evolution of ellipticity with time is given by:

$$\epsilon(t) = \exp \left(-\frac{4 \ln 2 \cdot |(t - \Delta)^2 - t^2|}{\tau_L^2} \right) \quad (4.3)$$

where Δ is the delay between two mutually perpendicular field components produced by the first plate (see Figure 4.4). Given the value of the threshold ellipticity ϵ_0 , the width of the ellipticity curve (the gating time) is given by:

$$\delta_{gating} = \frac{|\ln(1 - \epsilon_0)|}{4 \ln 2} \cdot \frac{\tau_L^2}{\Delta} \quad (4.4)$$

For a threshold ellipticity value of 0.4 the formula (4.4) yields:

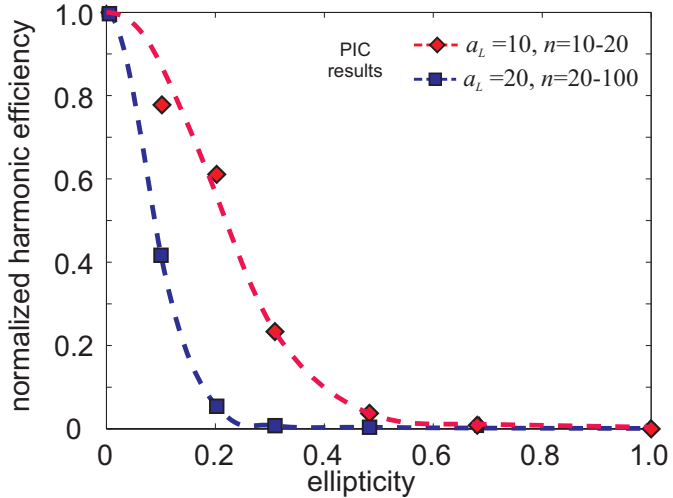


Figure 4.5: Dependence of harmonics generation efficiency on the ellipticity of the incident pulse for two cases: $a_L = 10$ ($I_L = 100I_{rel} \approx 2.0 \cdot 10^{20} \text{ W/cm}^2$, $\lambda_L = 0.8 \mu\text{m}$) (red diamonds and red dashed curve) and $a_L = 20$ ($I_L = 400I_{rel} \approx 9 \cdot 10^{20} \text{ W/cm}^2$, $\lambda_L = 0.8 \mu\text{m}$) (blue squares and blue dashed curve). The points are the results of the PIC simulations, while the curves are fits to guide the eye.

$$\delta_{gating} = \frac{0.2\tau_L^2}{\Delta} \quad (4.5)$$

In order to keep the gating time constant (5 fs) when increasing the pulse duration, one has to increase the delay produced by the first plate according to (4.5) (see Figure 4.4). Figure 4.6 also shows the amplitude of the electric field in the region of linear polarization (blue color). As one can see the delay needed for a 5 fs gating time increases with increase of laser pulse duration, and the amplitude decreases dramatically. This is also depicted in Figure 4.6 where the normalized field amplitude for the two perpendicular components is shown for three selected pulse durations. We estimate that the maximum reasonable pulse duration for polarization gating using 2 plates is about 50 fs. For longer pulses, there is at least a loss of 1 order of magnitude in the region of linear polarization and the energy waste makes this scheme inefficient. Such a limitation, however, can be overcome by using a different polarization gating scheme, for example one based on the double Michelson interferometer [118, 119].

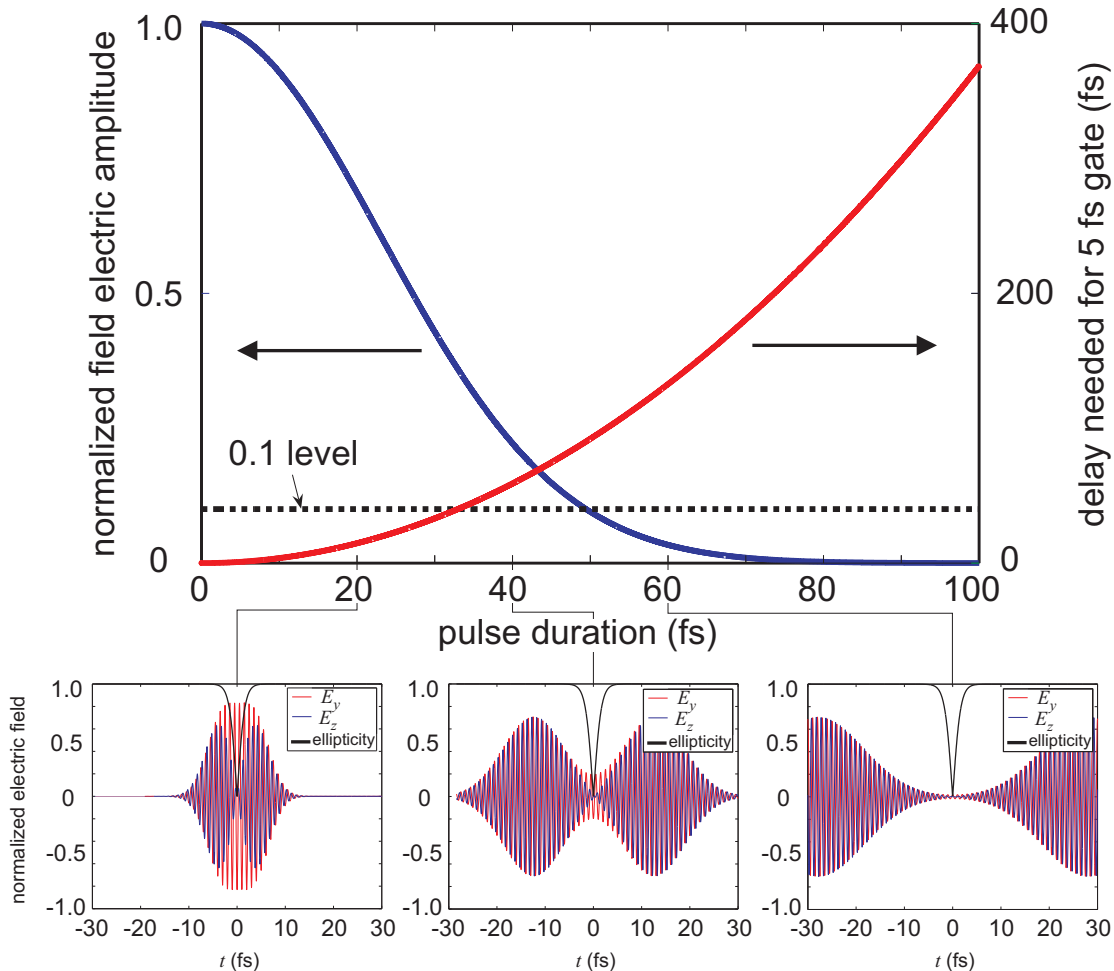


Figure 4.6: Delay needed for a 5 fs gate as a function of incident pulse duration (red curve) and the amplitude in the linear region of the pulse for this delay (blue curve). For selected pulse durations, the amplitude of the two field components are shown along with the variation of ellipticity in the lower panel. Within the polarization gate one of them is reduced to a level that renders a value for the ellipticity below the threshold.

4.2.3 Results of the simulations of the polarization gating

The results of the simulations are summarized in Figure 4.7. The initial pulse duration is 7 cycles (19 fs) and the delay (15 fs) is chosen in a way to keep the gating time approximately equal to 5 fs. One clearly sees the train of attosecond pulses generated in the case of the linearly polarized laser pulse, whereas, in the case of the pulses with polarization gating, practically all the attosecond pulses but one are suppressed and thus the polarization gating effectively works as a 2-cycle laser pulse. The surface motion in this case is shown in Figure 4.3c. The wavelet analysis [120] depicted in Figure 4.7 shows also that the use of higher-frequency filtering allows to generate single attosecond pulse with better contrast by more effectively suppressing the satellites. As it was mentioned above, the harmonics are phase-locked due to the mechanism of generation, and owing to the repetitiveness of the process they give rise to a train of attosecond pulses. When polarization gating is applied, one should be able to see its effect on the spectrum of the reflected light. If a single attosecond pulse is thus produced, the discrete spectrum should turn to continuous. But even if few attosecond pulses are captured by the gate, a broadening of the individual harmonics should be visible. Figure 4.7 depicts this difference in the spectrum for linear polarization and polarization gating. One can clearly see the broadening of the individual harmonics.

4.2.4 Dependence of harmonics generation efficiency on the angle of incidence

All the results described above are obtained for the case of normal incidence of the laser pulse. However in experiments for practical reasons, e.g., to avoid back reflection into the laser chain or to provide access to diagnostic instruments, the angle of incidence with respect to the target normal should differ from zero. The question arises whether polarization gating works as well for oblique incidence. It is well known that even circularly polarized light generates harmonics when incident obliquely [105] as there is a component of electric field parallel to the normal that drives surface oscillations. With increase of the angle of

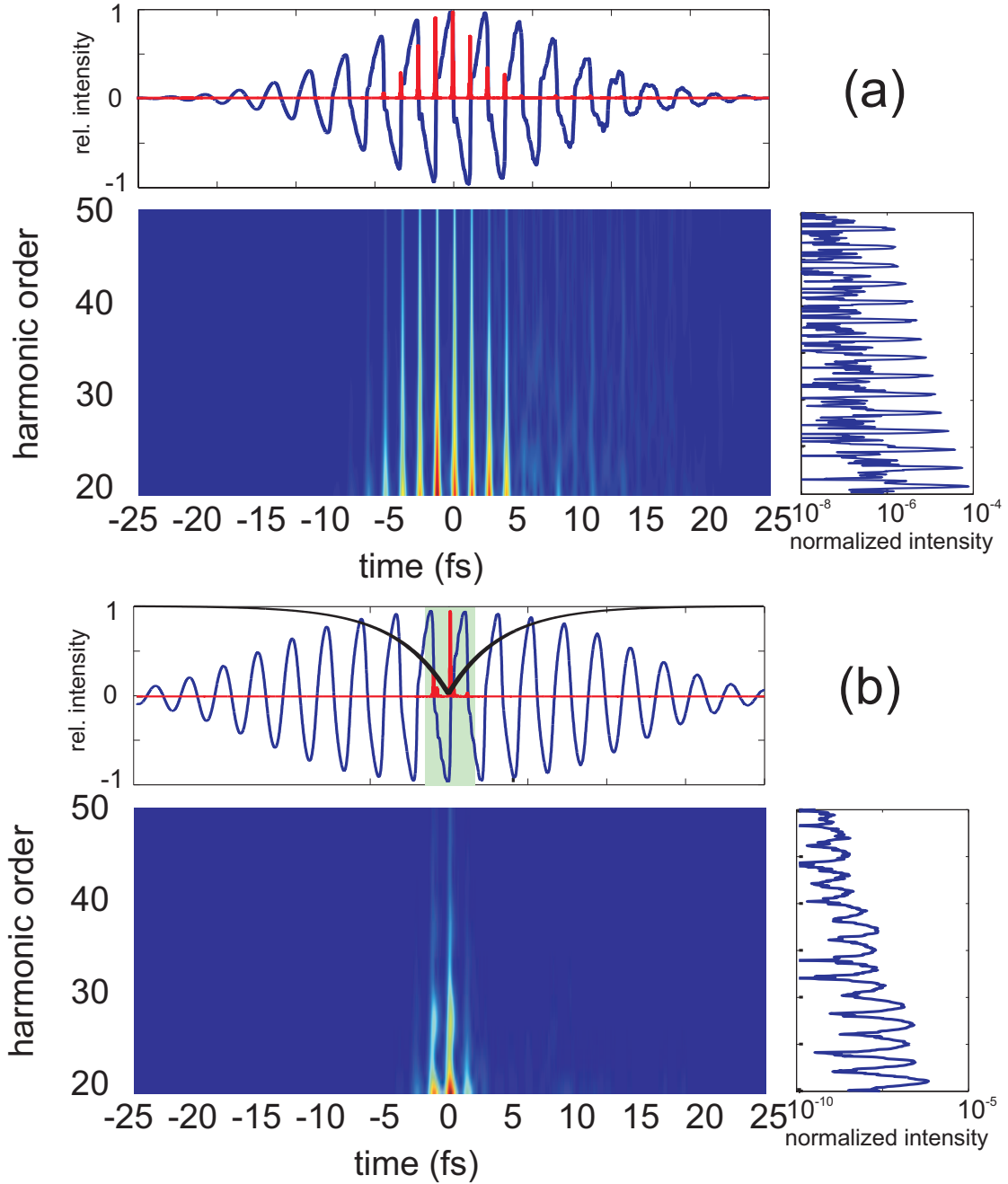


Figure 4.7: Results of particle-in-cell simulations with parameters: $a_L = 20$ ($I_L = 400I_{rel} \approx 9 \cdot 10^{20} W/cm^2$), $\tau_L = 7$ cycles (19 fs), $n_e = 80n_{cr}$ and normal incidence for linear polarization (a) and pulse with polarization gating (b). On both figures the color coded image shows the wavelet analysis (time-frequency analysis) with the vertical axis as the frequency axis and the longitudinal axis as the time axis. The graph on the right of the image represents the spectrum of the reflected light with frequencies on the vertical axis and normalized intensity on the longitudinal axis. The graph at the top shows the reflected light (blue color) and the filtered pulse (20-100 harmonics, red color). For the case of polarization gating (b) the ellipticity evolution (black color) and the gating time (green rectangle) are also shown.

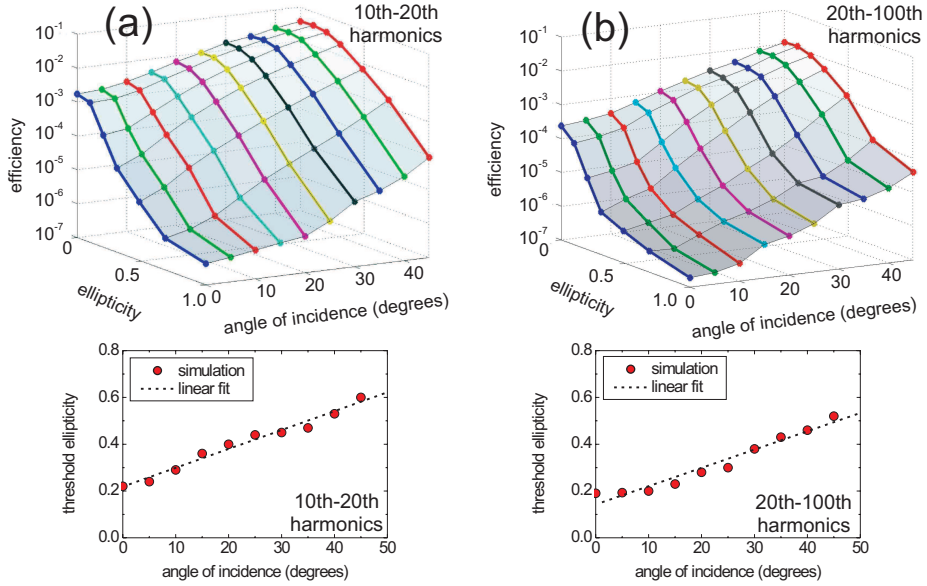


Figure 4.8: Harmonics generation efficiency as a function of both ellipticity and angle of incidence. Parameters of the simulations are the same as on Figure 4.7. The incident field for $\epsilon = 0$ is p-polarized. Results for harmonics within the range from 10th to 20th (a), and from 20th to 50th (b) are presented. For both ranges, the threshold ellipticity ϵ_0 for 10% harmonic efficiency as a function of angle of incidence is shown in the lower part.

incidence θ , this part grows proportionally to $\sin \theta$. To see the effect of oblique incidence to the effectiveness of the polarization gating scheme, we have performed a series of 1D-PIC simulations for angles of incidence between 0° and 45° . The oblique incidence case was incorporated into the 1D code using a Lorentz transformation to a moving frame in which the light is normally incident [121]. The efficiency of harmonics generation as a function of both ellipticity and angle of incidence for two harmonic ranges of practical interest is shown in Figure 4.8. Two different tendencies of the harmonic efficiency are to be noted here: first, with the increase of the angle of incidence and for all the ellipticity values it increases by more than an order of magnitude (see also Ref. [33]) and, second, for large angles of incidence it becomes less sensitive to the ellipticity. Simulations made with different parameters of laser pulse and plasma show similar results, i.e., the curve of efficiency as a function of ellipticity becomes broader with increasing angle of incidence, indicating longer gating width. This trend is depicted in the lower part of Figure 4.8, where the

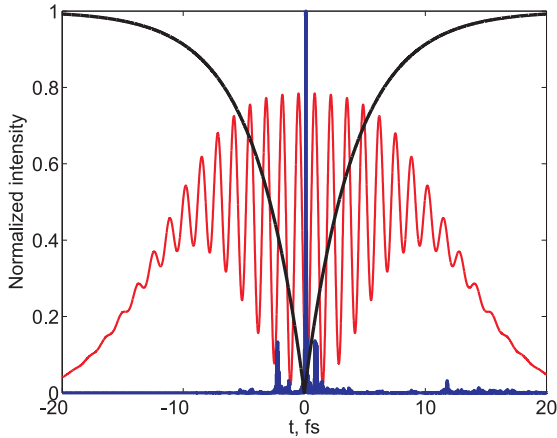


Figure 4.9: Intensity of the single attosecond pulse (blue color, 20-100 harmonics) as well as intensity of the incident pulse (red color) and ellipticity (black color) for the simulation with same parameters as in Figure 4.7 and with angle of incidence $\theta = 15^\circ$.

threshold ellipticity (the 10% level efficiency) is seen to increase as function of the incident angle approximately linearly. It appears that the greater the angle of incidence the higher the threshold ellipticity and therefore, the less confined in time the gate is. Both harmonic ranges exhibit the same general behavior, but the higher harmonic range (20th-100th) appears to be slightly more sensitive to ellipticity variation. For 45° target irradiation, the 10% efficiency level is reached for $\epsilon_0 \approx 0.6$, and this makes target irradiation under 45° questionable for experimental realization of an adequately short gate. However, it is experimentally practicable to irradiate the target under $10^\circ - 15^\circ$ in which case the results of the simulations show that the efficiency of harmonic generation decreases rapidly at small values of ellipticity, deviating only slightly from the case of normal incidence. Thus it appears quite feasible even under oblique incidence to generate a gate with duration short enough to restrict the emission to practically a single cycle. This is confirmed by the results in the Figure 4.9, where the simulations with parameters as in Figure 4.7, but with oblique incidence ($\theta = 15^\circ$), are shown.

4.3 Summary of the chapter.

In this chapter methods for controlling the temporal structure of harmonics are discussed based on reducing the number of oscillations of the reflecting surface. The first method relies on the intensity gating by few-cycle laser pulses and the second method makes use of pulses with dynamically changing polarization. The study presented in this chapter gives estimates for the gating time and thus for the parameters of the experimental set-up needed for obtaining a 5 fs gate. We find that the polarization gating by means of two plates has a limitation in the incident pulse duration due to the large delays needed, which in turn can be overcome by a different scheme (for example using the double Michelson interferometer technique [118]). It is shown that polarization gating is also feasible for oblique incidence of the laser pulse, at least for angles of incidence $\theta < 15^\circ$, which makes this scheme a candidate for experimental generation of intense single attosecond pulses using multi-cycle laser pulses.

In comparison with the gas harmonics, it appears that the method is more suitable for the case of surface harmonics since the shortcoming encountered with gas harmonics where the circular part induces unwanted ionization does not play a role in this case. In addition, the surface oscillations in the case $\theta > 0$ are driven not only by the light pressure force that oscillates at $2\omega_L$, but also by the normal to the surface component of the electric field that oscillates at ω_L . Subsequently as the angle of incidence increases, a regime is reached where all harmonics (odd and even) are efficiently generated and the attosecond pulses in the resulting train appear on every cycle and not every half-cycle as in the case of gas harmonic (odd orders only). This is a factor that should be taken into account in determining the optimum angle of incidence since it has the advantage that twice as long gates can be used to isolate a single attosecond pulse.

Chapter 5

Controlling the spatial structure of harmonic beam.

In previous chapter methods of controlling the temporal structure of harmonic beam were presented. Besides the temporal coherence the spatial coherence is of great importance especially in the view of the possibility of generation of electric fields with extreme intensities by focussing the harmonic beam to the diffraction limit. Reaching the so-called Schwinger intensity of 10^{29}W cm^{-2} [50] would help to open the whole new field of nonlinear quantum electrodynamics, where the vacuum can not be considered empty and interacts with the laser light [122, 123, 124, 125]. The Schwinger limit seems hard to reach with conventional laser systems with the wavelength of about $1\mu\text{m}$. High-order harmonics are a good candidate in that direction as besides the short duration they have also short wavelength and can in theory be focused [53]. From the experimental point of view some questions immediately arise. What is the divergence of the beam, how can it be controlled and how is it affected by the impurities of the target? In this chapter we make an attempt to answer these questions.

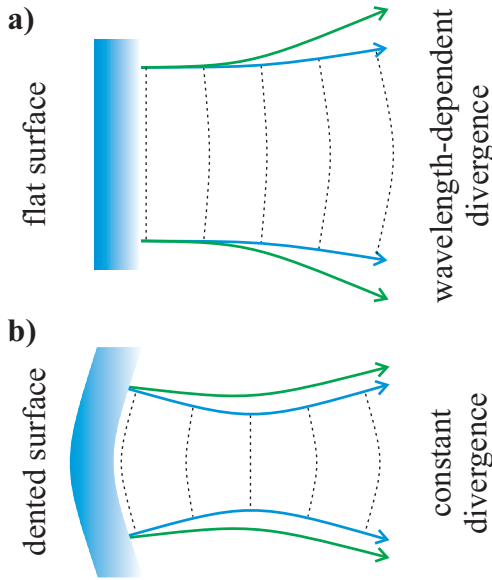


Figure 5.1: Illustration of target denting influence on the harmonic beam divergence. a) Divergence in the case of the planar target - the divergence of each harmonic depends on its wavelength. b) Divergence in the case of dented target - the beam is focused before diverging with the constant angle. (Figure courtesy R. Hörlein)

5.1 Surface denting

In the one-dimensional description of the generation process we always assume that the target is planar. If the harmonics are generated on a planar surface then the divergence angle Θ_q of the q -th harmonic is given by the approximate expression

$$\Theta_q \propto \frac{\lambda_q}{D_q}, \quad (5.1)$$

where λ_q and D_q are the wavelength and the source size of the q -th harmonic respectively. This scaling says that if all the harmonics are generated within the same spot, which has approximately the size of the laser spot, then the divergence is different depending on the harmonic wavelength. However, the experiments [28] show different scaling, namely all harmonics (within the measurement, harmonics from 20 to 40) have the same angle of divergence. This contradiction can not be resolved by assuming that the harmonics were generated each with the different initial spot size and another explanation is needed. As it

was mentioned above, expression 5.1 only works in the case of planar target geometry. In fact, initial planar target geometry changes during the interaction with the intense laser pulse due to the denting created by the inhomogeneous transverse distribution of the laser beam. This leads to the generation of the harmonics with curved wavefronts which can explain the experimental findings. The effect of the surface curvature on the divergence angle of the harmonic beam is schematically outlined in fig. 5.2. In the planar target geometry the beam diverges from the target and the divergence angle of each harmonic is governed by eq. 5.1. In the case of the dented or pre-curved target the harmonic beam first goes through the focus (generating fields that can have intensities higher than the intensity of the incoming laser beam) and then diverges, while the divergence of each harmonic now stays constant.

Two different denting mechanisms can be separated:

- Adiabatic or hydrodynamic denting of the background ions by the slow varying pressure of the laser pulse. This is closely connected to the ion acceleration mechanisms and is correlated with results of the chapter following further.
- Non-adiabatic denting of the oscillating reflecting surface due to the rapid electron motion. This can be understood from figure 3.3, where the dependence of the oscillation amplitude is plotted as a function of laser amplitude a_0 . Inhomogeneous transverse distribution of the laser beam leads to the inhomogeneous oscillation amplitudes of the mirror surface along the spot size.

The predominance of each mechanism depends strongly on the laser pulse duration. As ions are heavy compared to the electrons, the first mechanism is dominant for long laser pulses (approximately more than 15 cycles), as the second mechanism is dominant for few-cycle laser pulses.

Let us discuss the main results of the experiment presented in [28]. First of all, diffraction limited performance of 20-th harmonic was observed. Second, the divergence angle of all harmonics from 20 to 40 is constant. The laser pulse duration for the results of the paper [28] was 500 fs (for the VULCAN laser, approximately 180 periods) and 40 fs (for the

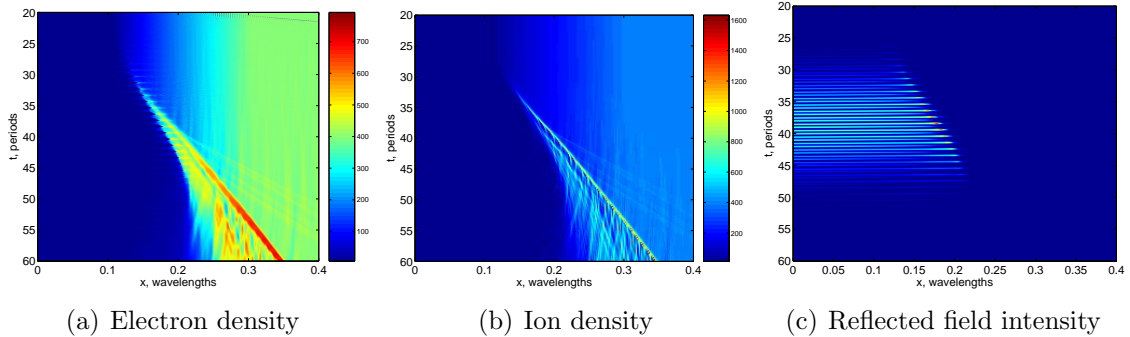


Figure 5.2: Spatio-temporal distributions of electron (a) and ion (b) densities as well as reflected field intensity (c) during the interaction with the laser pulse with $a_0 = 7, 15$ cycles FWHM duration. Plasma density is $400n_{cr}$, linear preplasma with length $0.2\lambda_L$ is assumed to be present.

ASTRA laser, approximately 45 periods) thus the hydrodynamic denting is dominant. All other laser and plasma parameters in the simulations were kept the same as in experiment. An illustration of the hydrodynamic dent is shown on fig. 5.2 where the results of the one-dimensional simulation are presented. In this simulation it was assumed that plasma has expanded during the interaction with the prepulse and the length of the preplasma is $0.2\lambda_L$ (this is justified by the fact that in experiments the laser pulse always has the pedestal due to Amplified Spontaneous Emission or some satellites). Each subfigure demonstrates the spatio-temporal picture with horizontal axis being the longitudinal coordinate x axis and vertical axis being the time axis. Electron density, ion density and the reflected light intensity are shown on fig. 5.2a,b,c respectively. One can see that the reflecting surface moved from its initial position and this motion is due to the slow laser pressure assisted movement of the ions.

From the experimental measurement of the divergence angle of the harmonic beam and knowing the spot size of the laser one can approximately estimate the size of the dent needed for the constant divergence [28]. This can be in turn compared with PIC simulations presented here. We have performed the same simulation as presented on fig. 5.2 but varying the laser amplitude and preplasma length for both ASTRA and VULCAN lasers. The results of this study are shown on fig. 5.3, which shows the depth of the dent for a range

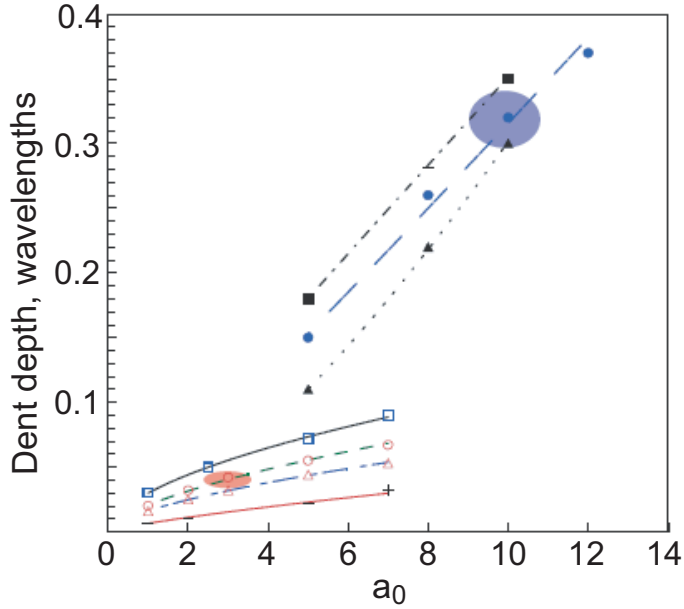


Figure 5.3: Expected level of denting from PIC code simulations for conditions similar to those used in experiments. The target densities used are $400n_{cr}$ for Astra parameters (15 cycles FWHM duration, open symbols) and $200n_{cr}$ for Vulcan parameters (180 cycles FWHM duration, filled symbols). Calculations are carried out for a spread of density ramps, resulting in two distinct groups of curves. The density ramps are 0nm (crosses), 50nm (triangles), 100nm (circles) and 200nm (squares). The expected level of denting derived from the experiment is shown by the shaded areas (red-Astra, blue-Vulcan), the extent of which indicate the level of experimental uncertainty.

of density gradients as a function of laser amplitude a_0 . The shaded areas on the figure represent the results of the estimations derived from the experimental data. To within the uncertainties of the experiment, the denting depth derived from the PIC simulations is in good agreement with the depth derived from the observations.

The effects of hydrodynamic denting can be mitigated to some extent by using few-cycle pulses. In this case the ions can be considered immobile and the non-adiabatic denting is important. To investigate the effects of the non-adiabatic denting and ways of controlling the divergence of the harmonic beam we have performed a series of 2D PIC simulations. The typical plasma density is $n_e = 30$, the target thickness is $1\lambda_L$. If not stated different, the laser pulse amplitude is equal to $a_0 = 10$, the pulses have the electric field with a Gaussian envelope function in both space and time:

$$E_y(t, x, y) = E_0 \cdot \exp \left[-\frac{y^2}{\rho^2} \right] \cdot \exp \left[-\frac{(t - x)^2}{2T_0^2} \right],$$

where ρ and T_0 are the width of the focus and duration of the laser pulse respectively. The FWHM duration is related to T_0 by $T_{FWHM} = T_0\sqrt{8\ln 2}$ and ρ is chosen to be $\rho = 5\lambda_L$. The size of the simulation box is $3.5\lambda_L$ in propagation direction and $40\lambda_L$ in polarization direction. The time step is $T_L/300$. Each cell is initially occupied by 50 macroparticles. This setup is used for all 2D simulations presented in this thesis.

We start with the simplest case - irradiation of the planar target with a laser pulse with gaussian distribution in both time and lateral direction. The farfield propagation using the standard Kirchhoff diffraction theory [102] is applied to the simulation data. This follows the approach of previous studies by Geissler *et al.* [126]. Figure 5.4a shows the electron density distribution approximately in the moment when the laser pulse maximum reaches the target. One can see how the inhomogeneous lateral distribution of laser pulse results in a dent, that produces the harmonics with curved wavefronts, that are shown on fig. 5.5a. The results of the propagation of the harmonic beam away from the target is shown on fig. 5.4b for different distances. On this figure the transverse beam profile (harmonics from 25 to 100) is shown. One can see that the harmonic beam goes through the intermediate focus before diverging again, reaching the intensity in the focus of approximately $10^{21} W/cm^2$.

5.2 Focusing of harmonics

Dent-induced focusing has a major problem - the beam is badly focused and is not controlled. In order to control the focusing one can use pre-dented targets. We have also performed the simulation with the parabolically shaped concave target. The radiation reflected from the target was again spectrally filtered from 25th to 100th harmonic and propagated to the focus. The comparison of the transverse beam profile for planar target case and the concave case is presented on fig. 5.5c. The inlay on this figure demonstrates

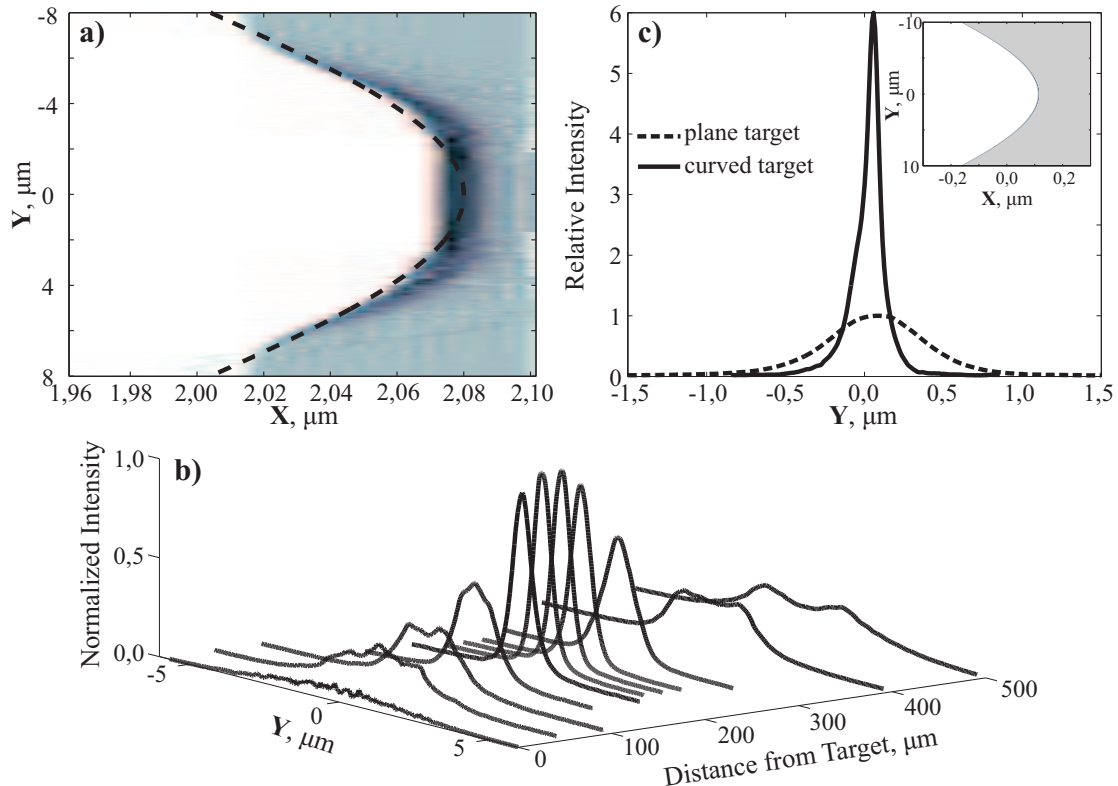


Figure 5.4: Simulations of harmonic focusing as a result of target denting. a) Snapshot of the target density of an initially planar target approximately in the instance when the peak of the driving laser reaches the target. The dashed line indicates the dent. Propagating the harmonics generated on the target away from the target (see b) clearly shows focusing of the emitted radiation. c) Comparison of the radial intensity distribution from a planar and a concave target. Significant enhancement of the focused intensity can be achieved in the case of a parabolically shaped target. The initial target shape is shown in the inlay in c. (Figure compiled by R. Hörlein)

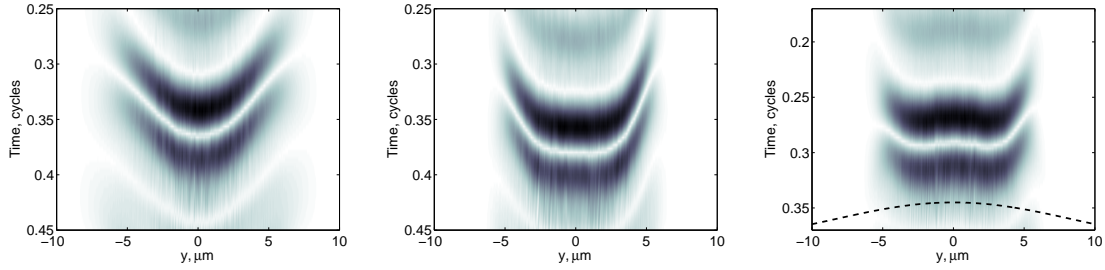


Figure 5.5: Simulated wave-fronts of the harmonics pulse (consisting of harmonics 25 to 100) immediately after the generation on the target for a) Gaussian intensity distribution on a planar target, b) super-Gaussian on a planar target and c) Gaussian on a pre-formed convex surface. In addition the dashed line in c) outlines the shape of the curved surface used in this simulation.

the target used in the simulation. In the case of the shaped target the width of the harmonic beam is approximately 6 times smaller compared to the case of the planar target, leading to the increase of intensity by the factor of 36 assuming radial symmetry. The intensity in the focus is then approximately $5 \cdot 10^{22} \text{ W/cm}^2$ and is larger than the intensity of the incident light. Due to the limited resolution of the simulation only harmonics up to 100 are taken into consideration. In theory selecting higher harmonics and focusing them with appropriately shaped targets could lead to achieving intensities on the order of 10^{29} W/cm^2 .

5.3 Controlling the divergence of the harmonic beam by shaped targets.

The problem of both dent-induced and concave-target focusing is that the focus is situated in the close vicinity of the target, where a lot of charged plasma particles are located. If one wants, for example, to detect electron-positron pairs created by the strongly focused harmonic beam, then this situation is not favorable. More than that, for many experiments it is important to transport the harmonic beam to the sample, which is usually mounted far from the target. This poses another question - can the harmonic beam be generated with flat wave fronts to diminish the divergence?

The easiest solution is to use the laser pulses that have flat transverse shape. To show the effect of using this idea we have performed a simulation with a superGaussian (of the order 4) laser pulse. The results are presented on fig. 5.5b. Compared to the case of a Gaussian pulse (fig. 5.5a) they exhibit significantly flatter wavefronts. In experiments, however, the generation of the flat-top pulses is accompanied with technical difficulties and waste of laser energy.

Another approach can be applied - using the shaped targets. In this case one needs to use convex targets instead of concave discussed in the previous chapter. Approximately knowing the depth of the dent for given intensity (for example from PIC simulations) one can engineer a target that will compensate the dent. For the case presented on fig. 5.4a, a spherical target with a diameter of approximately $500\lambda_L$ will be appropriate. Figure 5.5c shows the effect of such a target on the harmonic beam - straightening of the wavefronts. The deviation on the wings can be overcome by using even more complex targets. The drawback of this method is that it is essentially single-shot. After every shot in experiment the target has to be aligned again. Which of methods is preferable depends on the available laser energy and the goals of the experiment.

5.4 Influence of surface roughness on the divergence of harmonic beam.

On limit to the ultimate potential of beams of harmonics generated on the surface of the overdense plasmas is the role of any surface imperfections such in terms of shape and roughness. These can greatly affect the generation process and the angular and temporal structure of the beam. This is particularly important for Coherent Harmonic Focusing suggested in [53].

Classical scattering problems [127] such as, for example, propagation of radio waves near the surface of the ocean imply that the roughness is quasi-stable in time and the Rayleigh criterion can be used - the surface is considered rough and leads to diffuse reflection if

its characteristic roughness size $h > \lambda_L/(8 \cos \theta_i)$ (in other words the maximum phase difference between two reflected rays is more than $\pi/2$), where λ_L - is the wavelength of the incident wave and θ_i is the angle of incidence [127].

Contrary to the Rayleigh criterion, Dromey *et al.* experimentally observed a striking behaviour - "the harmonics are insensitive to surface roughness on the scale of the harmonic wavelength" [28].

Motivated by this surprising behaviour, we have investigated the interaction of a relativistically strong laser pulse with an overdense corrugated plasma surface. Here we present time the theoretical basis, both analytically and with PIC simulations, for rapid, non-adiabatic smoothing of the plasma-vacuum interface and show it to be effective on length scales below the transverse electron oscillation amplitude.

In section 3.1.1 the simple one particle model was introduced. In eq. 3.15 the approximate expression for transverse oscillation amplitude of the electron layer was given. One can write it in the following form

$$Y \approx \frac{2 \cdot a_0}{\omega_p}. \quad (5.2)$$

As it was discussed in section 3.1.1, the simple estimate (5.2) works well until the value of approximately $a_0 \approx \omega_p/2$. After that relativistic corrections to the skin depth and electron longitudinal motion become important [128]. On the other hand the simplicity of this expression makes it convenient for the following estimates. The results for the higher laser amplitudes can be obtained by numerically integrating the model equations. From fig. 3.2 one can see that the transverse motion amplitude reaches considerable fraction of the laser wavelength and might be responsible for the smoothing of the surface. Indeed if the transverse motion of the electron exceeds the characteristic roughness size, then the roughness is likely to disappear.

Having estimated the amplitude of the transverse coordinate Y one can establish a criterion for surface smoothing to occur based on the ratio of this amplitude to the characteristic roughness size h . For instances where the transverse motion substantially exceeds

the characteristic roughness within the whole roughness area, substantial smoothing can be expected. For simplicity we consider that the roughness has the same characteristic length h in both lateral and normal directions. One can define a dimensionless parameter ξ separating the case when smoothing takes place from the case when the roughness survives during the interaction:

$$\xi = \frac{2a_0}{\omega_p h} \cdot e^{-\omega_p h}. \quad (5.3)$$

When $\xi > 1$ the roughness according to our criterion vanishes.

In order to demonstrate the surface smoothing we have conducted a series of 1D and 2D PIC simulations using the code PICWIG described in chapter 2, with clean and rough surfaces for different laser amplitudes a_0 . Step-like vacuum-plasma interface is assumed, the ions are immobile. The surface is modulated under sinusoidal law in order to simulate the roughness (see left part of Fig. 5.7). For convenience, the modulation period and amplitude are linked and the position of the vacuum-plasma interface is given by the law $x = h \cdot \sin(\frac{y}{h})$.

In the 2D case in order to investigate the spatial properties of harmonics we analyze the propagation of the harmonics emission away from the target using Kirchhoff diffraction theory [102] following the approach used in earlier investigations of harmonics propagation [126]. The harmonic beam (from 15th to 25th harmonic, central wavelength $0.05\lambda_L$) $200\lambda_L$ away from the target is shown on Fig. 5.6. On all four sub-figures the color surface presents the distribution of normalized intensity of the filtered harmonics as a function of both time t and transverse coordinate y (the ceiling panel shows the same data as a color-coded image), the upper-right plane shows the projection of the beam to the time axis thus the time structure of the harmonics beam exhibiting a train of several attosecond pulses. On the upper-left plane the intensity distribution of the harmonics beam as a function of transverse coordinate y is shown (black solid line). Results presented on Fig. 5.6 a,b,c,d are obtained for surface with modulation size $h = 0$ (clean surface, $\xi \rightarrow \infty$), $h = 0.05\lambda_L$ ($\xi = 2$), $h = 0.1\lambda_L$ ($\xi = 0.2$) and $h = 0.2\lambda_L$ ($\xi = 0.003$) respectively. There are several important points to mention.

First, for these simulation parameters the distance of $200\lambda_L$ corresponds to the position of the harmonics focus due to surface denting as discussed in the previous sections. This can be illustrated from the Fig. 5.6a by the fact that the transverse width of the reflected harmonics beam (see graph in the upper-left plane) is much less than the initial laser width with $\rho = 5\lambda_L$.

Secondly depending on the dimensionless smoothing parameter the spatial and temporal structure of the harmonic beam is not influenced by the surface roughness. Figure 4 shows the harmonic orders from the 15th to the 25th, which should undergo diffuse reflection according to the Rayleigh criterion by all the rough surfaces simulated. Contrary to the Rayleigh criterion, but in agreement with experimental observation [28], almost no change in the harmonic beam structure is observed for $\xi = 2$ (Fig. 5.6b) in good agreement with our smoothing criterion. Surfaces with $\xi < 1$ (Fig. 5.6c,d) lead to the speckle-like diffraction picture with more energy going to the wings of the beam. The fact that the beam is still tolerably collimated hints that even though $\xi < 1$, the characteristic surface roughness was significantly diminished during the interaction. The analysis of the spatial structure of harmonics generated on the corrugated surfaces exhibits collimated beam structure and serves as an indirect proof of the surface smoothing.

Direct proof of the surface smoothing can be found on Fig. 5.7 where initial density distribution (as function of longitudinal and transverse coordinates) and the density distribution near the moment when the pulse maximum reaches the surface are shown (left and right sub-figures respectively). The results here are presented for the surface with $\xi = 2$ and show that the transverse motion of the electrons leads to the non-adiabatic (in contrast to the adiabatically slow smoothing due to ion motion) smoothing of the corrugation.

5.5 Summary of the chapter.

In this chapter some important for experiments questions are discussed, that concern the spatial coherence of the harmonic beam. It is shown that the laser pulse with inhomogeneous lateral distribution of intensity produces concave structure on the target that leads

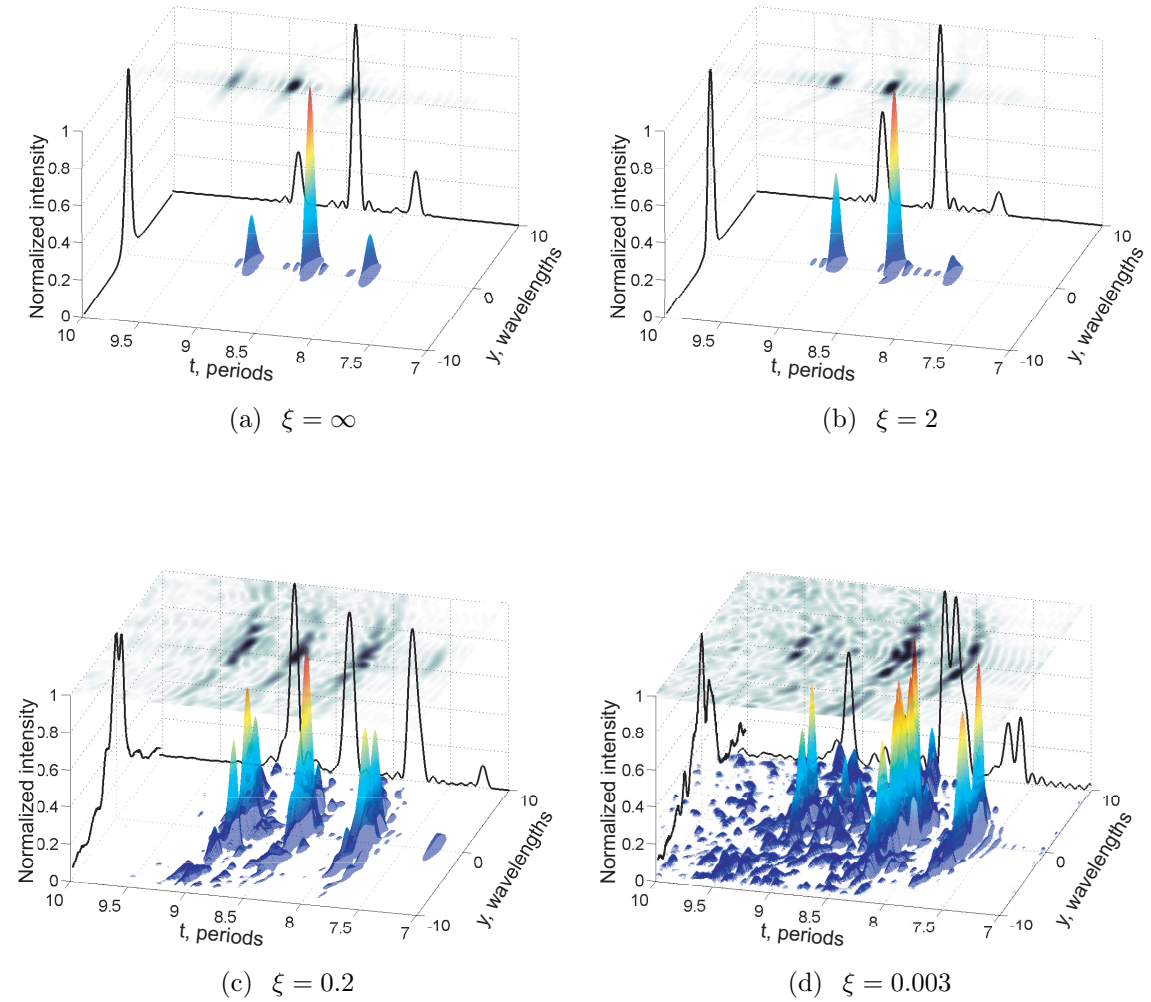


Figure 5.6: Farfield distribution of the reflected harmonics beam $200\lambda_L$ away from the target for a) clean surface, b) surface with modulation size $h = 0.05\lambda_L$, c) surface with modulation size $h = 0.1\lambda_L$, d) surface with modulation size $h = 0.2\lambda_L$.

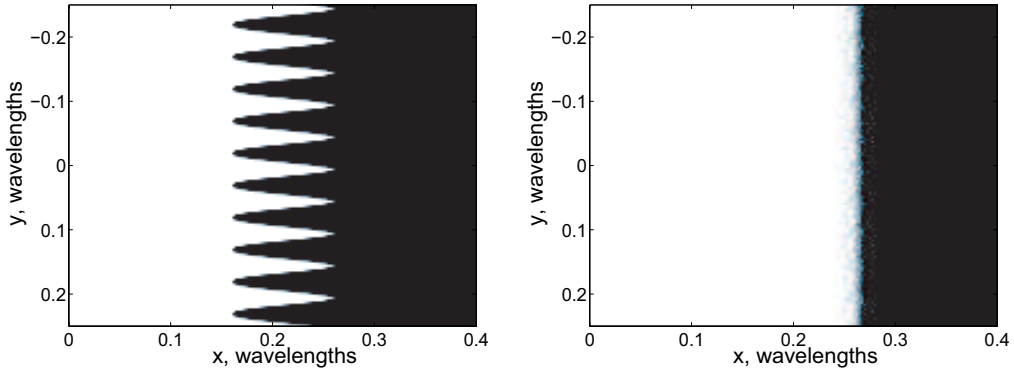


Figure 5.7: Initial density profile (left) and the smoothed density profile in the middle of the interaction process (right) for the surface with $\xi = 2$.

to the *parasitic* (in other words uncontrolled) focusing. Denting can happen due to two reasons: 1) the slow laser-pressure induced ion motion and 2) the fast Lorenz-force driven electron motion. The beam reflected from such a dented target exhibits constant divergence for all harmonics far from the target.

There are several ways of controlling the divergence of the harmonic beam. If one is interested in highest fields, one can use the concave targets and control the focusing of harmonics. This has a problem, because the focus is located about $50\lambda_L$ from the target, where there are a lot of background charged particles and photons. In experiments that would lead to difficulties in separating the useful signal from the noise.

If one is interested in re-focussing or transporting the beam with minimum divergence, one can pursue the attempt to straighten the wavefronts of the harmonic beam by reducing the dent. Here, one can use either shaped laser pulses with flat-top intensity distribution, or shaped convex targets. The first method has the disadvantage, because obtaining the flat-top distribution in experiment is fairly difficult. The second method is essentially single-shot, because the alignment of the target is needed before every shot. The usage of any of this methods relies on the available laser systems and the goals of the experiment.

Surface roughness can greatly affect the process. In this chapter we have shown that surface smoothing of a rough target surface during the interaction of relativistically intense laser pulse can be sufficient to allow diffraction limited beaming of harmonic radiation -

contrary to expectation based on the Rayleigh criterion. This effect does not rely on the slow, adiabatic smoothing due to ion motion and is a direct result of the large spatial amplitude of the electron trajectories in relativistic laser interactions. This finding has direct impact on the peak intensities that can be achieved at shortest wavelengths and suggests that extremely high quality keV harmonic beams are achievable.

This chapter might be useful for optimization of future experiments as it offers the ways of controlling the spatial structure of the beam of harmonics generated on the plasma-vacuum interface.

Chapter 6

Generation of monoenergetic ion beams from thin foils irradiated by circularly polarized laser pulses.

6.1 Ion acceleration in the radiation pressure regime

A prominent feature of relativistic laser-matter interaction is that the electrons do not only oscillate in the transverse electric field, but are also pushed longitudinally by the $\mathbf{v} \times \mathbf{B}$ part of the Lorentz force. Thus, focussing an intense laser pulse onto a solid target results in charge separation fields at the front side of the target. Those fields in turn accelerate ions into the laser propagation direction. For linearly polarized laser pulses this front-side acceleration process was studied both theoretically [129, 57, 60] and experimentally [78, 79, 64] during the last years. The role of circularly polarized light in high-intensity laser-solid interactions was addressed in recent publications by Macchi *et al.* [84] and Liseikina *et al.* [83]. In the case of circular polarization, the force due to the light pressure, i.e. the $\mathbf{v} \times \mathbf{B}$ term in the Lorentz-force, has no oscillating term and thus leads to less heating of electrons than linear polarization. While electrons are adiabatically pushed into the target, ions can be effectively accelerated in the non-oscillating charge separation field.

The difference between circular and linear polarization can be traced from animations made from simulation data. We use the 1D3P PIC code described in chapter 2 (the simulations and parameters are described below in section 4), where 1D3P means that each quantity depends only on one spatial coordinate (in our case the x - direction in which the laser propagates), but particles have all three momentum components and generate currents in three dimensions. In order to visualize particle motion in three-dimensional space in figure 6.1, we have selected electrons (blue) and ions (red) along the $y = z = 0$ axis, obtain their trajectories by integrating their momenta, and plot them in full three-dimensional space.

Figure 6.1 displays a snapshot taken at the time when the pulse maximum reaches the target. Black arrows represent the electromagnetic fields for a circularly polarized laser beam incident from the left side. The target foil is initially located at $x = 20\mu\text{m}$, and its thickness is $0.01\ \mu\text{m}$. Figure 6.1b represents the ion phase-space (longitudinal momentum versus ion position). Figures 6.1c and 6.1d give the electron and ion energy spectra, respectively. Figure 6.1e shows the square root of intensity (later by this term we mean the instantaneous intensity) of the laser pulse (black), the longitudinal field (green) and electron and ion densities (blue and red, respectively).

In the case of circular polarization (movie1 [130] and figure 6.1), the longitudinal charge-separation field, that accelerates the ions, is non-oscillating and produces a mono-energetic ion bunch. Electrons are moving in circular orbits and the electron spectrum also exhibits mono-energetic features during the interaction time. After the laser pulse, electron energy decreases because of energy transfer to the remaining foil. It is interesting to notice that in this particular case the longitudinal electric field amplitude becomes as large as that of the incoming laser pulse (see next section).

The case of linear polarization (movie2 [131] and figure 6.2) is quite different. In sharp contrast to the case of circular polarization, the oscillating component of the laser $\mathbf{v} \times \mathbf{B}$ force drives the electrons into chaotic longitudinal motion back and forth through the thin target foil. This strongly heats the electrons and leads to foil explosion rather than smooth localized ion acceleration. Notice the wide spatial spreading of the longitudinal

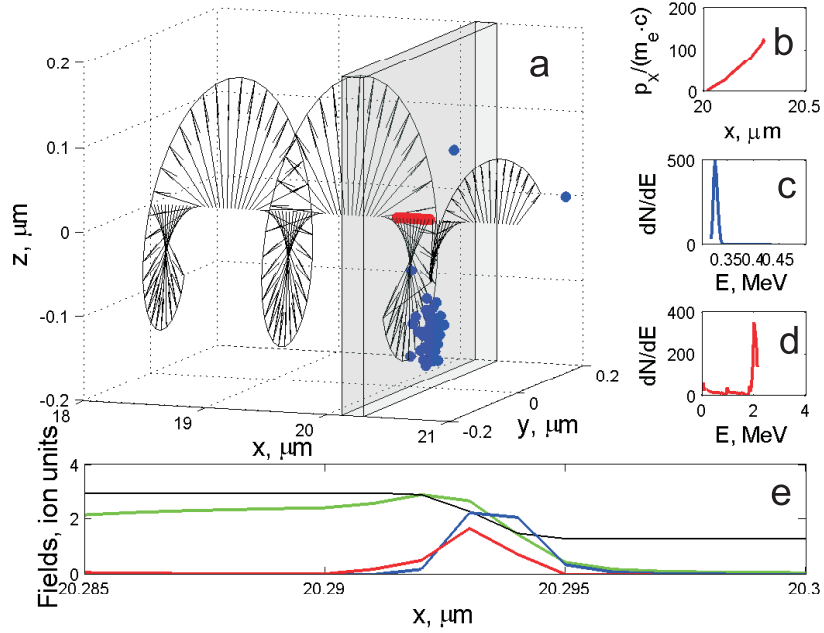


Figure 6.1: Snapshot of laser-foil interaction taken at the time when the pulse maximum reaches the target. The circular polarized laser pulse is incident from the left. The simulation parameters are: laser amplitude $a_0 = 3$, laser FWHM duration is 15 cycles, target density $n_e = 100n_{cr}$, and target thickness $l = 0.01\lambda_L$. (a) Positions of electrons (blue circles) and ions (red circles) are plotted on three axes in microns as well as electric field (black arrows) in arbitrary units. The transparent box indicates target position. (b) Ion Longitudinal ion phase space, (c) electron and (d) ion energy spectra, (e) square root of laser intensity (black), longitudinal field (green), and normalized electron (blue) and ion (red) density.

electric field (green), which accelerates the ions. As a result, we observe broad distributions of electrons (blue) and ions (red) with thermal-like spectra and strongly reduced energy transfer to ions. This confirms the results of recent publications [81, 82, 132, 133] that the use of ultra-thin foils combined with circular polarization of the laser pulse allows for highly efficient generation of mono-energetic ion beam bunches.

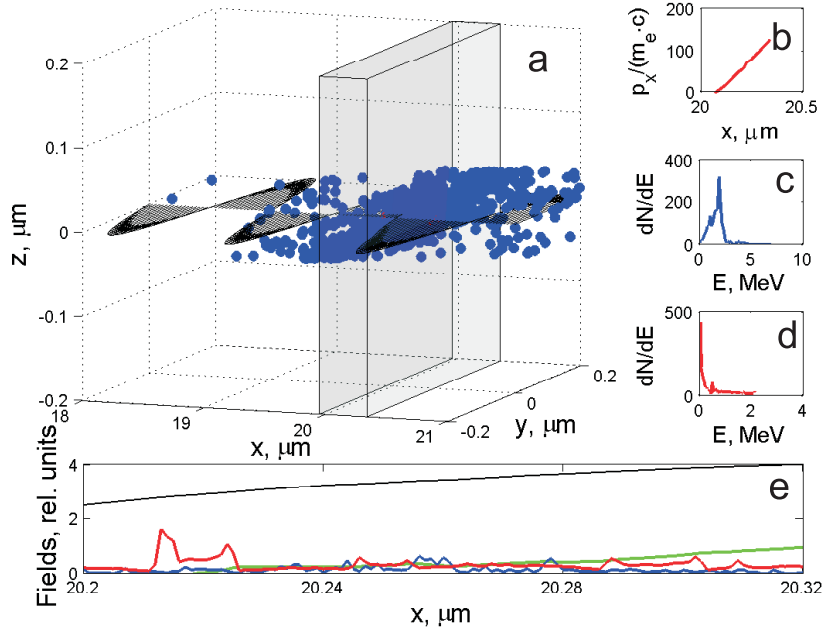


Figure 6.2: Same as figure 6.1, but for a linear polarized laser pulse with amplitude $a_0 = 3 \cdot \sqrt{2}$ incident from the left.

6.2 Model equations

For the following considerations we assume a steady state of the interaction where the electrostatic pressure is balanced by the radiation pressure of the laser (see also movie1). The model was already described above in chapter 2. Here we discuss it again. The charge separation field produced by displacing the electron slab with thickness l into the target is given by

$$a_{es} = Znl, \quad (6.1)$$

where a_{es} is the electrostatic charge separation field, Z and n are the mean charge state and the density of the target ions, respectively, and l is the thickness of the electron depletion layer [81]. We work in *relativistic units* (see Chapter 2). The length of the depletion layer

can be found from the balance between electrostatic and radiation pressure, i.e.

$$\frac{1}{2}a_{es}^2 = (1 + R - T)a_0^2, \quad (6.2)$$

where R and T are reflectivity and transmission of the foil, respectively. By combining eqns. (6.1) and (6.2) and considering a target of thickness d we introduce the dimensionless parameter

$$\xi = \frac{Znd}{a_0 \cdot \sqrt{2(1 + R - T)}}. \quad (6.3)$$

The dimensionless parameter ξ defines the regime of interaction. When $\xi = 1$, then the laser pressure is just sufficient to displace all electrons by the target thickness, i.e., the target thickness equals the length of the depletion layer. For $\xi \leq 1$, the laser pressure is stronger than the electrostatic pressure, and the electrons are pushed out of the target foil, while for $\xi > 1$ compressed electrons and space charge field remain inside the foil, accelerating the ions layer by layer [81]. For the latter case, the whole foil is set into motion after the shock launched by the laser front reaches the rear side of the target. In the following we divide our analysis into two different scenarios: i) the electrons are completely separated from the foil ($\xi \leq 1$) and ii) the electrons remain bound to the target ions ($\xi > 1$).

i) When the electrons are separated from the foil, the maximum field at the rear side of the target is defined by eq. (6.1), where l must be replaced by the target thickness d . In our one-dimensional consideration, this field is maintained for the duration of the laser pulse t_L , which in the non-relativistic description yields the maximum ion kinetic energy of

$$E_{\xi \leq 1} = \frac{1}{2m_i} (Z^2ndt_L)^2, \quad (6.4)$$

where m_i is the mass of the target ions in units of electron mass m_e .

In reality, the energy will be less when the one-dimensional description breaks down, i.e., when the separation distance L_s approaches the diameter of the laser focal spot $2 \cdot r_L$. This would lead to a lower ion energy in eq. (6.4) and may be described by replacing the

laser pulse duration t_L by the value $2 \cdot r_L/c$; here the electrons are assumed to move with speed of light away from the ions given them a shorter time, i.e. $2 \cdot r_L/c$ to respond on the charge separation fields.

ii) For $\xi > 1$, we assume that the foil remains in its initial shape, and the laser pulse is totally reflected by the target ($R = 1$, $T = 0$ in eq. (6.2)). Then the foil is accelerated by the light pressure, and the equation of motion reads [134, 82]

$$\frac{dp}{dt} = Z \cdot \frac{a_0}{\xi} \cdot \frac{\sqrt{1 + p^2} - p}{\sqrt{1 + p^2} + p}, \quad (6.5)$$

where p is the momentum of a single ion of the foil. In the non-relativistic approximation, the corresponding kinetic energy of the ion is given by

$$E_{\xi > 1} = \frac{1}{2m_i} \left(\frac{Za_0 t_L}{\xi} \right)^2. \quad (6.6)$$

It is worth noting that the motion of the foil becomes relativistic, when the momentum $p = Z a_0 t_L / \xi$ equals 1. For $\xi = 1$ and $t_L = 2\pi$ (single laser cycle), these conditions mark the transition to the laser piston acceleration regime as discussed by Esirkepov *et al.* [134]. The corresponding laser amplitude $a_0^{LP} = m_i / (2\pi) = 1836 / (2\pi)$ is equivalent to an intensity of $7 \times 10^{23} \text{ W/cm}^2$ at $1 \mu\text{m}$ wavelength for a hydrogen target.

Comparing eqs. (6.4) and (6.6) it is evident that they are identical for $a_0 = Znd$ which is similar to the ad-hoc definition given in eq. (6.3). Therefore, the ion energy expected for optimal conditions can be approximated by

$$E_{opt} = \left(\sqrt{(Za_0 t_L)^2 + m_i^2} - m_i \right), \quad (6.7)$$

which is the relativistic analogy to eq. (6.4).

6.3 Simulations

6.3.1 Optimal conditions for ion acceleration

The plasma density used throughout the chapter is $100 n_{cr}$ and was chosen to be lower than solid state densities. This is for the sake of simplicity in order to study the basic properties of the ion acceleration with thin foils. The results of this study can be scaled to real densities. The spatial step is equal to 0.5nm , each plasma cell is initially occupied by 400 macro-particles of each kind (electrons and ions). The ions in this study are assumed to be protons. The laser pulse has a Gaussian envelope, and its duration is the FWHM-value of the electric field envelope. Throughout the chapter the duration of the laser pulse is chosen to be 15 cycles, corresponding to approximately 40 fs for $\lambda_L = 800\text{nm}$. In all simulations presented in this work, the density gradient scale length at the plasma-vacuum interface was taken to be zero, i.e. the laser pulse interacts with step-like density profile.

The transition between the regimes $\xi \leq 1$ and $\xi > 1$ is apparent in figure 6.3a, where the proton energy is plotted versus the parameter ξ (eq. (6.3)) for different laser pulse amplitudes a_0 . For simple illustrative reasons, we have set $\xi = \xi(R = 1, T = 0)$, implying full reflection and zero transmission. This is actually not true for the thin foils considered here, where transmission is significant, as we saw in figures 6.1) and 6.2). Nevertheless, we find from 1D simulations that peak proton bunch energy occurs for $\xi \approx 1$, almost independent of laser amplitude. The important message is then that the optimum foil thickness $(nd)_{opt}$ scales linearly with laser amplitude a_0 . Plotting both quantities from simulations for Gaussian-shaped pulses in figure 6.3b, we find indeed proportionality

$$(nd)_{opt} \approx a_0, \quad (6.8)$$

given by the dashed line in the important range of $1 < a_0 < 20$. Also for other pulse shapes, the relation $(nd)_{opt} \approx f \cdot a_0$ remains valid, but with different proportionality factor f , for example, we obtain $f \approx 2$ for a flat-top laser pulse. Deviations show up at larger a_0 . Those

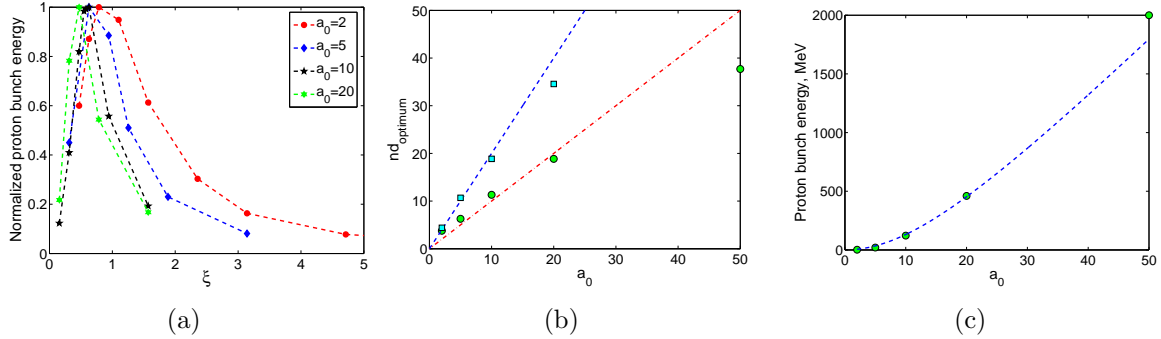


Figure 6.3: Results of 1D PIC simulations. (a) Proton bunch energy versus the parameter ξ for different laser amplitudes a_0 . (b) Dependence of the optimum mass-density $(nd)_{opt}$ on a_0 for a laser pulse with gaussian envelope (circles) and for a flat-top pulse (squares); the dashed and dash-dot lines correspond to $(nd)_{opt} = a_0$ and $(nd)_{opt} = 2a_0$ respectively. (c) Dependence of ion bunch energy on a_0 obtained from simulation (circles) and from eq. (6.4) (dashed line).

are probably due to the highly simplified derivation of the threshold for complete electron separation. For large values of a_0 the response of the ions to the growing longitudinal electrostatic field can not be neglected anymore and should be taken into account in the pressure balance equation (eq. (6.2)). With this respect, the motion of the ions becomes important when they approach the speed of light within the initial separation case, which is likely to happen for the case $a_0 = 50$ (figure 6.3b, c).

Finally figure 6.3c shows the ion bunch energy versus a_0 obtained from simulations (circles) and from eq. (6.7) (dashed line) setting $\xi = 1$. It is visible that the ion bunch energy grows proportionally to a_0^2 (eq. (6.6)) and therefore to the laser pulse energy as long as the ion motion is non-relativistic.

6.3.2 Ellipticity effects

Suppression of pre-pulses, which tend to degrade density profiles of targets before the main pulse arrives, is required in many experiments. Plasma mirrors have been successfully used in this case to achieve high contrast laser pulses [135, 136]. In the context of the present paper, however, pulses are needed having both high contrast and circular polarization.

The problem then is that plasma mirrors will change the polarization of obliquely incident pulses from circular to elliptical, because the p-polarized component is absorbed more strongly than the s-polarized one. Since the plasma-mirrors are often used after the main focusing optics of the laser system, i.e., shortly before target interaction, their effect on the polarization needs to be controlled.

Motivated by this experimental problem, we have studied how the generation of mono-energetic ion beams degrades with decreasing ellipticity and what is the minimum value. Here we define ellipticity as the ratio between the two field components $\epsilon = E_y/E_z$, supposing that the phase difference between them is equal to $\pi/2$ and that $E_y < E_z$. Results are shown in figure 6.4. Figure 6.4a exhibits ion energy spectra for $a_0 = 20$ and decreasing values of ellipticity. One can see that energies and strengths of spectral peaks diminish with decreasing ellipticity and disappear for $\epsilon < 0.7$. In figure 6.4b, the dependence of the threshold ellipticity on laser amplitude a_0 is plotted. For each a_0 the thickness of the target was chosen to be optimal according to the results of the previous chapter. One observes that the threshold ellipticity of $\epsilon \approx 0.7$ is almost independent of a_0 , though it slightly falls for $a_0 < 7$. We attribute this latter tendency to reduced electron heating at lower laser amplitudes.

Finally figure 6.3c shows the dependence of the energy of the ion bunch on ellipticity for $a_0 = 20$. The ellipticity is shown in the range from ϵ_{thr} to $\epsilon = 1$ (circular polarization). The results on peak ion energy can be approximately described by the relation

$$E_{ion} = E_{circ} \sqrt{(\epsilon - \epsilon_{thr}) / (1 - \epsilon_{thr})}, \quad (6.9)$$

where E_{circ} is the peak ion energy for circular polarization and $\epsilon_{thr} \approx 0.7$ the threshold ellipticity.

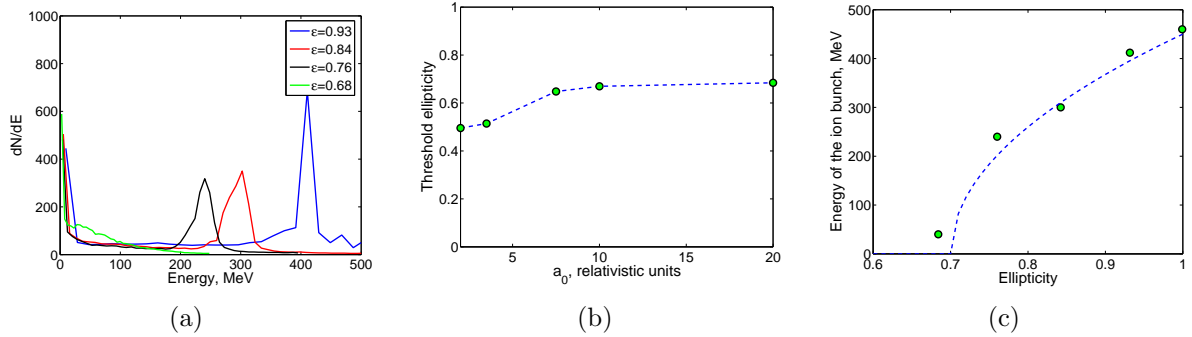


Figure 6.4: a) Proton energy spectra for $a_0 = 20$ and different ellipticities. b) Dependence of threshold ellipticity on a_0 . c) Dependence of the proton bunch energy on ellipticity for $a_0 = 20$. Beam parameters are the same as for figure 3.

6.4 Summary of the chapter.

The present study is restricted to one-dimensional analysis and simulation. Multi-dimensional effects have been discussed by Klimo *et al.* [81], in particular lateral decay of the ion bunch which limits the time interval available for acceleration to $t_m = \sqrt{2\xi\sigma/a_0}$. Here σ denotes the FWHM diameter of a Gaussian radial intensity distribution. The maximum ion energy then follows from eq. (6.6); for SI-units and $\xi > 1$, we find $E_m = (4\sqrt{\ln 2}m_i c^2/\xi)\sqrt{P_L/P_{Ri}}$, where the *ion relativistic power unit* $P_{Ri} = 4\pi\varepsilon_0 m_i^2 c^5/(Z^2 e^2) = 29.3\text{PW}$ for protons. Under optimal conditions ($\xi \approx 1$), this implies proton energies close to 1 GeV for a laser power of around 3 PW.

In conclusion, the results of the present chapter clarify two important points: First the areal density optimal for ion acceleration was found to be $(nd)_{opt} \approx a_0$. Second the degradation of peaked ion spectra as a function of ellipticity of the driving laser beam has been investigated. Peaked spectra exist for $\epsilon > 0.7$, and ion energy decreases $\propto \sqrt{\epsilon - 0.7}$. These results are important when using plasma mirrors for high contrast in upcoming experiments.

Circular polarization may be achieved even when using plasma mirrors. For this one has to take into account the different reflection coefficients for s- and p-polarization and choose the ellipticity of the incoming beam such that it results in circular polarization

after reflection. Deviations from complete circular polarization in the range of 10% can be tolerated, but should not exceed 30 %.

Chapter 7

Conclusions

This thesis is devoted to theoretical and numerical studies of overdense plasmas, which being irradiated by intense laser light become a source of charged particles and photons. Proof-of-principle experiments have been conducted in many laboratories of the world showing outstanding characteristics of beams of electrons, ions and photons. This has raised a lot of discussions on possible applications of such beams. However, before making these sources a scientific or medical instrument one needs to know how to control the process. This is the main emphasis of the thesis - studies of ways of controlling the two processes that occur during the interaction of intense laser pulses with overdense plasmas - generation of high-order harmonics of the fundamental laser frequency and generation of monoenergetic ion beams.

7.1 Controlling the generation of attosecond pulses.

7.1.1 Controlling the temporal structure of attosecond pulses.

As shown in Chapter 3, the harmonics of the fundamental laser frequency are generated in the form of trains of attosecond pulses due to the forced oscillations of the reflecting surface. In most cases single attosecond pulse is desirable. The only way to generate a single pulse and not a train of pulses is to reduce the number of oscillations of the reflecting

surface with the help of the gating. Here one can use either 2-cycle pulses - thus introduce *intensity gating*, or use pulses with dynamically changing polarization. According to the simple one-particle model presented in Chapter 3, the pulses with circular polarization do not produce oscillations of the surface and thus no harmonics are generated. If the pulse is constructed in the way that it possesses linear polarization only during short time and all other moments the polarization is circular then one can effectively confine the generation of attosecond pulses to the time period when the polarization is linear. This method is called *polarization gating* and is discussed in detail in Chapter 4. It is shown that *polarization gating* technique works both in the case of normal and oblique incidence, which makes this scheme a candidate for experimental generation of intense single attosecond pulses using multi-cycle laser pulses.

7.1.2 Controlling the spatial structure of attosecond pulses.

Controlling the spatial structure of high-order harmonics generated on the surface of over-dense plasma is especially important in the view of Coherent Harmonic Focusing [53] that would possibly allow to reach the Schwinger limit [50].

In Chapter 5 it is shown that inhomogeneous lateral intensity distribution of the driving laser pulse leads to target denting. Target denting can be either adiabatic, i.e. due to the slow hydrodynamic ion motion, or non-adiabatic, i.e. due to the fast motion of the electrons, and leads to the *parasitic* and *uncontrolled* focusing. After the harmonic beam is focused in the vicinity of the target it diverges and all harmonic orders have the same divergence angle.

In order to control the divergence of harmonic beam one can pursue two ways - either shaping the lateral intensity distribution of the laser pulse or shaping the target. In the case of the concave target, harmonic beam can be focused in the *controlled* way, theoretically leading to extreme intensity in the focus. However, as the focus is located in the close vicinity of the target, where there are a lot of particles, experimental value of such a scheme is questionable. In many cases the harmonic beam needs to be propagated a long

distance to the sample. In this case, one can think about straightening the wave-fronts of the generated harmonics and thus reducing the divergence angle. This can be done by reducing the denting of the target either by using flat-top laser pulses or by using convex targets.

Surface roughness can greatly affect the generation of the high-order harmonics and lead to the loss of the spatial coherence in the harmonic beam. In Chapter 5 it is shown that surface smoothing of a rough target surface during the interaction of relativistically intense laser pulse can be sufficient to allow diffraction limited beaming of harmonic radiation - contrary to expectation based on the Rayleigh criterion. This effect does not rely on the slow, adiabatic smoothing due to ion motion and is a direct result of the large spatial amplitude of the electron trajectories in relativistic laser interactions. This finding has direct impact on the peak intensities that can be achieved at shortest wavelengths and suggests that extremely high quality keV harmonic beams are achievable.

7.2 Controlling the generation of ion beams

The results presented in Chapter 6 clarify two important points: first, optimal conditions for generation of mono-energetic ion beams using the circularly polarized are found. Most energetic ion beams are generated when the laser pressure is just enough to displace all the electrons of the target from the ions. It is predicted that ion bunches with energies up to 1 GeV can be generated with state-of-the-art laser systems.

Second, the degradation of peaked ion spectra as a function of ellipticity of the driving laser beam has been investigated. The results of these studies are important when using plasma mirrors for high contrast in upcoming experiments. Circular polarization may be achieved even when using plasma mirrors. For this one has to take into account the different reflection coefficients for s- and p-polarization and choose the ellipticity of the incoming beam such that it results in circular polarization after reflection. Deviations from complete circular polarization in the range of 10 percents can be tolerated, but should not exceed 30 percents.

Bibliography

- [1] S.-W. Bahk, P. Rousseau, T. A. Planchon, V. Chvykov, G. Kalintchenko, A. Maksimchuk, G. A. Mourou and V. Yanovsky. *Generation and characterization of the highest laser intensities (10^{22} W/cm^2)*. Opt. Lett., **29**(24), 2837–2839 (2004).
- [2] V. V. Lozhkarev, G. I. Freidman, V. N. Ginzburg, E. V. Katin, E. A. Khazanov, A. V. Kirsanov, G. A. Luchinin, A. N. Mal'shakov, M. A. Martyanov, O. V. Palashov, A. K. Poteomkin, A. M. Sergeev, A. A. Shaykin, I. V. Yakovlev, S. G. Garanin, S. A. Sukharev, N. N. Rukavishnikov, A. V. Charukhchev, R. R. Gerke and V. E. Yashin. *200 TW 45 fs laser based on optical parametric chirped pulse amplification*. Opt. Express, **14**(1), 446–454 (2006).
- [3] D. Strickland and G. Mourou. *Compression of amplified chirped optical pulses*. Optics Communications, **56**(3), 219 – 221 (1985).
- [4] L. Landau. *The Classical Theory of Fields*. Pergamon Press, Oxford (1975).
- [5] E. S. Sarachik and G. T. Schappert. *Classical Theory of the Scattering of Intense Laser Radiation by Free Electrons*. Phys. Rev. D, **1**(10), 2738–2753 (1970).
- [6] A. Pukhov. *Strong field interaction of laser radiation*. Reports on Progress in Physics, **66**(1), 47–101 (2003).
- [7] G. A. Mourou, T. Tajima and S. V. Bulanov. *Optics in the relativistic regime*. Reviews of Modern Physics, **78**(2), 309 (2006).

[8] D. Umstadter. *Relativistic laser-plasma interactions*. Journal of Physics D: Applied Physics, **36**(8), R151–R165 (2003).

[9] U. Teubner and P. Gibbon. *High-order harmonics from laser-irradiated plasma surfaces*. Reviews of Modern Physics, **81**(2), 445 (2009).

[10] J. Faure, Y. Glinec, A. Pukhov, S. Kiselev, S. Gordienko, E. Lefebvre, J.-P. Rousseau, F. Burgy and V. Malka. *A laser-plasma accelerator producing monoenergetic electron beams*. Nature, **431**(7008), 541–544 (2004).

[11] S. P. D. Mangles, C. D. Murphy, Z. Najmudin, A. G. R. Thomas, J. L. Collier, A. E. Dangor, E. J. Divall, P. S. Foster, J. G. Gallacher, C. J. Hooker, D. A. Jaroszynski, A. J. Langley, W. B. Mori, P. A. Norreys, F. S. Tsung, R. Viskup, B. R. Walton and K. Krushelnick. *Monoenergetic beams of relativistic electrons from intense laser-plasma interactions*. Nature, **431**(7008), 535–538 (2004).

[12] C. G. R. Geddes, C. Toth, J. van Tilborg, E. Esarey, C. B. Schroeder, D. Bruhwiler, C. Nieter, J. Cary and W. P. Leemans. *High-quality electron beams from a laser wake-field accelerator using plasma-channel guiding*. Nature, **431**(7008), 538–541 (2004).

[13] W. P. Leemans, B. Nagler, A. J. Gonsalves, C. Toth, K. Nakamura, C. G. R. Geddes, E. Esarey, C. B. Schroeder and S. M. Hooker. *GeV electron beams from a centimetre-scale accelerator*. Nat Phys, **2**(10), 696–699 (2006).

[14] J. Osterhoff, A. Popp, Z. Major, B. Marx, T. P. Rowlands-Rees, M. Fuchs, M. Geissler, R. Hörlein, B. Hidding, S. Becker, E. A. Peralta, U. Schramm, F. Grüner, D. Habs, F. Krausz, S. M. Hooker and S. Karsch. *Generation of Stable, Low-Divergence Electron Beams by Laser-Wakefield Acceleration in a Steady-State-Flow Gas Cell*. Physical Review Letters, **101**(8), 085002 (2008).

[15] S. Karsch, J. Osterhoff, A. Popp, T. P. Rowlands-Rees, Z. Major, M. Fuchs, B. Marx, R. Hörlein, K. Schmid, L. Veisz, S. Becker, U. Schramm, B. Hidding, G. Pretzler,

D. Habs, F. Grüner, F. Krausz and S. M. Hooker. *GeV-scale electron acceleration in a gas-filled capillary discharge waveguide*. New Journal of Physics, **9**(11), 415 (2007).

[16] A. Rousse, K. T. Phuoc, R. Shah, A. Pukhov, E. Lefebvre, V. Malka, S. Kiselev, F. Burgy, J.-P. Rousseau, D. Umstadter and D. Hulin. *Production of a keV X-Ray Beam from Synchrotron Radiation in Relativistic Laser-Plasma Interaction*. Phys. Rev. Lett., **93**(13), 135005 (2004).

[17] M. Fuchs, R. Weingartner, A. Popp, Z. Major, S. Becker, J. Osterhoff, R. Hrlein, G. D. Tsakiris, U. Schramm, B. Hidding, T. P. Rowlands-Rees, S. M. Hooker, D. Habs, F. Krausz, S. Karsch and F. Grüner. *Table-top laser-driven ultrafast undulator radiation in the soft x-ray range*. Accepted to Nature Physics.

[18] N. H. Burnett, H. A. Baldis, M. C. Richardson and G. D. Enright. *Harmonic generation in CO₂ laser target interaction*. Applied Physics Letters, **31**(3), 172–174 (1977).

[19] R. L. Carman, C. K. Rhodes and R. F. Benjamin. *Observation of harmonics in the visible and ultraviolet created in CO₂ laser-produced plasmas*. Phys. Rev. A, **24**(5), 2649–2663 (1981).

[20] R. L. Carman, D. W. Forslund and J. M. Kindel. *Visible Harmonic Emission as a Way of Measuring Profile Steepening*. Phys. Rev. Lett., **46**(1), 29–32 (1981).

[21] S. Kohlweyer, G. D. Tsakiris, C. G. Wahlström, C. Tillman and I. Mercer. *Harmonic generation from solid-vacuum interface irradiated at high laser intensities*. Optics Communications, **117**(5-6), 431 – 438 (1995).

[22] D. von der Linde, T. Engers, G. Jenke, P. Agostini, G. Grillon, E. Nibbering, A. Mysyrowicz and A. Antonetti. *Generation of high-order harmonics from solid surfaces by intense femtosecond laser pulses*. Phys. Rev. A, **52**(1), R25–R27 (1995).

[23] P. A. Norreys, M. Zepf, S. Moustakidis, A. P. Fews, J. Zhang, P. Lee, M. Bakarezos, C. N. Danson, A. Dyson, P. Gibbon, P. Loukakos, D. Neely, F. N. Walsh, J. S. Wark

and A. E. Dangor. *Efficient Extreme UV Harmonics Generated from Picosecond Laser Pulse Interactions with Solid Targets*. Phys. Rev. Lett., **76**(11), 1832–1835 (1996).

[24] U. Teubner, G. Pretzler, T. Schlegel, K. Eidmann, E. Förster and K. Witte. *Anomalies in high-order harmonic generation at relativistic intensities*. Phys. Rev. A, **67**(1), 013816 (2003).

[25] B. Dromey, S. Kar, C. Bellei, D. C. Carroll, R. J. Clarke, J. S. Green, S. Kneip, K. Markey, S. R. Nagel, P. T. Simpson, L. Willingale, P. McKenna, D. Neely, Z. Najmudin, K. Krushelnick, P. A. Norreys and M. Zepf. *Bright multi-keV harmonic generation from relativistically oscillating plasma surfaces*. Phys. Rev. Lett., **99**(8), 085001 (2007).

[26] B. Dromey, M. Zepf, A. Gopal, K. Lancaster, M. S. Wei, K. Krushelnick, M. Tatarakis, N. Vakakis, S. Moustazis, R. Kodama, M. Tampo, C. Stoeckl, R. Clarke, H. Habara, D. Neely, S. Karsch and P. Norreys. *High harmonic generation in the relativistic limit*. Nat. Phys., **2**(7), 456–459 (2006).

[27] R. Hörlein, Y. Nomura, J. Osterhoff, Z. Major, S. Karsch, F. Krausz and G. D. Tsakiris. *High harmonics from solid surfaces as a source of ultra-bright XUV radiation for experiments*. Plasma Phys. Control. Fusion, **50**, 124002 (2008).

[28] B. Dromey, D. Adams, R. Hörlein, Y. Nomura, S. G. Rykovanov, D. C. Carroll, P. S. Foster, S. Kar, K. Markey, P. McKenna, D. Neely, M. Geissler, G. D. Tsakiris and M. Zepf. *Diffraction limited performance and focusing of high harmonics from relativistic plasmas*. Nat. Phys., **5**(2), 146–152 (2009).

[29] Y. Nomura, R. Hörlein, P. Tzallas, B. Dromey, S. Rykovanov, Z. Major, J. Osterhoff, S. Karsch, L. Veisz, M. Zepf, D. Charalambidis, F. Krausz and G. D. Tsakiris. *Attosecond phase-locking of harmonics emitted from laser-produced plasmas*. Nat. Phys., **5**(2), 124–128 (2009).

- [30] B. Bezzerides, R. D. Jones and D. W. Forslund. *Plasma mechanism for ultraviolet harmonic radiation due to intense CO₂ light.* Phys. Rev. Lett., **49**(3), 202–205 (1982).
- [31] S. V. Bulanov, N. M. Naumova and F. Pegoraro. *Interaction of an ultrashort, relativistically strong laser pulse with an overdense plasma.* Physics of Plasmas, **1**(3), 745–757 (1994).
- [32] P. Gibbon. *Harmonic Generation by Femtosecond Laser-Solid Interaction: A Coherent Water-Window Light Source?* Phys. Rev. Lett., **76**(1), 50–53 (1996).
- [33] R. Lichters and J. Meyer-ter Vehn. *High laser harmonics from plasma surfaces: Intensity and angular dependence, cutoffs and resonance layers at density ramps.* Multiphoton Processes 1996 IOP Conference Series, **154**, 221–230 (1997).
- [34] V. L. Ginzburg. *The Propagation of Electromagnetic Waves in Plasmas.* Pergamon, New York (1964).
- [35] F. Brunel. *Not-so-resonant, resonant absorption.* Phys. Rev. Lett., **59**(1), 52 (1987).
- [36] U. Teubner, K. Eidmann, U. Wagner, U. Andiel, F. Pisani, G. D. Tsakiris, K. Witte, J. Meyer-ter Vehn, T. Schlegel and E. Förster. *Harmonic emission from the rear side of thin overdense foils irradiated with intense ultrashort laser pulses.* Phys. Rev. Lett., **92**(18), 185001 (2004).
- [37] A. Tarasevitch, K. Lobov, C. Wuensche and D. von der Linde. *Transition to the relativistic regime in high order harmonic generation.* Phys. Rev. Lett., **98**(10), 103902 (2007).
- [38] F. Quéré, C. Thaury, P. Monot, S. Dobosz, P. Martin, J.-P. Geindre and P. Audebert. *Coherent wake emission of high-order harmonics from overdense plasmas.* Phys. Rev. Lett., **96**(12), 125004 (2006).
- [39] F. Krausz and M. Ivanov. *Attosecond physics.* Reviews of Modern Physics, **81**(1), 163 (2009).

- [40] P. B. Corkum. *Plasma perspective on strong field multiphoton ionization*. Phys. Rev. Lett., **71**(13), 1994–1997 (1993).
- [41] G. Farkas and C. Toth. *Proposal for attosecond light pulse generation using laser induced multiple-harmonic conversion processes in rare gases*. Phys. Lett. A, **168**, 447–450 (1992).
- [42] S. E. Harris, J. J. Macklin and T. W. Hänsch. *Atomic scale temporal structure inherent to high-order harmonic generation*. Optics Communications, **100**(5-6), 487 – 490 (1993).
- [43] M. Hentschel, R. Kienberger, C. Spielmann, G. A. Reider, N. Milosevic, T. Brabec, P. Corkum, U. Heinzmann, M. Drescher and F. Krausz. *Attosecond metrology*. Nature, **414**, 509–513 (2001).
- [44] R. Kienberger, E. Goulielmakis, M. Uiberacker, A. Baltuska, V. Yakovlev, F. Bammer, A. Scrinzi, T. Westerwalbesloh, U. Kleineberg, U. Heinzmann, M. Drescher and F. Krausz. *Atomic transient recorder*. Nature, **427**(6977), 817–821 (2004).
- [45] E. Goulielmakis, M. Uiberacker, R. Kienberger, A. Baltuska, V. Yakovlev, A. Scrinzi, T. Westerwalbesloh, U. Kleineberg, U. Heinzmann, M. Drescher and F. Krausz. *Direct Measurement of Light Waves*. Science, **305**(5688), 1267–1269 (2004).
- [46] M. Drescher, M. Hentschel, R. Kienberger, M. Uiberacker, V. Yakovlev, A. Scrinzi, T. Westerwalbesloh, U. Kleineberg, U. Heinzmann and F. Krausz. *Time-resolved atomic inner-shell spectroscopy*. Nature, **419**(6909), 803–807 (2002).
- [47] M. Uiberacker, T. Uphues, M. Schultze, A. J. Verhoef, V. Yakovlev, M. F. Kling, J. Rauschenberger, N. M. Kabachnik, H. Schroder, M. Lezius, K. L. Kompa, H.-G. Muller, M. J. J. Vrakking, S. Hendel, U. Kleineberg, U. Heinzmann, M. Drescher and F. Krausz. *Attosecond real-time observation of electron tunnelling in atoms*. Nature, **446**(7136), 627–632 (2007).

[48] A. L. Cavalieri, N. Muller, T. Uphues, V. S. Yakovlev, A. Baltuska, B. Horvath, B. Schmidt, L. Blumel, R. Holzwarth, S. Hendel, M. Drescher, U. Kleineberg, P. M. Echenique, R. Kienberger, F. Krausz and U. Heinzmann. *Attosecond spectroscopy in condensed matter*. *Nature*, **449**(7165), 1029–1032 (2007).

[49] J. Feist, S. Nagele, R. Pazourek, E. Persson, B. I. Schneider, L. A. Collins and J. Burgdörfer. *Nonsequential two-photon double ionization of helium*. *Phys. Rev. A*, **77**(4), 043420 (2008).

[50] J. Schwinger. *On gauge invariance and vacuum polarization*. *Phys. Rev.*, **82**(5), 664–679 (1951).

[51] URL <http://www.extreme-light-infrastructure.eu/>.

[52] URL www.hiper-laser.org/.

[53] S. Gordienko, A. Pukhov, O. Shorokhov and T. Baeva. *Coherent focusing of high harmonics: A new way towards the extreme intensities*. *Phys. Rev. Lett.*, **94**(10), 103903 (2005).

[54] R. Hörlein, S. Rykovanov, B. Dromey, Y. Nomura, D. Adams, M. Geissler, M. Zepf, F. Krausz and G. Tsakiris. *Controlling the divergence of high harmonics from solid targets: a route toward coherent harmonic focusing*. *European Journal of Physics D: Applied Physics*, **online**, DOI: [10.1140/epjd/e2009-00084-x](https://doi.org/10.1140/epjd/e2009-00084-x) (2009).

[55] W. L. Kruer and K. Estabrook. *J x B heating by very intense laser light*. *Physics of Fluids*, **28**(1), 430–432 (1985).

[56] A. V. Gurevich, L. V. Pariiskaya and L. P. Pitaevskii. *Automodel motion of a rarefied plasma*. *Zhurnal Eksperimental'noi i Teoreticheskoi Fiziki*, **49**, 647–654 (1965).

[57] S. C. Wilks, A. B. Langdon, T. E. Cowan, M. Roth, M. Singh, S. Hatchett, M. H. Key, D. Pennington, A. MacKinnon and R. A. Snavely. *Energetic proton generation in ultra-intense laser–solid interactions*. *Physics of Plasmas*, **8**(2), 542–549 (2001).

[58] H. Ruhl and P. Mulser. *Relativistic Vlasov simulation of intense fs laser pulse-matter interaction*. Physics Letters A, **205**, 388–392 (1995).

[59] T. Z. Esirkepov, S. V. Bulanov, K. Nishihara, T. Tajima, F. Pegoraro, V. S. Khoroshkov, K. Mima, H. Daido, Y. Kato, Y. Kitagawa, K. Nagai and S. Sakabe. *Proposed Double-Layer Target for the Generation of High-Quality Laser-Accelerated Ion Beams*. Phys. Rev. Lett., **89**(17), 175003 (2002).

[60] L. O. Silva, M. Marti, J. R. Davies, R. A. Fonseca, C. Ren, F. S. Tsung and W. B. Mori. *Proton Shock Acceleration in Laser-Plasma Interactions*. Phys. Rev. Lett., **92**(1), 015002 (2004).

[61] V. S. Belyaev, V. P. Krainov, V. S. Lisitsa and A. P. Matafonova. *Generation of fast charged particles and superstrong magnetic fields in the interaction of ultrashort high-intensity laser pulses with solid targets*. Phys. Usp., **178**, 823847 (2007).

[62] E. d’Humières, E. Lefebvre, L. Gremillet and V. Malka. *Proton acceleration mechanisms in high-intensity laser interaction with thin foils*. Physics of Plasmas, **12**(6), 062704 (2005).

[63] P. Antici, J. Fuchs, E. d’Humières, E. Lefebvre, M. Borghesi, E. Brambrink, C. A. Cecchetti, S. Gaillard, L. Romagnani, Y. Sentoku, T. Toncian, O. Willi, P. Audebert and H. Pépin. *Energetic protons generated by ultrahigh contrast laser pulses interacting with ultrathin targets*. Physics of Plasmas, **14**(3), 030701 (2007).

[64] J. Fuchs, Y. Sentoku, S. Karsch, J. Cobble, P. Audebert, A. Kemp, A. Nikroo, P. Antici, E. Brambrink, A. Blazevic, E. M. Campbell, J. C. Fernández, J.-C. Gauthier, M. Geissel, M. Hegelich, H. Pépin, H. Popescu, N. Renard-LeGalloudec, M. Roth, J. Schreiber, R. Stephens and T. E. Cowan. *Comparison of Laser Ion Acceleration from the Front and Rear Surfaces of Thin Foils*. Phys. Rev. Lett., **94**(4), 045004 (2005).

[65] M. Hegelich, S. Karsch, G. Pretzler, D. Habs, K. Witte, W. Guenther, M. Allen, A. Blazevic, J. Fuchs, J. C. Gauthier, M. Geissel, P. Audebert, T. Cowan and M. Roth. *MeV Ion Jets from Short-Pulse-Laser Interaction with Thin Foils*. Phys. Rev. Lett., **89**(8), 085002 (2002).

[66] A. J. Mackinnon, Y. Sentoku, P. K. Patel, D. W. Price, S. Hatchett, M. H. Key, C. Andersen, R. Snavely and R. R. Freeman. *Enhancement of Proton Acceleration by Hot-Electron Recirculation in Thin Foils Irradiated by Ultraintense Laser Pulses*. Phys. Rev. Lett., **88**(21), 215006 (2002).

[67] L. Robson, P. T. Simpson, R. J. Clarke, K. W. D. Ledingham, F. Lindau, O. Lundh, T. McCann, P. Mora, D. Neely, C. G. Wahlstrom, M. Zepf and P. McKenna. *Scaling of proton acceleration driven by petawatt-laser-plasma interactions*. Nat. Phys., **3**(1), 58–62 (2007).

[68] J. Schreiber, F. Bell, F. Grüner, U. Schramm, M. Geissler, M. Schnürer, S. Ter-Avetisyan, B. M. Hegelich, J. Cobble, E. Brambrink, J. Fuchs, P. Audebert and D. Habs. *Analytical Model for Ion Acceleration by High-Intensity Laser Pulses*. Physical Review Letters, **97**(4), 045005 (2006).

[69] V. Malka, S. Fritzler, E. Lefebvre, E. d'Humires, R. Ferrand, G. Grillon, C. Albarete, S. Meyroneinc, J. Chambaret, A. Antonetti and D. Hulin. *Practicability of protontherapy using compact laser systems*. Med. Phys., **31**, 1587–1592 (2004).

[70] S. V. Bulanov, H. Daido, T. Z. Esirkepov, V. S. Khoroshkov, J. Koga, K. Nishihara, F. Pegoraro, T. Tajima and M. Yamagiwa. *Feasibility of Using Laser Ion Accelerators in Proton Therapy*. In L. Hadzievski, N. Bibic and T. Grozdanov (editors), , volume 740, pp. 414–429. AIP (2004).

[71] Ledingham, K. W. D. Galster and W. Sauerbrey. *Laser-driven proton oncology a unique new cancer therapy?* Br. J. Radiol., **80**, 855–858 (2007).

[72] S. S. Bulanov, A. Brantov, V. Y. Bychenkov, V. Chvykov, G. Kalinchenko, T. Matsuoka, P. Rousseau, S. Reed, V. Yanovsky, K. Krushelnick, D. W. Litzenberg and A. Maksimchuk. *Accelerating protons to therapeutic energies with ultraintense, ultraclean, and ultrashort laser pulses*. Medical Physics, **35**(5), 1770–1776 (2008).

[73] S. Fritzler, V. Malka, G. Grillon, J. P. Rousseau, F. Burgy, E. Lefebvre, E. d'Humieres, P. McKenna and K. W. D. Ledingham. *Proton beams generated with high-intensity lasers: Applications to medical isotope production*. Applied Physics Letters, **83**(15), 3039–3041 (2003).

[74] E. Lefebvre, E. d'Humires, S. Fritzler and V. Malka. *Numerical simulation of isotope production for positron emission tomography with laser-accelerated ions*. J. Appl. Phys., **100**, 113308 (2006).

[75] A. J. Mackinnon, P. K. Patel, R. P. Town, M. J. Edwards, T. Phillips, S. C. Lerner, D. W. Price, D. Hicks, M. H. Key, S. Hatchett, S. C. Wilks, M. Borghesi, L. Romagnani, S. Kar, T. Toncian, G. Pretzler, O. Willi, M. Koenig, E. Martinolli, S. Lepape, A. Benuzzi-Mounaix, P. Audebert, J. C. Gauthier, J. King, R. Snavely, R. R. Freeman and T. Boehlly. *Proton radiography as an electromagnetic field and density perturbation diagnostic (invited)*. Review of Scientific Instruments, **75**(10), 3531–3536 (2004).

[76] M. Temporal, J. J. Honrubia and S. Atzeni. *Proton-beam driven fast ignition of inertially confined fuels: Reduction of the ignition energy by the use of two proton beams with radially shaped profiles*. Physics of Plasmas, **15**(5), 052702 (2008).

[77] N. Naumova, T. Schlegel, V. T. Tikhonchuk, C. Labaune, I. V. Sokolov and G. Mourou. *Hole Boring in a DT Pellet and Fast-Ion Ignition with Ultraintense Laser Pulses*. Physical Review Letters, **102**(2), 025002 (2009).

[78] H. Schwoerer, S. Pfotenhauer, O. Jackel, K. U. Amthor, B. Liesfeld, W. Ziegler, R. Sauerbrey, K. W. D. Ledingham and T. Esirkepov. *Laser-plasma acceleration*

of quasi-monoenergetic protons from microstructured targets. *Nature*, **439**(7075), 445–448 (2006).

[79] B. M. Hegelich, B. J. Albright, J. Cobble, K. Flippo, S. Letzring, M. Paffett, H. Ruhl, J. Schreiber, R. K. Schulze and J. C. Fernández. *Laser acceleration of quasi-monoenergetic MeV ion beams.* *Nature*, **439**, 441–444 (2006).

[80] S. Ter-Avetisyan, M. Schnürer, P. V. Nickles, M. Kalashnikov, E. Risse, T. Sokollik, W. Sandner, A. Andreev and V. Tikhonchuk. *Quasimonoenergetic Deuteron Bursts Produced by Ultraintense Laser Pulses.* *Physical Review Letters*, **96**(14), 145006 (2006).

[81] O. Klimo, J. Psikal, J. Limpouch and V. T. Tikhonchuk. *Monoenergetic ion beams from ultrathin foils irradiated by ultrahigh-contrast circularly polarized laser pulses.* *Phys. Rev. ST Accel. Beams*, **11**(3), 031301 (2008).

[82] A. P. L. Robinson, M. Zepf, S. Kar, R. G. Evans and C. Bellei. *Radiation pressure acceleration of thin foils with circularly polarized laser pulses.* *New Journal of Physics*, **10**(1), 013021 (13pp) (2008).

[83] T. V. Liseikina and A. Macchi. *Features of ion acceleration by circularly polarized laser pulses.* *Applied Physics Letters*, **91**(17), 171502 (2007).

[84] A. Macchi, F. Cattani, T. V. Liseykina and F. Cornolti. *Laser Acceleration of Ion Bunches at the Front Surface of Overdense Plasmas.* *Physical Review Letters*, **94**(16), 165003 (2005).

[85] A. Henig. Private communication.

[86] L. V. Keldysh. *Ionization in the field of a strong electromagnetic wave.* *Sov. Phys. JETP*, **20**, 1307 (1965).

[87] V. S. Popov. *Tunnel and multiphoton ionization of atoms and ions in a strong laser field (Keldysh theory).* *Phys. Usp.*, **174**, 921951 (2004).

[88] N. Delone and V. Krainov. *Tunneling and barrier-suppression ionization of atoms and ions in a laser radiation field*. Phys. Usp., **41**, 469 (1998).

[89] L. Landau and L. Pitaevskii. *Course of Theoretical Physics. Volume 10. Physical Kinetics*. Pergamon Press, Oxford (1981).

[90] A. A. Vlasov. *On Vibration Properties of Electron Gas (in Russian)*. Journal of Experimental and Theoretical Physics, **8**, 291 (1938).

[91] J. C. Maxwell. *A Dynamical Theory of the Electromagnetic Field*. Philosophical Transactions of the Royal Society of London, **155**, 459–512 (1865).

[92] C. K. Birdsall and A. B. Langdon. *Plasma Physics via Computer simulation*. McGraw-Hill Book Company (1985).

[93] R. W. Hockney and J. W. Eastwood. *Computer simulation using particles*. McGraw-Hill Book Company (1981).

[94] Y. N. Grigoryev, V. A. Vshivkov and M. P. Fedoruk. *Numerical Particle-In-Cell Methods: Theory and Applications*. Walter de Gruyter Inc (2002).

[95] A. Pukhov. *Three-dimensional electromagnetic relativistic particle-in-cell code VLPL (Virtual Laser Plasma Lab)*. Journal of Plasma Physics, **61**(03), 425–433 (1999).

[96] T. Umeda, Y. Omura, T. Tominaga and H. Matsumoto. *A new charge conservation method in electromagnetic particle-in-cell simulations*. Computer Physics Communications, **156**(1), 73 – 85 (2003).

[97] T. Z. Esirkepov. *Exact charge conservation scheme for Particle-in-Cell simulation with an arbitrary form-factor*. Computer Physics Communications, **135**(2), 144 – 153 (2001).

[98] J. Villasenor and O. Buneman. *Rigorous charge conservation for local electromagnetic field solvers*. Computer Physics Communications, **69**(2-3), 306 – 316 (1992).

[99] G. F. Bertsch, M. Bonitz, A. Filinov, V. S. Filinov, Y. Lozovik, D. Semkat and H. Ruhl. *Introduction to Computational Methods in Many-Body Physics*. Rinton Press, Princeton (2006).

[100] R. Lichters. *Relativistische Wechselwirkung intensiver kurzer Laserpulse mit überdichten Plasmen: Erzeugung hoher Harmonischer*. Ph.D. thesis, Technischen Universität München (1996).

[101] Y. Sentoku. Private communications.

[102] M. Born and E. Wolf. *Principles of optics*. Cambridge University Press, 7th edition (1999).

[103] J. Boris. *Relativistic plasma simulation optimization of a hybrid code*. In *Proc. the 4th Conf. on Numerical Simulation of Plasmas*, pp. 3-67 (1970).

[104] A. Einstein. *Zur Elektrodynamik bewegter Körper*. Annalen der Physik (Leipzig), **322**(10), 891 (1905).

[105] R. Lichters, J. Meyer-ter Vehn and A. Pukhov. *Short-pulse laser harmonics from oscillating plasma surfaces driven at relativistic intensity*. Phys. Plasmas, **3**(9), 3425–3437 (1996).

[106] G. D. Tsakiris, K. Eidmann, J. Meyer-ter Vehn and F. Krausz. *Route to intense single attosecond pulses*. New J. Phys., **8**, 19 (2006).

[107] S. Gordienko, A. Pukhov, O. Shorokhov and T. Baeva. *Relativistic Doppler effect: Universal spectra and zeptosecond pulses*. Phys. Rev. Lett., **93**(11), 115002 (2004).

[108] T. Baeva, S. Gordienko and A. Pukhov. *Theory of high-order harmonic generation in relativistic laser interaction with overdense plasma*. Phys. Rev. E, **74**(4), 046404 (2006).

- [109] D. F. Zaretsky, P. A. Korneev, S. V. Popruzhenko and W. Becker. *Landau damping in thin films irradiated by a strong laser field*. Journal of Physics B: Atomic, Molecular and Optical Physics, **37**(24), 4817–4830 (2004).
- [110] P. Mulser, D. Bauer and H. Ruhl. *Collisionless Laser-Energy Conversion by Anharmonic Resonance*. Physical Review Letters, **101**(22), 225002 (2008).
- [111] F. Olver. *Asymptotics and Special Functions*. Academic Press, New York (1974).
- [112] F. Tavella, A. Marcinkevicius and F. Krausz. *90 mJ parametric chirped pulse amplification of 10 fs pulses*. Opt. Express, **14**(26), 12822–12827 (2006).
- [113] P. B. Corkum, N. H. Burnett and M. Y. Ivanov. *Subfemtosecond pulses*. Opt. Lett., **19**(22), 1870 (1994).
- [114] V. T. Platonenko and V. V. Strelkov. *Single attosecond soft-x-ray pulse generated with a limited laser beam*. J. Opt. Soc. Am. B, **16**(3), 435–440 (1999).
- [115] O. Tcherbakoff, E. Mével, D. Descamps, J. Plumridge and E. Constant. *Time-gated high-order harmonic generation*. Phys. Rev. A, **68**(4), 043804 (2003).
- [116] T. Baeva, S. Gordienko and A. Pukhov. *Relativistic plasma control for single attosecond x-ray burst generation*. Physical Review E (Statistical, Nonlinear, and Soft Matter Physics), **74**(6), 065401 (2006).
- [117] G. Sansone, E. Benedetti, F. Calegari, C. Vozzi, L. Avaldi, R. Flammini, L. Poletto, P. Villoresi, C. Altucci, R. Velotta, S. Stagira, S. De Silvestri and M. Nisoli. *Isolated Single-Cycle Attosecond Pulses*. Science, **314**(5798), 443–446 (2006).
- [118] P. Tzallas, E. Skantzakis, C. Kalpouzos, E. P. Benis, G. D. Tsakiris and D. Charalambidis. *Generation of intense continuum extreme-ultraviolet radiation by many-cycle laser fields*. Nat Phys, **3**(12), 846–850 (2007).

[119] D. Charalambidis, P. Tzallas, E. P. Benis, E. Skantzakis, G. Maravelias, L. A. A. Nikolopoulos, A. P. Conde and G. D. Tsakiris. *Exploring intense attosecond pulses*. New Journal of Physics, **10**(2), 025018 (17pp) (2008).

[120] P. Goupillaud, A. Grossmann and J. Morlet. *Cycle-octave and related transforms in seismic signal analysis*. Geoexploration, **23**, 85–102 (1984).

[121] A. Bourdier. *Oblique incidence of a strong electromagnetic wave on a cold inhomogeneous electron plasma. Relativistic effects*. Physics of Fluids, **26**(7), 1804–1807 (1983).

[122] A. Di Piazza, K. Z. Hatsagortsyan and C. H. Keitel. *Harmonic generation from laser-driven vacuum*. Phys. Rev. D, **72**(8), 085005 (2005).

[123] A. Fedotov and N. Narozhny. *Generation of harmonics by a focused laser beam in the vacuum*. Phys. Lett. A, **362**, 1–5 (2007).

[124] N. Narozhny, S. Bulanov, V. Mur and V. Popov. *e^+e^- -pair production by a focused laser pulse in vacuum*. Phys. Lett. A, **330**, 1–6 (2004).

[125] M. Marklund and P. Shukla. *Nonlinear collective effects in photon-photon and photon-plasma interactions*. Rev. Mod. Phys., **78**, 591 (2006).

[126] M. Geissler, S. Rykovanov, J. Schreiber, J. M. ter Vehn and G. D. Tsakiris. *3D simulations of surface harmonic generation with few-cycle laser pulses*. New Journal of Physics, **9**(7), 218 (2007).

[127] A. Ishimaru. *Wave Propagation and Scattering in Random Media. Volume II: Multiple scattering, turbulence, rough surfaces and remote sensing*. Academic Press, New York (1978).

[128] S. Wilks, W. Kruer and W. Mori. *Odd harmonic generation of ultra-intense laser pulses reflected from an overdense plasma*. IEEE Trans. Plasma Science, **21**, 120 – 124 (1993).

- [129] Y. Sentoku, T. E. Cowan, A. Kemp and H. Ruhl. *High energy proton acceleration in interaction of short laser pulse with dense plasma target*. Physics of Plasmas, **10**(5), 2009–2015 (2003).
- [130] URL <http://www.iop.org/EJ/mmedia/1367-2630/10/11/113005/movie1lq.avi>.
- [131] URL <http://www.iop.org/EJ/mmedia/1367-2630/10/11/113005/movie2lq.avi>.
- [132] X. Zhang, B. Shen, X. Li, Z. Jin, F. Wang and M. Wen. *Efficient GeV ion generation by ultraintense circularly polarized laser pulse*. Physics of Plasmas, **14**(12), 123108 (2007).
- [133] X. Q. Yan, C. Lin, Z. M. Sheng, Z. Y. Guo, B. C. Liu, Y. R. Lu, J. X. Fan and J. E. Chen. *Generating High-Current Monoenergetic Proton Beams by a CircularlyPolarized Laser Pulse in the Phase-Stable Acceleration Regime*. Physical Review Letters, **100**(13), 135003–4 (2008).
- [134] T. Esirkepov, M. Borghesi, S. V. Bulanov, G. Mourou and T. Tajima. *Highly Efficient Relativistic-Ion Generation in the Laser-Piston Regime*. Phys. Rev. Lett., **92**(17), 175003 (2004).
- [135] B. Dromey, S. Kar, M. Zepf and P. Foster. *The plasma mirror—A subpicosecond optical switch for ultrahigh power lasers*. Review of Scientific Instruments, **75**(3), 645–649 (2004).
- [136] Y. Nomura, L. Veisz, K. Schmid, T. Wittmann, J. Wild and F. Krausz. *Time-resolved reflectivity measurements on a plasma mirror with few-cycle laser pulses*. New Journal of Physics, **9**(1), 9 (2007).

Publications

2009

- B. Dromey, **S. G. Rykovanov**, D. Adams, R. Hörlein, Y. Nomura, D. C. Carroll, P. S. Foster, S. Kar, K. Markey, P. McKenna, D. Neely, M. Geissler, G. D. Tsakiris, and M. Zepf
Tunable Enhancement of High Harmonic Emission from Laser Solid Interactions.
Phys. Rev. Lett., **102**, 225002 (2009).
- Y. Nomura, R. Hörlein, P. Tzallas, B. Dromey, **S. G. Rykovanov**, Zs. Major, J. Osterhoff, S. Karsch, L. Veisz, M. Zepf, D. Charalambidis, F. Krausz and G. D. Tsakiris.
Attosecond phase locking of harmonics emitted from laser-produced plasmas.
Nature Phys., **5**(2), 124–128 (2009).
- B. Dromey, D. Adams, R. Hörlein, Y. Nomura, **S. G. Rykovanov**, D. C. Carroll, P. S. Foster, S. Kar, K. Markey, P. McKenna, D. Neely, M. Geissler, G. D. Tsakiris and M. Zepf.
Diffraction limited performance and focusing of high harmonics from relativistic plasmas.
Nature Phys., **5**(2), 146–152 (2009).
- A. Henig, D. Kiefer, M. Geissler, **S. G. Rykovanov**, R. Ramis, R. Hörlein, J. Osterhoff, Zs. Major, L. Veisz, S. Karsch, F. Krausz, D. Habs, and J. Schreiber.

Laser-Driven Shock Acceleration of Ion Beams from Spherical Mass-Limited Targets.
 Phys. Rev. Lett., **102**, 095002 (2009)

- A. Henig, D. Kiefer, K. Markey, D. C. Gautier, K. A. Flippo, S. Letzring, R. P. Johnson, T. Shimada, L. Yin, B. J. Albright, K. J. Bowers, J. C. Fernandez, **S. G. Rykovanov**, H.-C. Wu, M. Zepf, D. Jung, V. Kh. Liechtenstein, J. Schreiber, D. Habs, and B. M. Hegelich.

Enhanced Laser-Driven Ion Acceleration in the Relativistic Transparency Regime.
 Phys. Rev. Lett., **103**, 045002 (2009)

- Rainer Hörlein, Yutaka Nomura, **Sergey G. Rykovanov**, George D. Tsakiris.
Factors influencing the temporal characteristics of coherent wake field harmonic emission from solid surfaces.

Proceedings of the SPIE, **7359**, pp. 73590D-73590D-8 (2009).

- M. Zepf, D. Adams, B. Dromey, M. Geissler, R. Hörlein, Y. Nomura, **S. Rykovanov**, G.D. Tsakiris.

Ultrabright attosecond sources from relativistically oscillating mirrors.
 Proceedings of the SPIE, **7359**, pp. 73590G-73590G-6 (2009).

- R. Hörlein, **S.G. Rykovanov**, B. Dromey, Y. Nomura, D. Adams, M. Geissler, M. Zepf, F. Krausz and G.D. Tsakiris.

Controlling the divergence of high harmonics from solid targets: a route toward coherent harmonic focusing.

Eur. Phys. J. D, DOI: 10.1140/epjd/e2009-00084-x (2009).

2008

- **S. G. Rykovanov**, J. Schreiber, J. Meyer-ter-Vehn, C. Bellei, A. Henig, H. C. Wu and M. Geissler

Ion acceleration with ultra-thin foils using elliptically polarized laser pulses.
 New J. Phys., **10**, 113005 (2008). (**IOP Select**)

- **S. G. Rykovanov**, M. Geissler, J. Meyer-ter-Vehn and G. D. Tsakiris.

Intense single attosecond pulses from surface harmonics using the polarization gating technique.

New J. Phys, **10**, 025025 (2008). (New Journal of Physics Best of 2008)

2007

- M. Geissler, **S. Rykovanov**, J. Schreiber, J. Meyer-ter-Vehn and G. D. Tsakiris.

3D simulations of surface harmonic generation with few-cycle laser pulses.

New J. Phys., **9**, 218 (2007)

- B. G. Bravy, V. M. Gordienko, V. T. Platonenko, **S. G. Rykovanov**, G. K. Vasiliev.
Sub-picosecond Petawatt class N_2O laser system: mid-IR non-linear optics and new possibilities for high energy physics.

Proceedings of SPIE, **6735**, 67350L (2007)

2005

- Y. M. Mikhailova, V. T. Platonenko, **S. G. Rykovanov**.

Generation of an attosecond X-ray pulse in a thin film irradiated by an ultrashort ultrarelativistic laser pulse.

JETP Letters, **81**, 571 (2005)

Submitted

- R. Hörlein, Y. Nomura, D. Herrmann, M. Stafe, I. Földes, **S. Rykovanov**, F. Tavella, A. Marcinkevicius, F. Krausz, L. Veisz and G. D. Tsakiris.

Few-cycle emission of high harmonics from solid density plasmas.

submitted to Phys. Rev. Lett.

In preparation

- R. Hörlein, Y. Nomura, P. Tzallas, **S.G. Rykovanov**, B. Dromey, J. Osterhoff, Zs. Major, S. Karsch, L. Veisz, M. Zepf, D. Charalambidis, F. Krausz, and G.D. Tsakiris. *Temporal Characterization of Attosecond Pulses Emitted from Solid Density Plasmas.* In preparation
- **S. G. Rykovanov**, H. Ruhl, J. Meyer-ter-Vehn, R. Hörlein, B. Dromey, M. Zepf, G.D. Tsakiris. *Non-adiabatic surface smoothing and generation of collimated attosecond pulses.* In preparation

Acknowledgements

Here I would like to thank all the people that supported me during my PhD time in Garching.

- First of all, I would like to thank Prof. Ferenc Krausz for giving me the opportunity to work in his group.
- Prof. Jürgen Meyer-ter-Vehn always took care of me and invited me first for the internship period and then to do my PhD thesis in MPQ. I am also indebted to him for many valuable discussions and ideas. He also changed the way I was looking at solving problems in physics. He is a great scientist!
- Dr. George Tsakiris was the direct supervisor of this thesis. I feel overwhelmingly lucky that I worked under his guidance all these years. I admire his deep understanding of physics, his patience and kindness.
- I would like to thank Prof. Hartmut Ruhl who accepted to be my supervisor. Discussions with him and his support helped me a lot. It is always great to interact with somebody who has such a broad range of interests.
- I thank Prof. Toshiki Tajima, Prof. Dietrich Habs, Prof. Stefan Karsch and Prof. Florian Grüner for kindly agreeing to be in my defence committee.
- I am specially grateful to Michael Geissler who not only helped me make my first steps in physics in MPQ, but also restored my interest in music. He is a great fellow.

- I am thankful to Jörg Schreiber for many hours he spend with me explaining the physics and of course for help with MATLAB. He has a vivid interest in physics and also "infected" me with it.
- This thesis would not be written without Yutaka Nomura and Rainer Hörlein. They conducted experiments in MPQ and let me participate from the theory side. It is great to discuss new ideas and results with them. I also thank Rainer Hörlein for translating the abstract of my thesis.
- I would like to thank Prof. Matt Zepf and Dr. Brendan Dromey for many new ideas and letting me participate in their experiments from the theory part. I am also indebted to them for many discussions outside physics.
- I thank Andreas Henig for discussions about ion acceleration and for being a great friend.
- I would like to thank my good friend Maxim Efremov, who spent enormous amount of time explaining physics and mathematics to me and supported me in any matter.
- Jens Osterhoff and Rainer Hörlein were basically first people I talked to when I first came to Germany. They made my life in the institute much easier and much more interesting.
- I am indebted to Fr. Wild, who took a lot of care of me and won the battle against the insurance company.
- I acknowledge a lot of discussions with Paris Tzallas, Dimitrios Charalambidis, Xue-qing Yan and Huichun Wu.
- I would like to acknowledge all members of our group, especially Antonia Popp, Matthias Fuchs, Patrick Heissler, Andreas Henig, Raphael Weingartner, Daniel Kiefer, Daniel Jung, Sandro Klingebiel, Christoph Wandt, Michael Hofstetter, Stefan Karsch, Zsuzsanna Major, Karl Schmid, Vova Pervak, Laszlo Veisz, Ioachim Pupeza, Michael

Korbman, Justin Gagnon and Vlad Yakovlev for great working and not-working atmosphere.

- My wife Arsenia always supported and encouraged me. I am extremely grateful to her for that!
- Last, but not least, I would like to thank my parents who opened the beauty of science to me and supported me in any matter.

This part of the thesis appeared to be very tough to write. I was trying not to forget anybody but most likely I did that. Non-intentionally, of course.

Curriculum Vitae

Personal data

Name: **Sergey Georgievich Rykovanov**

Date of birth: 30.01.1983

Place of birth: Snezhinsk/Russia

Citizenship: Russia

Current address

Max-Planck-Institut für Quantenoptik

Hans-Kopfermann-Str. 1

85748 Garching bei München, Germany

E-mail: sergey.rykovanov@mpq.mpg.de

Tel.: +49 89 32905-393

Education and academic experience

May 2006 - September 2009,

Ph.D. student at the Max-Planck-Institut für Quantenoptik, Garching, Germany and Ludwig-Maximilians-Universität München, Munich, Germany within the International Max-Planck Research School for Advanced Photonics (IMPRS-APS)

Thesis: Interaction of intense laser pulses with overdense plasmas. Theoretical and numerical study.

Supervisor: Prof. Dr. Hartmut Ruhl

2000-2006,

M.V. Lomonosov Moscow State University, Russia

Diploma with distinction in Physics with specialization in Laser Physics, January 2006

Thesis: Generation of fast particle and short x-ray pulses in the interaction of intense laser radiation with thin targets.

Supervisor: Prof. Dr. V.T. Platonenko

Secondary education, 1990-2000

Gymnasium 127, Snezhinsk, Russia